Max-Planck-Institut für Metallforschung
Stuttgart

Multiscale Modeling of Fracture and Deformation in Interface Controlled Materials

Nils Brödling

Dissertation
an der
Universität Stuttgart

Bericht Nr. 217
September 2007

Multiscale Modeling of Fracture and Deformation in Interface Controlled Materials

Von der Fakultät Chemie der Universität Stuttgart
zur Erlangung der Würde eines Doktors der
Naturwissenschaften (Dr. rer. nat.) genehmigte Abhandlung

Vorgelegt von

Dipl.-Ing. Nils C. Brödling

aus Detmold

Hauptberichter:	Prof. Dr. phil. E. Arzt
Mitberichter:	Prof. Dr. rer. nat. A. Hartmaier
Mitprüfer:	Prof. Dr. rer. nat. F. Aldinger
Tag der Einreichung:	23.07.2007
Tag der mündlichen Prüfung:	06.09.2007

Max-Planck-Institut für Metallforschung, Stuttgart

Juli 2007

To my parents

Acknowledgements

This work has been conducted at the Max Planck Institute for Metals Research in Stuttgart, and partially at the chair for General Material Properties, University of Erlangen.

First I would like to express my deepest gratitude to Prof. Dr. Huajian Gao, who accepted me as his doctoral student and gave me the opportunity to work on some of the most challenging problems in materials science. I am deeply indebted for his guidance and support. I have benefited much from the extremely stimulating working culture in our department and from our joint discussions with various visiting colleagues.

I am deeply indebted to Prof. Dr. Alexander Hartmaier for his persistent support, his guidance and encouragement that he provided during my time at the Max Planck Institute for Metals Research, unchanged after responding to his call to the University of Erlangen, and later during my stay at the chair for General Material Properties, University of Erlangen. Not forgetting the numerous lessons on discrete dislocation and atomistic modeling and for the many inspiring discussions that helped me toward my goal of completing my PhD research, thank you.

To my thesis committee members, especially Prof. Dr. Eduard Arzt for his support and for agreeing on assuming the *Hauptbericht* for my dissertation, and also Prof. Dr. Fritz Aldinger for agreeing on assuming the *Prüfungsvorsitz*, I am indebted.

For his great support and giving me the opportunity to work at MIT, thank you Dr. Markus Buehler. The unique working climate in your modeling group and your enthusiasm were very stimulating and beneficial to my research. I enjoyed the frequent discussions on atomistic modeling with you and your co-workers.

I would also like to express my gratitude to Dr. Chun Lu and Dr. Liu Zishun for inviting me to IHPC where I learnt about other computational methods, particularly, the level set dislocation dynamics method.

The environment at MPI has been nothing but conducive and for that there are a few to thank. Particulary, I would like to acknowledge Franz-Werner Gergen from the EDV department for his continuous help, and our secretary Silvia Casanova for her great support and continuous care especially in the last year. Furthermore, for some of my calculations I used the MD code "IMD" developed by the group of Prof. Dr. Trebin at the University of Stuttgart (Institut für Theoretische und Angewandte Physik). I gratefully acknowledge the support from Dr. Franz Gähler in order to make the necessary modifications to the code. Some of my large-scale computations were carried out at the very recently installed "Woodcrest" Compute-Cluster in Erlangen, and I like to commend Dr. Georg Hager from the Center of Excellence in High Performance Computing particular for his excellent continuous support especially in the test phase beginning of this year.

I would like to extend my thanks to all the colleagues and guests at the Max Planck Institute for Metals Research and at the chair for General Material Properties, University of Erlangen, for their help and for creating a pleasant working atmosphere.

I gratefully acknowledge financial support from the German Academic Exchange Service (*DAAD-Kurzzeitstipendium für Doktoranden*) and funding from the International Graduate-Scholarship program of the Agency for Science, Technology and Research, Singapore.

My family and friends, thank you for the encouragement and support, special thanks to Shuyi, my parents Marianne and Wilhelm, and my sister Nicole.

Abstract

Many nanostructured metals are characterized by scale dependent mechanical properties and by size effects due to geometrical confinement. Dislocation activities, interface mediated plasticity, and macroscopic yielding are quite different from those in unconstrained metals. The role of interfaces for the material properties and for the governing deformation mechanisms remains unclear despite the large efforts made in experimental and theoretical investigations. Here we approach the effect of geometrical confinement on the atomic and on the mesoscopic scale. We elucidate size effects on failure mechanisms and on scale dependent plasticity of nanostructured dual phase composite materials with the aid of computer simulations.

Cleavage failure of dual phase layered materials is simulated with a mesoscopic model to clarify the scaling behavior of the materials fracture toughness. The model accounts for the confinement effect that a layer geometry imposes on the collective dislocation behaviour near a moving crack tip. The critical layer thickness at which the bulk fracture toughness of the elastic-plastic material is reached as well as the bulk fracture toughness itself increase with the cohesive strength of the interface, but become smaller for higher yield strengths. The main conclusion drawn in this work is that fracture toughness as a function of layer thickness saturates gradually if dislocation activity is dispersed, dilute and not compact around the crack tip. It increases abruptly with the thickness when dislocation activity right at the crack tip is possible and a compact, shielding dislocation array forms near the crack tip.
Furthermore this work provides preliminary understanding of the governing mechanisms that control the limiting length scale for the strengthening of bioinspired metallic nanocomposits. Large-scale molecular dynamics simulations are performed to investigate the plastic deformation behavior of a bioinspired metallic nanocomposite which consists of hard nanosized Ni platelets embedded in a soft Al matrix. The simulation results are analyzed with respect to the prevailing deformation mechanisms quantifying the contribution of dislocation-based plasticity and interface-mediated interfacial slip as a function of the nanostructural scaling. The results of the simulations show that interfacial sliding contributes significantly to the plastic deformation despite a strong bonding across the interface. Critical for the strength of the nanocomposite is the geometric confinement of dislocation processes in the plastic phase. The confinement effect strongly depends on the length scale and the morphology of the metallic nanostructure. The main conclusion drawn for this material is that below a critical length scale, the softening caused by interfacial sliding prevails, giving rise to a maximum strength at the optimum size.

Kurzzusammenfassung (in German)

Viele nanostrukturierte Materialien sind durch ihre Längenskalen-abhängigen mechanischen Eigenschaften und durch Größeneffekte gekennzeichnet. Aufgrund geometrischer Einengung unterscheiden sich Versetzungsbewegungen, Grenzflächenplastizität und makroskopisches Fließen grundlegend von grob strukturierten Metallen. Welche Rolle die Grenzflächen für die Materialeigenschaften und für die vorherrschenden Verformungsmechanismen spielen, ist noch nicht abschließend geklärt. Diese Arbeit konzentriert sich auf den Einfluss geometrischer Einengung auf die Plastizität von nanostrukturierten, zweiphasigen Metallkompositen. Mit Hilfe von rechnergestützten Simulationen werden Größeneffekte auf Versagensmechanismen und Materialeigenschaften auf der atomaren und mesoskopischen Skala aufgeklärt.

Das Skalierungsverhalten der Bruchzähigkeit eines durch Sprödbruch versagenden Schichtmaterials wird mit einem diskreten Versetzungsmodell untersucht. Das Modell berücksichtigt den Einengungseffekt, den eine Schichtgeometrie auf die kollektive Versetzungsbewegung in der Nähe eines laufenden Risses ausübt. Sowohl die kritische Schichtdicke, bei der die Bulk-Bruchzähigkeit des Materials erreicht wird, als auch die Bulk-Bruchzähigkeit selbst steigen mit der kohäsiven Festigkeit der Grenzfläche und verringern sich mit der Fließfestigkeit des Volumenmaterials. Eine wesentliche Aussage dieser Arbeit ist, dass die Bruchzähigkeit als Funktion der Schichtdicke graduell in eine Sättigung übergeht, wenn die Versetzungsaktivtät um die Rissspitze herum verteilt ist. Sie steigt jedoch sprunghaft an, wenn Gleitprozesse direkt an der Rissspitze möglich sind und eine kompakte, abschirmende Versetzungsreihe an der Rissspitze ausgebildet werden kann.

Weiterhin liefert diese Arbeit erste Erkenntnisse über das Verformungverhalten bioinspirierter Metall-Nanokomposite. Die mit großskaliger Molekulardynamik simulierten Nanostrukturen bestehen aus harten in einer weichen Al-Matrix eingebetteten Ni-Plättchen. In dieser Arbeit werden zur Aufklärung der vorherrschenden Verformungsmechanismen die individuellen Gleitanteile der Versetzungsaktivitäten in der Matrix sowie des Grenzflächengleitens als Funktion von der Strukturskalierung quantifiziert. Die Simulationsergebnisse zeigen, dass Grenzflächengleiten trotz großer Grenzflächenhaftung wesentlich zur plastischen Verformung beiträgt. Entscheidend für die Festigkeit des Nanokomposits ist die Einengung der Versetzungsprozesse innerhalb der weichen Phase. Der Einengungseffekt hängt stark von der Längenskala und der Morphologie der Nanostruktur ab. Eine wichtige Aussage für dieses Materialsystem ist, dass das Material durch das Einsetzen von Grenzflächengleiten unterhalb einer kritischen Längenskala seine Festigkeit verliert.

Contents

List of Symbols

Roman letters

b	norm of Burgers vector
$\mathcal{B}$	isotropic linear elastic body
$\partial\mathcal{B}$	contour enclosing isotropic linear elastic body
B	mathematical dislocation (displacement discontinuity) density
$\mathbf{B}$	element vector of mathematical dislocations
$\mathbf{C}_n$	matrix representation of cohesive coefficients
d	scaling parameter of microstructure
E	Young's modulus
$\mathbf{f}$	Peach-Koehler force
$G_{\alpha\beta\gamma}, \mathbf{G}$	stress Green's tensor function, matrix representation
h	layer thickness
$\hat{h}$	critical layer thickness
J	J-Integral
k_I	local stress intensity factor
k_{Ic}	intrinsic fracture toughness
K_I	global stress intensity factor
K_{Ic}	fracture toughness
K_D	shielding stress intensity factor
$M_{\alpha\beta}, \mathbf{M}$	displacement Green's tensor function, matrix representation
$N, \mathbf{N}_n$	cohesive normal traction, matrix representation
$\mathbf{n}$	normal vector
R	blunting radius
$\mathbf{s}$	slip vector
$\mathbf{t}$	traction vector
$\mathbf{u}$	displacement vector

Greek letters

δ_1, δ_2	shape parameter of traction-separation law
Δ	normal separation displacement
Δ_c	critical crack tip opening displacement
$\boldsymbol{\varepsilon}^*$	eigenstrains induced by defects

$\boldsymbol{\varepsilon}$	infinitesimal strain tensor
Γ	cohesive energy
μ	shear modulus
ν	Poisson's ratio
ρ_{src}	source density
σ_{src}	source strength
σ_{th}	cohesive strength
σ_y	yield strength
$\boldsymbol{\sigma}$	stress tensor
ξ_k	dislocation position vector

Special notation

$\bar{(.)}$	mechanical fields of homogeneous sub-BVP
$\tilde{(.)}$	singular mechanical fields induced by dislocations
$\hat{(.)}$	mechanical image fields stemming from auxiliary sub-BVP
$(.)^\infty$	acting far field
$(.)^0$	applied boundary conditions
$\Delta(.)$	difference in values of coupled collocation points

1 Introduction

Interface controlled materials such as thin layered films or nanocrystalline materials are characterized by size effects due to geometrical confinement and scale dependent mechanical properties. Dislocation activities, interface mediated plasticity and macroscopic yielding are quite different from those in unconstrained metals. Deformation and failure of such materials are largely determined by the properties of the interfaces and by size effects. Typically the characteristic length scales are of the order of one micrometer and below. This work elucidates size effects on failure mechanisms and on scale dependent plasticity of nanostructured dual phase composite materials with the aid of computer simulations on the atomic and mesoscopic scale.

The theoretical studies presented in this thesis are oriented along the fields of failure analysis of microelectronic components and structural material design. The interfaces of the materials are viewed as discontinuities between a hard and a soft phase. We consider two material classes of high technical and scientific interest. Thin layered nanocomposites are used in a wide range of applications as microelectronic components. Research interests so far have been focused on plasticity in confined systems as thin films or nanocrystalline materials, but a detailed investigation of fracture or delamination under geometrical confinement of the plastic zone is still lacking. The possibility to nucleate dislocations in the crack-tip region is essential to shield the crack from the applied load and to prevent brittle crack propagation. However, geometrical confinement can severely affect the plastic shielding of the crack tip. Dislocations pile up at interfaces and the resulting back-stress prevents further dislocation nucleation at the crack tip. The second research focus is devoted to the area of interface engineering and biomimetic design. Structural refinement is a well-known process in the field of interface engineering to strengthen metals and is related to the confinement of slip during deformation due to the presence of interfaces. On the basis of the theoretical considerations, however, there must be a limiting transition of the dominant deformation mechanism on the nano scale. Many natural hard/soft nanocomposite materials, such as spider silk or nacre, are ideal examples for the design of strong and tough materials by structural refinement on the nano scale. Their superior mechanical properties may be attributed to a generic parallel staggered arrangement of their microstructure. In this thesis a novel bio-inspired design concept for structural refinement is tested. The studies provide preliminary understanding on the governing mechanisms that control the limiting length scale for the strengthening of their biomimetic metallic counterparts.

Chapter 2 of the thesis presents the review of the current state of research in the field of interface controlled materials. The survey will focus on well known scale dependencies of mechanical strength, as well as on size effects on the dominant deformation mechanisms in nanocrystalline materials. The modeling framework for small scale plasticity that is developed and used in this work will be introduced with special focus on cohesive zone interface description. Eventually, the theoretical background relevant to the studied material problems is provided, i.e. cleavage failure of metal layer and strength of nanocrystalline materials. Chapter 3 covers a combined dislocation dynamics cohesive zone model. The micro mechanical model was developed for the simulation of fracture processes in thin metal layer materials and further extended to describe bulk behavior of dual phase metal matrix composite with consideration of slip and decohesion at internal interfaces. Simulation results elucidating the effect of microstructure and layer thickness on fracture toughness of thin metal layers are presented in chapter 4. Chapter 5 includes the atomistic model and the limiting strength analysis of a biomorphous metallic nanocomposite. Scale dependent mechanical properties and size effects on the prevailing deformation mechanisms are presented over a wide range of the materials characteristic length scales under quasi-static tensile loading conditions. Chapter 6 discusses the results for failure and deformation of dual phase nanocomposites and the modeling strategies on multiple scales. Main findings are related to the current understanding of interface controlled plasticity in nanocrystalline. The applied simulations tools are critical reviewed with respect to their capability in resolving the dominant deformation mechanisms. Chapter 7 concludes this work with a summary of the main results.

2 Literature and theoretical background

This chapter is designed to review the current research focus regarding the meaning of interfaces for scale dependent mechanical properties as well as their role as barriers to lattice dislocation glide and as sources for interface mediated plastic deformation. This work focuses on developing structure-property relationships based on atomistic and mesoscopic modeling. Accordingly, discrete dislocation dynamics and molecular dynamics simulations for the study of small-scale plasticity are reviewed. Both frameworks are surveyed with a special focus on the description of material interfaces. Eventually, two material classes of high technical and scientific interest are introduced, each of which constitutes a separate length scale regime.

2.1 Scale dependence of strength on the nanometer scale

Plastic deformation of conventional polycrystals of average grain size $d > 1\,\mu$m occurs in two steps. After initial plastic flow by nucleation and motion of dislocations in grains with maximum shear stress an intensive multiplication of dislocations in grains with various orientations leads to a dramatic increase of the dislocation density. The stress during large scale yielding, the macroyield stress σ_y, is measured after the sample has undergone significant plastic strain so that all grains contribute to the plastic flow. The controlling factors and mechanisms of plastic flow in conventional polycrystals and their grain size effects have been of major interest since the experimental demonstration of grain size effects by Hall (1951) and Petch (1953). The Hall-Petch (HP) law that has shown to apply to the size regime above tens of nanometers (Kumar et al., 2003) states that σ_y scales with the average grain size d as

$$\sigma_y = \sigma_0 + kd^{-1/2}. \tag{2.1}$$

The HP constant σ_0 corresponds to the yield stress of the single crystal, where k depends on the formation of the dislocation microstructure during the deformation. For pure fcc metals typical values are $\sigma_0 \approx 10^{-4}\mu$ and $k \approx 0.05\mu\sqrt{b}$. The traditional derivation of the HP-laws is based on the occurrence of pile-ups that control the elasto-plastic transition at initial plastic flow. It is assumed that a large stress concentration ahead of the dislocation pile-up is required to transfer glide between adjacent grains by activation of Frank-Read sources in the neighboring grain. Bulk Frank-Read sources within the grains release dislocation loops at stress levels proportional to the inverse of the source length. The stress ahead of a pile-up approximately scales as $d^{-1/2}$ when the pile-up is modeled as a continuous distribution of infinitesimal dislocations and the exact positions of the discrete dislocations are neglected.

The variety of HP models differs in the assumptions for the pile-up formation. The HP relation (2.1) describing the dependence of yield stress on the grain size was later extended to cover flow stress at a given strain considering effects of intragranular plasticity. With decreasing grain sizes the dislocation network consists more and more of dislocation loops that are pinned at the grain boundary and partially remain inside the grain. In this view the flow stress is controlled by a dislocation network within the grain of density ρ (Cottrell, 1953). The resistance of the dislocation network to dislocation glide scales as $\sigma_y \sim \sqrt{\rho}$, where the total dislocation length of dislocations remaining inside the grain scales as $l_g \sim d^2$ and $\rho = \frac{l_g}{d^3}$. The HP relationship is therefore also obtained for the flow stress at a given strain when effects of intragranular plasticity are considered. However, the interpretation of the constants is rather difficult when the HP law is applied to the flow stress (Hansen, 2004).

It is widely accepted that the extension to the nanometer grain size has consequences for the strength of nanocrystalline materials. A deviation from the conventional HP like scale dependence has been observed in many experiments and computer simulations. Different types of deviation from the HP behavior are reported for metals with grain sizes less than a few tens of nanometers. The deviation was found either as an increase of the strength with a smaller slope, as a saturation of strength, or even as a softening at very small grain sizes. The postulated transition from grain size hardening to grain size softening suggests that there is an optimum grain size that provides maximal strength (Yip, 1998).

The optimum grain sizes that could be confirmed in experiments lie between 10 to

40 nm (Sanders et al., 1997; Masumura et al., 1998; Khan et al., 2000). Optimum grain sizes have also been reported based on atomistic modeling by Yamakov et al. (2003) and Schiøtz and Jacobsen (2003), with approximated values based on atomistic simulations as 18 nm for Al and $10 - 15$ nm for Cu, respectively. Different explanations for the behavior of the flow stress for decreasing grain sizes have been proposed. Based on their high temperature simulations, Yamakov et al. (2003) suggested that the behavior may involve diffusional flow. Schiøtz and Jacobsen (2003) found for small grain sizes that the strain is localized in the grain boundaries, indicating that the main deformation mechanism operating is grain boundary sliding.

The HP relationship is expected to break down if the discreteness of the dislocation microstructure becomes important, and even more, if different deformation mechanisms set in. Yet unanswered questions are: What are the physical mechanisms behind the deviation from the HP-behavior at small length scales? And most important, what is the limiting length scale where the trend predicted by this relationship breaks down?

2.2 Deformation mechanisms in nanostructured metals

Most understanding of the mechanisms operative under confinement during the deformation of nanocrystalline metals have been obtained by large-scale atomistic studies published in the last few years as reviewed in the literature (M.A. Meyers, 2006; Wolf et al., 2005). It is known that confinement effects result in a strong interplay between dislocation based deformation in the grain interior and plastic deformation mechanisms in the grain boundary regions. The strain b/d provided by a single dislocation crossing a grain increases with decreasing grain size. Consequently, the number of dislocations involved in a total strain increment decreases with grain size. Dislocation based deformation in nanocrystalline metals is therefore discrete in nature as only tens of dislocations crossing a grain are necessary to generate a total plastic strain of a few percent. This suggests that collective dislocation motion and dislocation multiplication vanishes gradually when the grain size decreases.

As observed experimentally (Janecek et al., 2000) and in atomistic simulations (Derlet and Swygenhoven, 2004), deformation of the corresponding nanocrystalline material proceeds through direct transfer of individual dislocations across the grain from a grain boundary where they are nucleated to the opposite grain boundaries at which they are annihilated. The kinetics of this deformation mechanism is controlled by the nucleation and annihilation process. When dislocation based deformation is confined to even smaller grain sizes, plastic deformation mechanisms at grain boundaries are more effective to produce overall plastic deformation and become dominant (Kumar et al., 2003; Schiøtz and Jacobsen, 2003).

2.2.1 Dislocation based deformation under confinement

Confinement effects on plastic deformation of polycrystals arise when the glide of lattice dislocations is effectively hindered by the presence of interfaces. In case of heterophase interfaces, the confinement effects due to contact interactions between lattice dislocations and interfaces appear in several forms depending on the interface structure. Coherent interfaces maintaining the continuity of a reference lattice allow the transmission of lattice dislocations. In semicoherent interfaces coherent regions are separated by misfit dislocations that accommodate the lattice misfit between the adjoining crystals. In the limit of incoherent interfaces, the spacing of the misfit dislocation is comparable to the width of their cores and the lattice continuity across the interface disappears completely. In coarse grained materials, even though direct slip across non coherent grain boundaries is terminated by special geometric conditions, slip may still be propagated if pile-ups of incoming dislocations generate sufficiently high local stresses in the vicinity of the boundary to activate sources in the adjacent crystal.

The use of atomistic simulations of nanocrystalline materials has substantially contributed to the understanding of the atomic mechanisms associated with the nucleation of dislocation from bimaterial interfaces in confined systems. MD simulations elucidated, in particular, the nucleation of partial dislocations from interfaces in face-centered cubic (fcc) bicrystals (Sansoz and Molinari, 2004, 2005) as well as nanocrystalline materials (Yamakov et al., 2002, 2003, 2004; Swygenhoven and Caro, 1998; Swygenhoven et al., 1999a,b, 2001, 2002, 2004; Derlet and Swygenhoven, 2004; Derlet et al., 2003; Schiøtz et al., 1999; Schiøtz and Jacobsen, 2003; Schiøtz and Tolla, 1998). Calculations by Van Swygenhoven and Schiøtz for grain sizes less than 10 nm have shown that deformation is dominated by grain boundary processes, such as grain boundary migration or grain boundary sliding. Above this grain size, deformation of nanocrystalline metals is a result of both grain boundary processes and dislocation activities within the grain. They found that sources for dislocation nucleation were exclusively provided by the grain boundaries of the sample. Early simulations of nc pure Ni and Cu with a grain size of about 12 nm showed that the leading partial dislocation is emitted, sweeps across the grain and is absorbed in the opposite interface. Oftentimes the trailing partial dislocation is not emitted. In this case an extended intrinsic stacking fault remains within the grain with a larger extension than the typical equilibrium spacing between partial dislocations. In their analysis of the grain boundary structure it was shown that nucleation of the first partial was assisted by “atomic shuffling“ within the interface and stress-assisted free volume migration. They suggested the stress relaxation by the nucleation of the first partial dislocation accompanied by the interfacial atomic rearrangement was sufficient to reduce that grain boundary energy so that the nucleation of the second partial was unnecessary.

The simulations by Yamakov et al. (2002, 2003, 2004) for nc Al with a higher stacking fault energy showed that the second partial dislocation may emit from the interfaces. They analyzed a columnar structure to be able to simulate larger grain sizes. They identified the stacking fault width as a critical length scale parameter necessary to describe the cross-over between two deformation regimes of extended partial and full dislocations.

In a following work by Swygenhoven et al. (2004) and Frøseth et al. (2004) it has then been argued that the interpretation between different deformation regimes in terms of the intrinsic stacking fault energy is insufficient and that the entire generalized stacking fault curve (Zimmerman et al., 2000) needs to be taken into account. They proposed that the dislocation activity in nanocrystalline samples should be described by the ratio of the unstable and intrinsic stacking fault energies. The occurrence of full dislocation pile-ups during deformation of nc materials indicating a correlation with the HP behavior is still under debate. Schiøtz and Tolla (1998) observed dislocation pile-ups of several dislocations locked on grain boundaries in nc Cu within the strengthening grain size regime of about 50 nm.

2.2.2 Interface mediated plastic deformation

Interface mediated deformation mechanisms play an important role in materials with grain sizes smaller than the critical grain size ($\sim 100\,\mathrm{nm}$) to activate a dislocation source within the grain. The mechanisms that are critical for the strength of nanocrystalline materials are grain boundary sliding, diffusional creep at grain boundaries and triple junctions, and rotational deformation modes. In addition, ductility and fracture of nanocrystalline materials is very sensitive to interfacial decohesion and void formation.

Depending on the temperature regime, two types of grain boundary sliding are distinguished in the theory of the deformation of polycrystals (Langdon, 2006). Rachinger sliding is accommodated by the movement of intragranular dislocations and Lifshitz sliding accommodates diffusion creep. At elevated temperatures thermal activated processes such as diffusional matter transport becomes important. At low temperatures and in the presence of plastic flow within the adjoining crystals interface sliding can be accommodated via the motion of lattice dislocations. This process occurs at relatively high stresses and depends upon the interface acting as sources or sinks for lattice dislocations. The inelastic deformation within the grain boundary region at low temperature observed in atomistic simulations (Swygenhoven et al., 1999,a,b) is not dominated by thermal diffusion of atoms in the grain boundary region, even though it is sometimes regarded as ”grain boundary sliding”. Note that grain boundary sliding is defined as a thermally activated process present at high temperatures (Sutton and Balluffi, 1995).

In general, interface sliding in bicrystals is defined as a plastic shear displacement of two crystals with respect to each other parallel to the interface localized in an interfacial region in response to applied forces. Depending on the interface structure the shear that is associated with the interface sliding can be distributed over a slap of material which includes the interface or can be restricted to the narrow core of the interface. As one form of plastic deformation, interface sliding contributes to the overall plastic deformation and in addition, may be responsible for cavitation or interfacial void formation successively leading to interfacial mechanical failure. Contrary to the simple macroscopic view of two shearing uniform blocks, on the atomistic scale interface sliding is a complex phenomenon that strongly depends on the plasticity of the adjoining crystals and on the interface characteristics. Similar to shearing of a single crystal by the passage of dislocation, interfaces sliding occurs preferably in a non-uniform manner. This process requires lower stresses than shearing of the entire interface simultaneously (Sutton and Balluffi, 1995).

Here we use the term “interface shearing“ to denote a stress induced and dislocation assisted interface mediated process in nanocomposite structures. Contact interaction between lattice dislocations and interfaces under the action of high local stresses result in local shear displacement events of interface atoms or the motion of grain boundary dislocations with Burgers vector parallel to the interface. The collectively shear-displaced interface atoms result in interface sliding of that entire segment.

For low temperatures, there is some experimental evidence for occurrence of interface sliding in nanostructured materials produced by electrodeposition (Lu et al., 2000) and by severe plastic deformation (Valiev et al., 2002). The effect was explained by a very high density of extrinsic dislocations that permits easy interface sliding (Valiev, 2004). The presence of high dislocation densities adjacent to grain boundaries found by electron microscopy after SPD processing seems to support this explanation. Another explanation was proposed regarding the width of the grain boundaries with respect to the grain size. In nanostructured materials it would be possible to develop macroscopic sliding along planes extending over distances that are much larger than the grain size (Hahn et al., 1997). This behaviour was found experimentally after SPD processing for several materials (Vinogradov et al., 2001).

A body of atomistic analyses can be found in literature that addresses either the characteristics of interfacial sliding during the deformation of metallic bicrystals (Wolf, 1990; Sansoz and Molinari, 2004, 2005; Chandra and Dang, 1999), and more recently, the role of interface sliding and decohesion for the deformation of metallic nanocrystals (Schiøtz et al., 1999; Schiøtz and Jacobsen, 2003; Schiøtz and Tolla, 1998; Swygenhoven et al., 1999,a,b, 2001, 2002; Farkas et al., 2005; Derlet and Swygenhoven, 2004; Derlet et al., 2003). Most research on metallic bicrystals addresses the simplest case, i.e. interface sliding at an ideal planar grain boundary. In early works, e.g. (Wolf, 1990), the structure and energy of boundaries was analysed at 0 K and at finite temperatures without addressing plastic deformation. Chandra and Dang (1999) studied the characteristics of interface sliding and migration of several low-order Γ interfaces in Al. Sliding is induced by applying either displacement or a force to one of the crystal boundaries. When subjected to an applied shear force, they showed that grain migration and grain sliding are coupled. A major result is that low energy boundaries offer more resistance to shear deformation than higher energy boundaries. Sansoz and Molinari (2004, 2005) have recently used the quasicontinuum method to study the deformation and failure of bicrystal models with symmetric Γ boundaries under shear and tension. For shear loading, they specify three different failure modes depending on the initial boundary configuration: grain boundary sliding by atomic shuffling, nucleation of partial dislocations from the bicrystal interface and grain boundary migration. Atomic shuffling appeared to be triggered by the free volume inherent to the structural feature of the boundaries.

A larger body of recent atomistic simulations of interface sliding have focused on nanocrystalline samples. Molecular dynamics simulations of the deformation of metallic polycrystals (Schiøtz et al., 1999; Schiøtz and Jacobsen, 2003; Swygenhoven et al., 1999; Schiøtz and Tolla, 1998; Swygenhoven et al., 1999a,b, 2001, 2002; Farkas et al., 2005; Derlet and Swygenhoven, 2004; Derlet et al., 2003) suggest that interface sliding is increasingly important when the grain size is extremely small. Van Swygenhoven and coworkers analysed their structure evaluating the displacement vector distribution and atomic coordination to detect the nucleation of dislocations and the interface evolution in nanocrystalline Ni and Cu samples. The initial samples were annealed at room temperature for a short period of time to equilibrate the structure. They observed atomic shuffling and stress-assisted free volume migration along the interface plane prior to the dislocation nucleation event. However, a quantitatively evaluation of the role of interface sliding for scale dependent plastic deformation is lacking.

In addition to the interface mediated deformation mechanisms, there are also failure mechanisms associated with interfaces. The effect of interfacial flaws, e.g. due to impurities at the interface, have been a major concern in technical application for decades. Slow decohesion where the decohesion zone evolves with time was addressed in various research fields, such as stress-corrosion cracking or embrittlement of high strength steel. Failure modes in nanocrystalline materials such as shear-failure, nanocracking and cavitation have only been addressed recently. These failure mechanisms may occur prior to macroscopic ductile fracture in nanocrystalline materials which is viewed to occur through a nano-void coalescence mechanism. Interfacial flaws have therefore a significant effect on the macroscopic fracture toughness. The formation of interfacial damage in the vicinity of a crack tip has been simulated recently by pure atomistic approaches (Farkas et al., 2002, 2005; Sansoz and Molinari, 2004). Farkas et al. (2002) observed grain boundary decohesion and cavitation in the atomistic analysis for nanocrystalline Ni. The simulations show grain boundary nano-void formation leading to intergranular fracture. However, initiation of interfacial damage initiation is a coupled process between dislocation activity in the adjacent crystals and interfacial decohesion. It remains unclear whether the initiation and evolution of this failure mechanism is dependent on the grain size of nanocrystalline materials due to confinement effects on plasticity.

2.3 Modeling scale dependent plasticity in small dimensions

Within the scope of this thesis, size effects on plasticity and on failure mechanisms of nanostructured dual phase composite materials are investigated with the aid of computer simulations on the atomic and mesoscopic scale. One part of these studies focuses on mesoscopic dislocation dynamics simulations. Such DD simulations can capture the dynamical development of dislocation microstructures on time and length scales that are important for the brittleness or ductility of a material. It is apparent that DD methods can not capture all the atomistic details of dislocation nucleation and reaction processes as they occur in the composite material, including the effects of a realistic 3D structure. Therefore, MD simulations will be employed for a fundamental, atomic and physically based description of the dual phase composites. MD simulation is a very useful tool to study details of materials failure processes. During such simulations the equations of motion of a large number of atoms interacting with semi-empirical potentials are solved. The principal challenge of this research is the treatment of the interface between dissimilar materials. A critical aspect for the realistic simulation of the governing material processes is the availability, choice and implementation of appropriate interatomic potentials in MD, respectively, cohesive zone models in DD to describe interfaces in dual phase metallic composites.

To derive effective material properties from mesoscopic or atomistic simulations, the nanoscale (MD), respectively, the microscale (DD) needs to be linked to the macroscale. The macroscale is incorporated via appropriate macroscopic loading conditions that are applied to a small scale domain, e.g. the near crack tip region, which is then prescribed with atomistic or discrete dislocation theory. The macroscopic loading is specified with a loading parameter that represents the intensity of the acting remote field. With this approach it is possible to investigate the interaction of interfaces with defects, like dislocations or cracks, and to deduce macroscopic quantities like strength, toughness or ductility of the structure. Besides the fundamental methods (MD,DD) there are hybrid frameworks in the field of multiscale modeling that connect several length scales by linking different modeling schemes.

2.3.1 The mesoscopic scale

Dislocation dynamics

In many materials problems plasticity spreads out from high stress concentrations, e.g. a crack tip or a nanoindent. These problems involve several physical length scales and have therefore been addressed with multiscale modeling approaches. Molecular dynamics applies to the atomic region right at the crack tip, respectively, underneath the indenter tip. On a somewhat larger length scale DD plasticity is the appropriate description, while at still larger distances continuum crystal plasticity is used. As a purely atomistic framework is useful for the study of nucleation of single dislocations and material cleavage, and continuum crystal plasticity applies to macroscopic cracking covering local strain hardening due to a high density of geometrically necessary dislocations, for the intermediate regime of micro and submicron fracture problems discrete dislocation plasticity is an appropriate approach. In this work, a two dimensional combined dislocation dynamics-cohesive zone model is developed to study interface controlled microscale plasticity problems. The mesoscopic simulation tool is used to study fracture of nanoscaled layered structures and further modified for the simulation of representative volume elements of dual phase metal matrix composites.

Despite inherent limitations of two-dimensional models in describing formation of (three-dimensional) dislocation structures and atomic-scale phenomena, such models have been shown to capture some of the most important features in the discreteness of plastic deformation by considering nucleation of dislocations at discrete sources and motion of individual dislocations on slip planes. At the present time, fully three dimensional (3D) dislocation simulations have not advanced to the stage of being able to solve boundary value problems of practical significance and two dimensional (2D) simulations continue to be an important tool to investigate plasticity in micro- and nanostructured materials where classical continuum plasticity is often not applicable. A number of problems concerning microscale plastic deformation have been investigated based on the 2D DD method developed by Van der Giessen and Needleman (1995). They introduced a technique where the boundary value problem (BVP) of discrete dislocations is transformed into a weak formulation and then solved within a finite element (FEM) approach. Later a cohesive zone formulation was implemented to study fracture accompanied by plastic deformation (Cleveringa et al., 2000; Deshpande et al., 2003). Other workers followed alternative approaches based on Green's functions to incorporate the evolution of a dislocation microstructure under different boundary conditions into DD models. For example, a procedure was developed to evaluate contact stresses in the wake region of a growing fatigue crack (Riemelmoser et al., 1997). Other applications of DD methods include the study of nanoindentation (Kreuzer and Pippan, 2004) and constrained diffusional creep in polycrystalline thin films on substrates (Hartmaier et al., 2003, 2005).

The general framework for modeling the kinetics of discrete lattice dislocations in the vicinity of material interfaces is based on continuum mechanics. Within this mesoscopic approach, the microstructure of a solid and the internal elastic fields are associated with a number of discrete dislocations. The driving force for dislocation motion is assumed to be completely described within the framework of elasticity.

Cohesive zone interface description

Cohesive zone (CZ) models describing the process zone ahead of a crack tip have widely been used for static and dynamic simulations in the area of continuum damage or fracture mechanics, see e.g. (Raabe et al., 2004). CZ models have recently been coupled to continuum crystal plasticity models to describe the deformation of nc materials accounting for both reversible elastic and irreversible inelastic sliding-separation deformations (Wei and Anand, 2004). Other workers performed crack propagation analysis with a cohesive modelling approach focusing on crystal plasticity effects in the fracture behavior of metal/ceramic interfaces (Siddiq and Schmauder, 2006). A cohesive zone formulation has first been implemented in a discrete dislocation plasticity framework by Cleveringa et al. (2000). Their model was mainly used to study fracture accompanied by plastic deformation (Cleveringa et al., 2000; Deshpande et al., 2003). In all these approaches (Wei and Anand, 2004; Siddiq and Schmauder, 2006), including the DD/CZ implementation by Cleveringa et al. (2000), the cohesive zone models were integrated in a finite element framework that requires the discretization of the interior of the continuum, particulary, the region of high dislocation activity. The total computational time of a DD scheme relies very much on the efficient and accurate evaluation of an auxiliary subproblem, see chapter 3. Additionally, modeling defects near a stress concentration such as in crack growth or contact evolution problems require a high resolution of the process zone. For this type of problems the boundary element method (BEM) is expected to have computational advantages besides providing a good accuracy with minimal discretization effort compared to FEM based frameworks. The BEM has often been used in combination with cohesive zone model for damage locus description in brittle materials, e.g. (Yang et al., 2001). In addition, the BEM has shown to be a quite suitable approach for modeling DD plasticity in fatigue crack and evolving contact problems (Kreuzer and Pippan, 2004; Riemelmoser et al., 1997), see also chapter 3. One major objective in this work is therefore to develop a combined DD/CZ model by means of a boundary integral method to study fracture of nanoscaled layered structures.

The cohesive zone does not represent any physical material, but describes the cohesive forces that occur when the material is pulled apart. Cohesive elements are therefore placed between two phases of continuous bulk material. When damage occurs the cohesive zone elements open in order to simulate crack advance or decohesion at interfaces, see Figure 2.1. Cohesive zone models originated from the idea that fracture is a proceeding process in which separation takes place across an extended crack tip. The separation process is resisted by cohesive tractions ahead of the crack tip in the so called process or cohesive zone (Raabe et al., 2004; Ortiz and Pandolfi, 1999) which consists of a lower and an upper cohesive surface that are held together by cohesive tractions. The cohesive tractions are related to the cohesive separation of the surfaces by a traction-separation law (TS-law). The failure description is defined by traction-separation laws (TS-laws) (Chandra et al., 2002) that determine the constitutive behavior of the cohesive zone model. In two dimensions, cohesive traction can only occur in the normal and tangential direction. In the general theory of cohesive surfaces (Xu and Needleman, 1994) the traction vector is derived from an interfacial potential ϕ. The opening and shear components

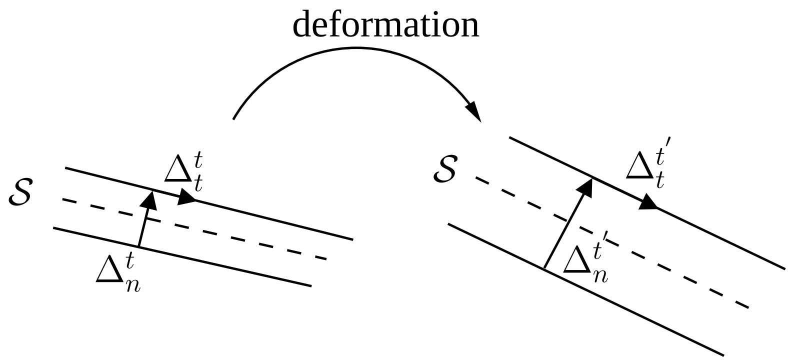

Figure 2.1: Definition of sliding Δ_t and opening Δ_n separation for the cohesive surface $\mathcal{S}$ before at time t and after deformation at time t'

N and S are the derivatives with respect to normal Δ_n

$$N = -\frac{\partial \phi}{\partial \Delta_n} \tag{2.2}$$

and tangential separation Δ_t

$$S = -\frac{\partial \phi}{\partial \Delta_t} \,. \tag{2.3}$$

The area under the TS curves $N(\Delta_n)$ and $S(\Delta_t)$ represents the amount of work needed for complete separation.

Cohesive zone models have been typically used as heuristically derived relationships. The values for the quantities that are input to the analysis at the microstructural scale are based on macroscopic parameters such as fracture toughness. In most work the parameters stem from experimental studies and do not originate from the physics of the atomic scale. Besides crack propagation studies, cohesive zone models have also been applied to the deformation of polycrystals (Zavattieri and Espinosa, 2001; Espinosa and Zavattieri, 2003; Wei and Anand, 2004).

Multiscale modeling approaches have recently been proposed in which the cohesive zone formulation is based on physics of the smallest scale to solve macroscopic engineering problems. The cohesive zone parameters are extracted from computations based on molecular dynamics or quantum mechanics and passed to continuum models. Models have been developed from results of molecular dynamics allowing the physical insight of the atomistics to be embedded in the more computationally efficient continuum descriptions, for example (Yamakov et al., 2006; Gall et al., 2000). They applied a statistical procedure to extract traction-displacement curves from the atomic forces and motions around crack tips for the investigation of brittle and ductile crack propagations (Yamakov et al., 2006) and studied deformation and fracture characteristics of incoherent interfaces (Gall et al., 2000). Following the same idea of multiscale modeling, interface energies were calculated on a quantum level of material separation to investigate the effect of atomic-level properties on chemically induced crack formation, e.g. (Jarvis et al., 2001).

2.3.2 The atomistic scale

Molecular dynamics

MD simulation techniques have proven to be suitable to investigate the dependence of the mechanical properties such as yield stress, flow stress and hardness on the grain size, e.g. (Schiøtz and Tolla, 1998; Schiøtz and Jacobsen, 2003; Schiøtz et al., 1999; Yamakov et al., 2002, 2003). They also helped identify size effects in brittle materials and adhesive systems and were used to demonstrate the existence of flaw tolerant length scales (Buehler et al., 2006). Advancing computational power in recent years allowed setting up three-dimensional models of nanostructured materials and analyzing the governing deformation mechanisms even up to the Hall-Petch regime (Schiøtz and Tolla, 1998; Schiøtz and Jacobsen, 2003). Most research work using MD simulation techniques on understanding the mechanisms responsible for deformation of nanostructured materials has been carried out for nanocrystalline single phase metals. In this work, molecular dynamics (MD) is employed to study the atomic scale mechanisms that occur in a dual phase metallic nanocomposite as a result of an applied mechanical deformation and to derive scale dependent mechanical properties.

MD refers to a well-established atomistic simulation framework to model the interaction and evolution of a set of atoms under given boundary conditions, see e.g. (Allen and Tildesley, 1996). The set of atoms is represented as point masses in space that interact through multibody interaction potentials. The interatomic potentials provide a model for the total potential energy of the system avoiding the complex description of electron dynamics. In the absence of externally applied forces, the force on a given atom $\mathbf{f}_i$ is obtained as

$$\mathbf{f}_i = -\nabla E_{tot}. \tag{2.4}$$

The evolution of atomic positions is described with Newton's second law of motion

$$\mathbf{f}_i = m\ddot{\mathbf{r}}_i, \tag{2.5}$$

where the double dot signifies the second derivative with respect to time. In this work, equilibrium atomistic simulations are performed, in which the system is isolated from its surroundings with a fixed number of atoms, volume and constant total energy is minimized. These boundary conditions correspond to the microcanonical NVE ensemble in statistical mechanics. In the analysis presented in chapter 5, MD calculations are used to compute minimum energy structures during the deformation of dual phase systems within a given tolerance based on a special relaxation scheme. The calculations are conducted with the parallel classical molecular-dynamics code 'IMD' from the Institute of Theoretical and Applied Physics, University of Stuttgart (Stadler et al., 1997). In the relaxation scheme, the residual force vector, defined as the negative of the gradient of the potential energy, is set to zero to solve for appropiate values of $\mathbf{r}_i$ that minimizes E_{tot} (Bitzek et al., 2006).

The interatomic potential used in atomistic simulation are semi-empirical and fit to match certain material properties (lattice constant, bulk modulus, elastic constants, vacancy formation energy) from quantum mechanics calculations or experiments. The choice of the potential has significant impact on the performance of atomistic simulations. Several classes of semi-empirical interatomic potentials are defined depending on their complexity. Lennard-Jones 12-6 potential (Lennard-Jones, 1924), e.g. for the simplest type of fully empirical pair potentials, the force between two atoms is a function of only the distance between those two atoms. Cluster potentials, on the other hand, consider both the distance between atoms and the angles between sets of atoms in the force calculation. One example of a semi-empirical potential is the the embedded-atom method (EAM) potential. The EAM potential is known to combine an realistic description of metallic bonding together with high computational efficiency. The EAM considers the total energy of a set of atoms in the functional form Daw and Baskes (1984)

$$E_{tot} = \frac{1}{2}\sum_{i,j} \Phi_{ij}(r_{ij}) + \sum_{i,j} F_i(\bar{\rho}_i), \tag{2.6}$$

where $\Phi_{ij}(r_{ij})$ is the pair-interaction term between atom pair (ij) separated by a distance r_{ij}. $\bar{\rho}_i$ is the host electron density induced by the surrounding atoms j at the position of atom i. The host electron density is defined as

$$\bar{\rho}_i = \sum_{ij} \rho_j(r_{ij}), \tag{2.7}$$

where ρ_j is the electron-density function associated with atom j. Local atoms only within a specified cut-off distance are considered. The cut-off distance typically includes at least first and second nearest neighbors. More recently, interatomic EAM potentials were developed to match additional structural properties, such as the stacking fault energy (Mishin et al., 1999, 2001).

Another important issue for the atomistic setup is the calculating capacity required to carry out the simulations. About 150 to 300 million atoms are necessary for a model size of about 50 nanometers in three dimensions. In order to enable extensive parameter studies over a wide range of the characteristic length scale and with a realistic description of the atomic interaction many researchers have used quasi-two dimensional atomistic setups of columnar structures, e.g. (Yamakov et al., 2003; Farkas and Curtin, 2005; Zhang et al., 2004).

Atomistic interface description

The limiting strength analysis of a biomorphous hard/soft nanocomposite (chapter 5) is conducted for a metallic dual phase Ni-Al model system. Hard nanosized nickel platelets are embedded in a soft aluminum matrix with a nanostructural morphology similar to that of bone. The atomistic description of the Ni/Al interface is based on an EAM interatomic potential for NiAl. Different EAM interatomic potentials, namely those from Foiles and Daw (1987), Voter and Chen (1987), Ludwig and Gumbsch (1995), have been employed to describe the properties of Ni-Al systems. In this study, the EAM potential developed by Ludwig and Gumbsch (1995) is employed. The potential is known to accurately reproduce the equilibrium lattice parameter and the elastic constants and to predict the correct constitutional point defect population. Furthermore, it behaves sensibly under large strains. The full description of the Ni-Al system requires definition of seven potential functions. The functions are obtained by fitting to the properties of the individual Ni and Al elements, respectively, to the properties of the Ni-Al alloys in case of the cross-interaction functions (Ludwig and Gumbsch, 1995). The potential used for the Ni-Al system also gives a good representation of the interatomic forces across interfaces between Ni and Al.

2.4 Scale dependence due to plastic confinement – case studies

2.4.1 Cleavage failure of metal layer

Research on crack initiation and fracture in layered materials is motivated by the need for predictive models for failure on microelectronic packaging and devices. A very important class of layered materials is a thin film bonded between two hard substrates. The failure mechanisms alter fundamentally depending on whether the film is ductile or brittle and on the properties of the film-substrate interface. For macroscopic fracture of a ductile film between hard substrates, void nucleation and growth can be assumed to be the main failure mechanism in the film.

Scale dependence in the large scale regime

The ductile failure mechanisms of traditional metal layer materials with above micron layer thickness were classified by (O´Dowd et al., 1992, 2001; Varias et al.,

1991) as: near-tip void growth and coalescence, interface debonding near the tip, high triaxiality cavitation and interface debonding ahead of the crack tip. Near-tip void growth and coalescence occurs supposedly in ductile layers. Interface debonding occurs near the tip when the local stresses at the crack tip normal to the interface exceeds the strength of the interface. High triaxiality cavitation at a distance of several layer thicknesses ahead of the crack tip followed by void coalescence occurs when the interface strength is sufficiently strong and the ductile layer undergoes substantial plastic deformation. The first two mechanisms operate if the mean spacing between voids is much less than the layer thickness or if the interface bond is weak, otherwise, the last two mechanisms are operative, see (O´Dowd et al., 2001). Theories and numerical tools based on conventional continuum plasticity describing fracture in layered materials in the layer thickness range of one micron and above are well advanced (Tvergaard and Hutchinson, 1994). The main aspect that is relevant to existing models is the restrictions that a layer geometry imposes on the expansion of the plastic zone and to the resulting fracture toughness of layer composites, see Figure 2.2. It has been shown experimentally and theoretically that the toughness of a ductile layer sandwiched between elastic substrates decreases with increased mode mixing and increases with the thickness of the ductile layer until the layer fails plastically. As Varias et al. (1991) found, this is due to plastic confinement the tensile stress at the crack tip increases as the thickness decreases. In spite of the progress in developing appropriate models for fracture of traditional layered materials, only

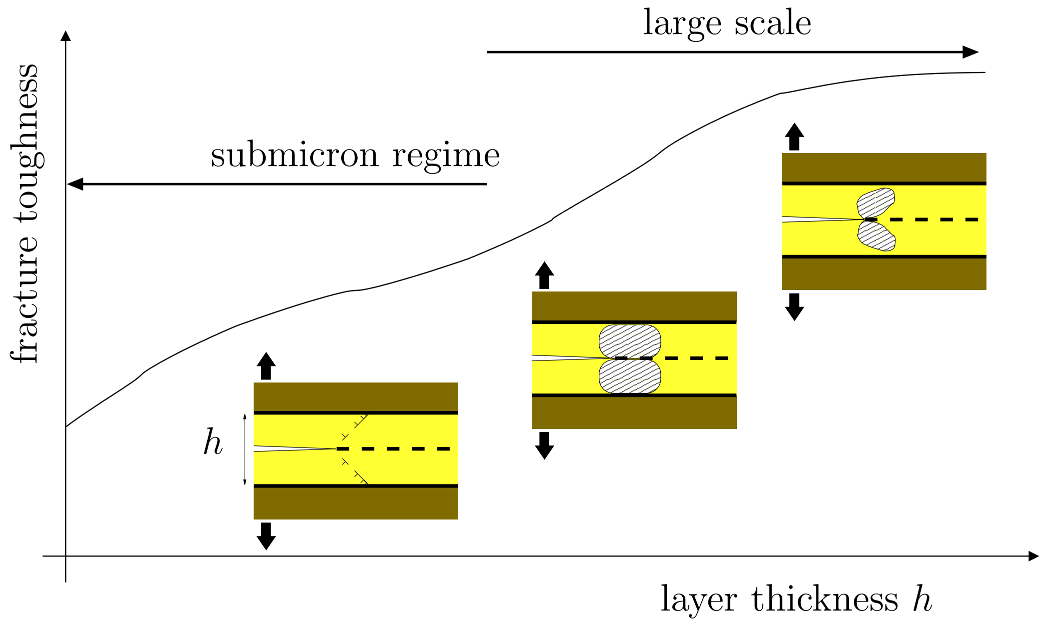

Figure 2.2: Schematics of the fracture toughness as a function of layer thickness

a small body of experimental work exists on this topic. Recent experimental studies for Al interlayers of various thicknesses ($0.2 - 3\,\mathrm{mm}$) suggest that metal layers exhibited failure modes that are different to those in the bulk form of the layer material. The plastic confinement resulted in a transition from ductile to brittle failure even in a intrinsically ductile metal such as fcc pure Al (Han et al., 2005).

Analytical pile-up model for the submicron regime

In modern industrial applications multi layer materials with multiple alternating hard and ductile layers are used with a thickness ranging from 10 nm to 1000 nm. As a consequence of dislocation confinement by narrowly spaced internal boundaries, the stress variation over the layer thickness is large compared to the macroscopic yield strength. The discrete nature of plastic flow becomes important, as size effects in this regime are dominated by the elastic interaction between discrete dislocations with the crack tip and the interfaces, see Figure 2.3. Appropriate modeling approaches for the plastic flow processes must treat interfaces and dislocation activities individually (Suo et al., 1991). When the plastic zone is modeled by a dislocation population around the crack tip subjected to a applied stress intensity factor K_I, the local stress intensity factor k_I is reduced by a shielding factor K_D as

$$k_I = K_I - K_D. \tag{2.8}$$

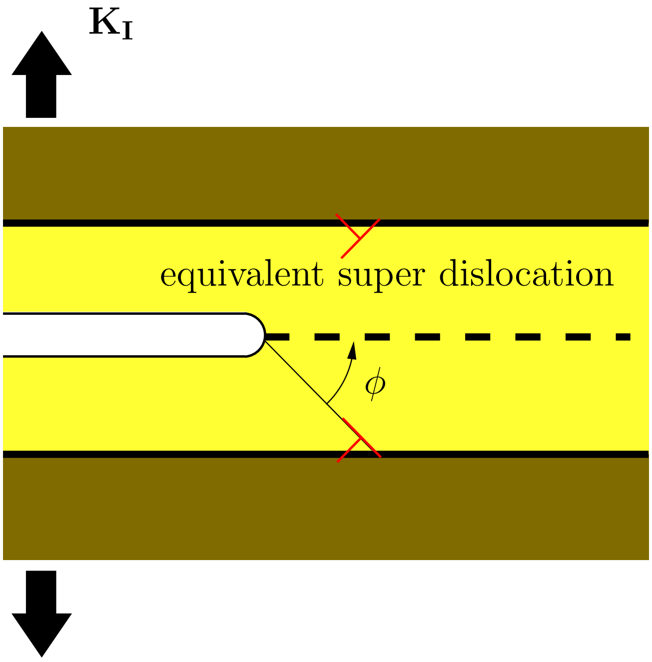

Figure 2.3: Schematics of the effective superdislocation model by Hsia et al. (1994)

Shielding dislocations emitted at the crack tip relax the high stress concentration there, due to their elastic interaction with the crack tip. This effect is regarded as crack tip shielding and was extensively studied by Lin and Thomson (1986). In the absence of confinement, shielding dislocations move freely away from the crack tip forming an inverse pile-up in which the dislocation spacing increases with increasing distance from the crack tip. The condition for cleavage failure due to confinement effects in the thickness regime of a few micrometers has been recently addressed by an analytical analysis for a semi-infinite crack within a metal layer (Hsia et al., 1994), and for crack initiation at a bimaterial interface (Mao and Lib, 1999). The central arguments in the model by Hsia et al. (1994) and the main results are summarized in the following, see Figure 2.3. Hsia et al. (1994) considered a semi-infinite crack tip located in the center of the metal layer interacting with an equilibrium numbers of shielding dislocations that are pinned at the interfaces. The dislocation microstructure is idealized by two super dislocations located at the interfaces. The effect of crack tip blunting on the crack tip stresses is approximated assuming the formation of a notch of semicircular shape due to dislocation emission. The contribution K_D due to the interaction forces between a semi-infinite crack tip and a emitted dislocation located at the interface can be written (Lin and Thomson, 1986) as

$$K_D = \frac{\mu b}{(1-\nu)2\pi h_\phi}\frac{3}{2}\sin\phi\cos\frac{\phi}{2}, \tag{2.9}$$

with $h_\phi = h/(2\sin\phi)$. The equilibrium number n of emitted dislocations stored in the super dislocations is estimated comparing the energy of the state with $(n-1)$ and the one with n dislocations. If the total energy decreases by generating an additional dislocation across the whole crack front, the state with n dislocations is energetically preferable. Thus, the criterion for the equilibrium dislocation number is

$$\Delta W_T = W_T^n - W_T^{n-1} > 0. \tag{2.10}$$

The total energy W_T of a systems with two dislocation pile-ups is the sum

$$W_T = W_d + W_K + W_L. \tag{2.11}$$

The dislocation self energy W_d in the presence of a semi-infinite crack can be evaluated as the work done by dragging the dislocation against its image force along the slip plane from the crack tip to the current location. The interaction energy between the dislocation and the crack tip due to the presence of an applied K-field W_K is viewed similarly as the work done by the crack tip gliding force which drives the dislocation from crack tip to its current position. The ledge energy equals the surface energy of the extra step emerging at the crack tip due to dislocation emission. The effect of two dislocation pile-up branches is evaluated by superposition. The effect of blunting is simply considered by approximating the effective decrease of the crack tip stresses. The maximum stress at the crack tip as a function of local stress intensity factor is

$$\sigma_{tip} = \beta \frac{k_I}{\sqrt{nb}}, \tag{2.12}$$

where β is a geometry factor for a notch with semicircular front and nb is the blunting radius caused by n dislocations with Burgers vector b. The competition between crack advance and dislocation emission as the applied stress intensity increases ultimately leads to cleavage failure of the metal layer. Cleavage failure is assumed to occur when the crack tip stress σ_{tip} has reached the cohesive strength of the material. The applied stress intensity at this condition is the fracture toughness. The expression for the fracture toughness-layer thickness dependence that is deduced from the model by Hsia et al. (1994) shows the proportionality

$$K_{Ic} \sim \frac{\sqrt{h}}{\ln \frac{h}{r}} \tag{2.13}$$

for large layer thicknesses neglecting contribution from surface energy. Furthermore the model demonstrates that the fracture toughness scales as

$$K_{Ic} \approx \sigma_{th}^2. \tag{2.14}$$

and thus is very sensitive to the cohesive strength.

2.4.2 Strength of nanocrystalline materials

The influence of interfaces on the mechanical deformation behavior of composite materials has drawn much attention in the last decades, see e.g. (Llorca et al., 1991). It is also evident that in nanostructured materials the behavior of the interface dominates the overall material performance as the interface-area-to-volume ratio is low. As a rule of thumb one can speak of interface-controlled materials, if the characteristic length scales are of the order of one micrometer and below. Deformation and failure of such materials are largely determined by the properties of the interfaces and by size effects of plasticity in the crystalline domains. Microstructural processes such as delamination of the interface, dislocation nucleation and dislocation movement depend on the interfacial properties as well as on the spatial distribution of the interfaces. Structural refinement by severe plastic deformation is a well-known process in the field of interface engineering to strengthen materials (Höppel et al., 2004). For metals at low and intermediate temperatures this strengthening is related to the plastic confinement caused by interfaces due to the presence of particles or grain boundaries in the initial structure. The controlling factors of interfaces on the deformation of polycrystals appear in a wide variety of forms. Temperature and characteristic microstructural length scales play significant roles in determining the mechanical properties. A central research field has therefore emerged for the study of the structure and properties of interfaces as their design is essential for the microstructural evolution during plastic deformation and controls the ultimate macroscopic bulk properties such as strength and toughness.

Recently, ultra fine grained and nanocrystalline metals as well as nanocomposites are under extensive research. Ultra fine grained bulk materials with grain sizes between $100 - 300\,\mathrm{nm}$ have been fabricated based on severe plastic deformation, see (Höppel et al., 2004; May et al., 2005). The resulting nanostructured bulk materials have homogenous and equiaxed microstructures with high fraction of high-angle grain boundaries. The production of nanocomposites (Veprek, 1999; Kauffmann et al., 2005) and nanocrystals (Wang et al., 2002; Chen et al., 2006) with microstructural sizes in the range of $50 - 100\,\mathrm{nm}$ is currently seen to be very promising to achieve extremely high strength and extraordinary hardness. Nanocomposites that are candidates for superhard materials consist of at least two phases with a well-defined microstructure. The predominant phase provides enhanced stiffness and effectively hinders the generation and motion of dislocations. The minority phase should inhibit sliding of grain boundaries (Veprek, 1999). Potential engineering applications include friction and wear resistant cutting tools (tungsten/cobalt composite). Other prominent biphase nanocomposite coatings consist of aluminum metal phases and ceramic fibers, especially silicon carbide, but also aluminum oxide or aluminum nitride, and have a big potential for solving tribological problems in the automotive industry.

There has been a number of experimental studies on the deformation behavior of nanocrystals with average grain size less than $100\,\mathrm{nm}$ (Kauffmann et al., 2005; Wang et al., 2002; Yip, 1998; Arzt, 1998; Chen et al., 2006). These investigations show generally an increasing yield stress and hardness with decreasing grain sizes down to $20\,\mathrm{nm}$. For several materials an inverse Hall-Petch effect has been reported for grain sizes below 10 nm, where strength seems to decrease with further grain refinement (e.g., (Volpp et al., 1997)). It is assumed that in this regime deformation is mainly accommodated by grain boundary sliding (M.A. Meyers, 2006; Weertman, 2000) and J.R. Weertman in (Koch, 2002). Furthermore, the failure strain is found to decrease when grain refinement reaches the nanocrystalline regime. However, there is a great deviation in the data obtained experimentally and strength measurements seem to be significantly affected by imperfections in the material. A survey on experimental measurements indicating an inverse Hall-Petch behavior of the strengths of nanocrystalline materials is given by J.R. Weertman in (Koch, 2002). The decrease in strength in some of these experiments has been attributed to the presence of flaws, especially when samples were used repetitively and different grain sizes were obtained by intermediate annealing, which generally not only increases the grain size, but also reduces the density of other defects (M.A. Meyers, 2006; Weertman, 2000).

While the yield strength is defined as the resistance to macroscopic yielding due to dislocation glide, toughness gives structural materials adequate strength in the presence of crack-like defects. Maximizing both properties designing strong and tough materials is a crucial task in materials engineering. As a typical trend, increasing the materials strength leads to a decrease in the toughness, as higher toughness is achieved by enhancing the plastic work done during formation and propagation of cracks. Novel approaches for the development of strong and tough materials is particularly shaped by interface engineering and biomimetic design. Many natural nanocomposite materials, such as spider silk or nacre, are ideal examples for strong and tough materials. These structural materials achieve extraordinary properties by, first, the unique properties of soft organic phases confined between hard platelets, second, microstructure (size, shape of platelets), and third, molecular interactions at the organic-inorganic interface. Nacre, also known as mother-of-pearl, is the iridescent layer found inside some mollusk species such as oyster or abalone. It is made of relatively weak materials, but due to its hierarchical microstructure, its macroscopic mechanical properties are far superior to those of its constituents. For this reason there is a great interest in nacre as a source of inspiration for novel designs of composites.

Part of the motivation for the present work comes from the increasing evidence that the superior strength and toughness of biological materials including nacre, bone and tendon may be attributed to a generic parallel staggered arrangement of their microstructure (Landis, 1995; Menig et al., 2000; Gao et al., 2003). The abalone shell, which is a composite of mineral plates sandwiched by protein-rich organic materials, has a fracture resistance 3000 times higher than that of the mineral plates (Currey, 1977; Jackson et al., 1988). Inspired by such generic microstructure of biological materials, (Ji et al., 2004) have investigated the flow stress of a metal matrix composite (MMC) with a biomorphous microstructure similar to that of nacre. Such metal matrix composite would be made of staggered hard and slender nanoparticles embedded in a ductile matrix. Ji et al. (2004) showed that the large aspect ratio and the nanometer size of inclusions in the biomorphous MMC lead to significantly improved properties with increased tolerance of interfacial damage. For example, it was found that partially debonded inclusions continue to carry mechanical load transferred via longitudinal shearing of the matrix material between neighboring inclusions. The larger the inclusion aspect ratio, the larger is the flow stress and work hardening rate for the composite. Increasing the volume concentration of inclusion also makes the biomorphous MMC more tolerant of interfacial damage.

The work by Ji et al. (2004) was based on continuum plasticity theory which can not capture the size effect of plastic deformation at micron and submicron length scales (Gao et al., 1999). In the present work (chapter 5), we investigate a fully atomistic model of a similar metallic nanocomposite structure with the aim to study size dependent material properties over a wide range of length scales with a fully atomistic resolution of the material and thus without any a priori assumptions of the deformation processes.

3 Mesoscopic modeling of interface controlled small scale plasticity

Interface controlled small scale plasticity problems such as crack tip plasticity under geometrical confinement are complex, because they involve mixed displacement and traction boundary conditions, which, moreover, dynamically change during crack growth processes following crack path and crack tip geometry. Therefore the solutions to these problems are not trivial and require efficient computational techniques. This chapter demonstrates how these techniques are applied to study fracture processes under plastic confinement as well as deformation of dual phase metal matrix composites.

In the two dimensional discrete dislocation models considered here, the microstructure of a solid and the internal elastic fields are associated with a number of discrete dislocations and cracks within a process window, see Figure 3.1. The process win-

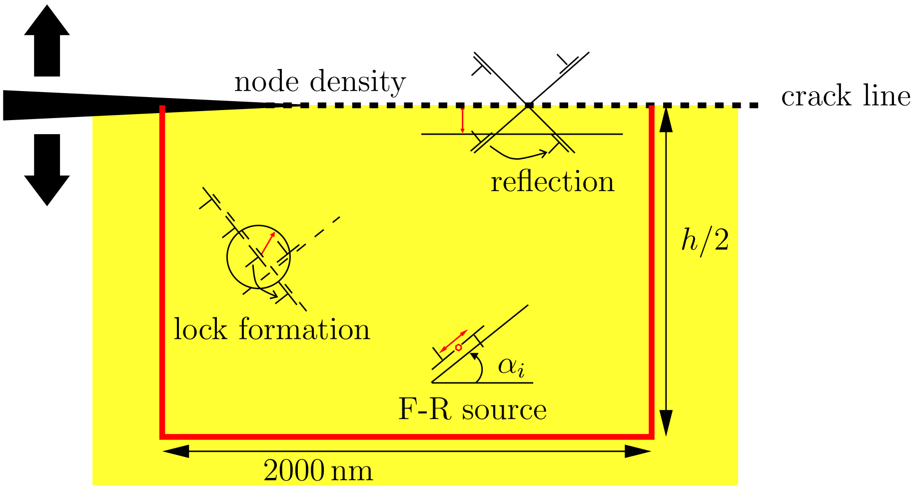

Figure 3.1: Schematics of process window (red box) for the equivalent symmetric crack problem, see text. Shown are the elementary dislocation processes around an initial crack in the two dimensional model. Critical distances for dislocation-dislocation interaction and dislocation-interface interaction are marked in red.

dow describes the dislocation activity in the vicinity of the tip of a plane strain mode I crack. The region shown is the lower half of the equivalent symmetric crack problem (see following section). The crack line is modeled as a cohesive zone and characterized by a traction-separation law. The material is assumed to be a linear elastic, isotropic body $\mathcal{B}$ in which plasticity is carried by dislocation motion. Edge dislocation dipoles are generated from pre-defined two dimensional Frank-Read (F-R) sources. The dislocation structures are assumed to extend infinitively long into the line direction (out of plane) of the dislocations. This motivates the plane strain approximation. In response to the thermodynamic force acting on each individual dislocation, i.e. by the Peach-Koehler (3.8) force which is proportional to the local resolved shear stress at the position of the dislocation, the entire microstructure evolves in time and space. The driving force for dislocation motion is assumed to be completely described within the framework of linear elasticity. In the simulation procedure the evolution of the dislocation microstructure is characterized by nucleation of dislocations at F-R sources, dislocation motion,lock formation and dissociation, annihilation of dislocations and dislocation reflection at the crack line due to the mirror symmetry. For the pure mode I crack analyzed in this work, it is convenient to take advantage of the mirror symmetry of the domain with respect to the crack line so that the problem is reduced to the analysis of the lower half plane. A mirror symmetry line is characterized by the fact that the tangential tractions vanish. In less symmetric crack arrangements mixed mode interactions are usually present, i.e. both normal and shear tractions are induced on the crack line.

3.1 Basic simulation procedure

The evolution of the dislocation microstructure in the vicinity of cracks is computed from a chosen initial configuration based on an explicit time integration scheme. The time step of the integration algorithm is restricted to resolve dislocation-dislocation interaction on a very small scale. Since the time step needs to be small because of near-field dislocation interaction (annihilation, lock formation) an explicit time-stepping algorithm is adopted for the overall solution procedure, see the flowchart in Figure 3.2. The positions ξ^k of dislocations $k = (1...N)$, where N is the total number of dislocations, are incrementally updated over time t as

$$\xi^k_{t+\Delta t} \rightarrow \xi^k_t + \Delta t \mathbf{v}^k_t \tag{3.1}$$

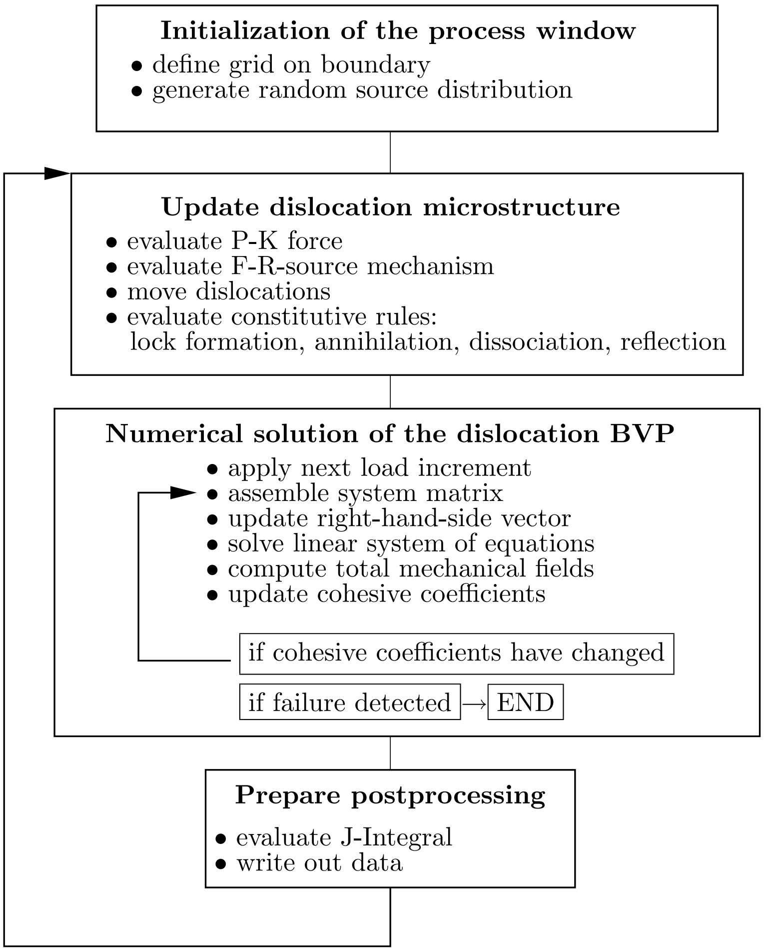

Figure 3.2: Flowchart showing simulation procedure.

where Δt is the current time step and $\mathbf{v}_t^k$ is the current velocity that is taken to be proportional to the acting driving force. After each time step the mechanical equilibrium is solved numerically for the new updated dislocation configuration $\xi_{t+\Delta t}^k$. The total computational time of this procedure relies very much on the efficient evaluation of the dislocation boundary value problem.

3.1.1 Initialization

At the beginning of the simulation a process window is created in which the evolution of the dislocation microstructure is described. The numerical solution of a dislocation boundary value problems requires the discretization of the crack line into a number of boundary elements. Following the domain truncation strategy, a computational interval is defined on the crack line that is large enough, so that the numerical error is small in the domain of interest, i.e. the process zone in the vicinity of the crack tip. The number of integration points used in the simulations is about 1000 leading to a system matrix of the dimension 2000 times 2000 as seen later. The integration points are very dense in the process region having a constant spacing of $8b$. The process region (Figure 3.1) has a dimension of 2000 nm in the direction of the crack line. In the process region, the moving dislocations are expected to interact strongly with the crack. They may be absorbed if they run into the traction-free crack surface or mirrored where the material is still coherent. The boundary of the remaining crack line is more coarsely discretized with increasing spacing between the nodes, approximating an infinitely long crack line and cohesive zone. The plastic deformation around the crack tip develops from a distribution of Frank-Read dislocation sources with density ρ_{src} and strength σ_{src} corresponding to the yield stress. Two slip planes at angles of $\alpha_1 = 45^{\circ}$ and $\alpha_1 = -45^{\circ}$ with respect to the crack line are considered. Initially a randomly distributed source configuration is generated keeping a minimum distance of $10b$ between neighboring slip planes that are associated with the F-R sources.

3.1.2 Updating dislocation microstructure

The Update of the dislocation microstructure involves the evaluation of the Peach-Koehler (P-K) force, the nucleation of dislocations, from Frank-Read (F-R) sources, the motion of the dislocations, and the evaluation of constitutive rules that take care of elementary dislocation processes, see Figure 3.1.

Evaluation of the Peach-Koehler force

In the general framework of defect mechanics, the microstructural evolution is governed by the variation of the total potential energy with respect to changes of the individual defect positions. This generic concept can be applied to various types of defects, however, due to their significance to small scale plasticity, discrete dislocation models have advanced most of all in recent years. An isotropic linear elastic body $\mathcal{B}$ is considered containing a number of N defects at positions ξ^k. The defects induce elastic eigenstrains $\boldsymbol{\varepsilon}^*$ in the lattice and may interact with boundaries or interfaces via elastic image fields (Eshelby, 1951). These image fields contribute to the local stresses and hence to the total driving force that moves the defect. They depend on the defect locations ξ^k and may become the major contribution to the driving force when the defects migrate in the vicinity of boundaries and interfaces. For example, dislocations tend to be pulled into a free surface or are repelled

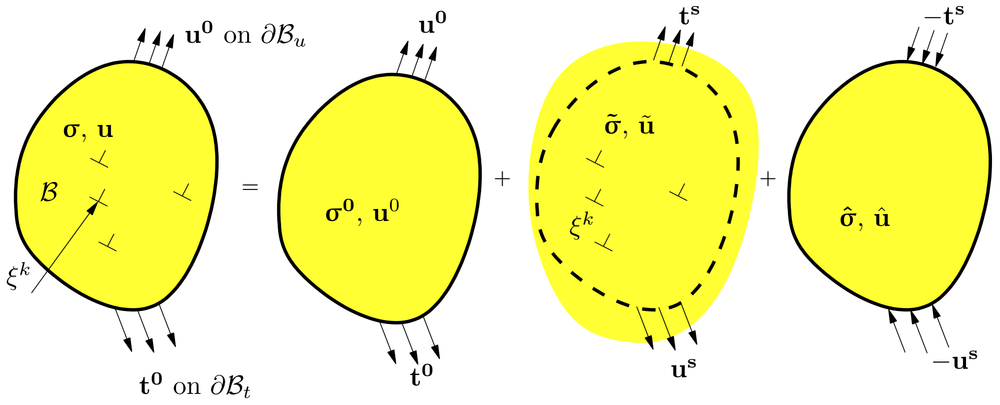

Figure 3.3: General boundary value problem of a finite body with dislocations and decomposition into subproblems.

from interfaces towards stiffer materials. In the framework of linear elasticity the defects are represented by singularities in an unbounded linear elastic domain. The close-form solutions for their stresses and displacement fields can be found in the literature, see (Eshelby, 1951; Mura, 1982). For example, the simplest singularity in elasticity is the center of dilatation which can be considered as a model for an interstitial atom.

The elastic image fields stemming from the presence of material interfaces are determined by formulating and solving a boundary value problem of a finite or semi-infinite body containing a number of defects subject to arbitrary complex boundary conditions, see Figure 3.3. Assuming the solid to be linear elastic and neglecting body forces the singular field can be subtracted from the original boundary value problem by virtue of the principle of superposition. The remaining auxiliary problem of a finite defect-free body under modified boundary conditions has to be solved numerically. The original dislocation boundary value problem is therefore decomposed into a finite body without defects subject to the prescribed boundary conditions $\mathbf{t}^0$,$\mathbf{u}^0$, a problem of a number of defects located in an unbounded domain and an auxiliary problem. In the auxiliary problem the finite defect free body is subject to boundary conditions stemming from the singular fields $\tilde{(.)}$. Tractions $\mathbf{t}_s$ and displacements $\mathbf{u}_s$ at the boundary are compensates by equal loads on $\partial\mathcal{B}$ with opposite sign. The full set of equations specifying the general dislocation boundary value problem are summarized as follows:

$$\begin{array}{rclrclrcl}
\nabla\cdot\bar{\boldsymbol{\sigma}} &=& \mathbf{0} & \nabla\cdot\tilde{\boldsymbol{\sigma}} &=& \mathbf{0} & \nabla\cdot\hat{\boldsymbol{\sigma}} &=& \mathbf{0}\\
\bar{\boldsymbol{\sigma}} &=& \mathbf{C}:\bar{\boldsymbol{\varepsilon}} & \tilde{\boldsymbol{\sigma}} &=& \mathbf{C}:(\tilde{\boldsymbol{\varepsilon}}-\boldsymbol{\varepsilon}^*) & \hat{\boldsymbol{\sigma}} &=& \mathbf{C}:\hat{\boldsymbol{\varepsilon}}\\
\bar{\boldsymbol{\varepsilon}} &=& \frac{1}{2}(\nabla\bar{\mathbf{u}}+\nabla^T\bar{\mathbf{u}}) & \tilde{\boldsymbol{\varepsilon}} &=& \frac{1}{2}(\nabla\tilde{\mathbf{u}}+\nabla^T\tilde{\mathbf{u}}) & \hat{\boldsymbol{\varepsilon}} &=& \frac{1}{2}(\nabla\hat{\mathbf{u}}+\nabla^T\hat{\mathbf{u}})\\
\bar{\mathbf{u}}|_{\partial\mathcal{B}_u} &=& \mathbf{u}^0 & \tilde{\mathbf{u}}|_{\infty} &=& \mathbf{0} & \hat{\mathbf{u}}|_{\partial\mathcal{B}_u} &=& -\mathbf{u}^s\\
\bar{\mathbf{t}}|_{\partial\mathcal{B}_t} &=& \mathbf{t}^0 & \tilde{\mathbf{t}}|_{\infty} &=& \mathbf{0} & \hat{\mathbf{t}}|_{\partial\mathcal{B}_t} &=& -\mathbf{t}^s
\end{array} \tag{3.2}$$

Each subproblem is specified by three sets of equations, i.e. the balance of forces, the constitutive relation where $\mathbf{C}$ is the elasticity tensor, the kinematical relation between strains and displacements, and the boundary conditions which need to be defined on the whole boundary $\partial\mathcal{B} = \partial\mathcal{B}_u + \partial\mathcal{B}_t$. Bold symbols denote vector or tensor quantities. Symbols $\nabla(.)$ and $\nabla\cdot(.)$ denote the gradient and divergence operator, respectively. The symbol $(.) : (.)$ denote the inner product between two tensors of higher rank. The total stress, strain and displacement fields can be determined from the superpositions $\boldsymbol{\sigma} = \bar{\boldsymbol{\sigma}} + \tilde{\boldsymbol{\sigma}} + \hat{\boldsymbol{\sigma}}$, $\boldsymbol{\varepsilon} = \bar{\boldsymbol{\varepsilon}} + \tilde{\boldsymbol{\varepsilon}} - \boldsymbol{\varepsilon}^* + \hat{\boldsymbol{\varepsilon}}$ and $\mathbf{u} = \bar{\mathbf{u}} + \tilde{\mathbf{u}} + \hat{\mathbf{u}}$. Knowing the closed form solution of a single defect, the solution for $\tilde{\boldsymbol{\sigma}}$ and $\tilde{\mathbf{u}}$ of the second subproblem can be obtained by simple summation over all defects. The third subproblem is used to correct the boundary conditions on the boundary $\partial\mathcal{B}$ and usually requires a numerical solution procedure such as finite element (FEM) or boundary element methods (BEM).

After specifying the general dislocation boundary value problem the total potential energy of the body $\mathcal{B}$ can be written in an integral form

$$\begin{aligned}
\Pi &= \frac{1}{2}\int\limits_{\mathcal{B}} \big((\bar{\boldsymbol{\sigma}}(\mathbf{x}) + \tilde{\boldsymbol{\sigma}}(\mathbf{x}) + \hat{\boldsymbol{\sigma}}(\mathbf{x})) : (\bar{\boldsymbol{\varepsilon}}(\mathbf{x}) + \tilde{\boldsymbol{\varepsilon}}(\mathbf{x}) - \boldsymbol{\varepsilon}^*(\mathbf{x},\xi^k) + \hat{\boldsymbol{\varepsilon}}(\mathbf{x}))\big)\, dV\\
&\quad - \int\limits_{\partial\mathcal{B}} \mathbf{t}^0(\mathbf{x})\cdot(\bar{\mathbf{u}}(\mathbf{x}) + \tilde{\mathbf{u}}(\mathbf{x}) + \hat{\mathbf{u}}(\mathbf{x}))\, dA.
\end{aligned} \tag{3.3}$$

The defect positions ξ^k enter the potential by the dependence of the eigenstrain distribution $\boldsymbol{\varepsilon}^*(\xi^k)$. For a number of n defects the eigenstrain distribution can be written as

$$\boldsymbol{\varepsilon}^*(\mathbf{x},\xi^k) = \sum_{k=1}^{n} \delta(\mathbf{x}-\xi^k)\mathbf{G}, \tag{3.4}$$

where the discreteness of the defect distribution is mathematically represented by the Dirac function $\delta(\mathbf{x}-\xi^k)$. $\mathbf{G}$ is a tensor function in general. In the simple case of a center of dilatation, $\mathbf{G}$ simply reduces to the unit tensor $\mathbf{1}$. For a specific eigenstrain distribution the expression (3.3) can usually be simplified by considering the symmetry of the elasticity tensor in conjunction with the common techniques in continuum mechanics to convert integral equations. The thermodynamic driving forces are derived from the variation of the total potential energy

$$\delta\Pi = \sum_{i=1}^{n} \frac{\partial\Pi(\xi^k)}{\partial\xi_i} \cdot \delta\xi_i \tag{3.5}$$

as

$$\mathbf{f}_i = -\frac{\partial\Pi(\xi^k)}{\partial\xi_i}. \tag{3.6}$$

This general expression may be used to derive driving forces for various types of defects by performing the variational calculus for a given eigenstrain distribution $\boldsymbol{\varepsilon}^*(\mathbf{x}, \xi^k)$ that represents a certain type of defect.

The 2D DD model described in this work considers plane strain situations of edge dislocations in isotropic elastic media. The dislocations are only allowed to move on fixed slip planes as rigid entities. The self energy is therefore independent of their locations. The eigenstrain of a dislocation line L lying in a slip plane S with unit normal $\mathbf{n}$ can be written as (Mura, 1982)

$$\boldsymbol{\varepsilon}^*(\mathbf{x};\xi) = \frac{1}{2}(\boldsymbol{b} \otimes \mathbf{n} + \mathbf{n} \otimes \boldsymbol{b})\delta[(\mathbf{x} - \mathbf{x}_s)\cdot\mathbf{n}]H[(\xi - \mathbf{x})\cdot(\boldsymbol{\tau} \times \mathbf{n})] \tag{3.7}$$

where $H[.]$ is the Heaviside function, $\boldsymbol{b}$ is the Burgers vector, $\delta(.)$ the Dirac function, $\boldsymbol{\tau}$ is the unit vector tangential to L, $\mathbf{s}$ is a arbitrary point lying on S and ξ is a point lying on L. $(.) \times (.)$ denotes the dyadic product of two vectors. Inserting this expression in (3.3) one obtains with (3.6) the driving force on the dislocation line segment at point ξ for pure dislocation glide as

$$\mathbf{f} = \boldsymbol{\tau} \times (\boldsymbol{\sigma}\boldsymbol{b}), \tag{3.8}$$

which is known as the Peach-Koehler force. The Peach-Koehler force is proportional to the local stress $\boldsymbol{\sigma}$ at the position ξ caused by any type of boundary conditions and internal stresses. The evaluation of the Peach-Koehler force requires solving the problem specified in (3.2). In response to the thermodynamic force $\mathbf{f}$ acting on each individual defect the entire microstructure evolves in time and space. Under the action of an external force the dislocation microstructure evolves such that it minimizes the total potential energy Π. In DD simulations equilibrium configuration are usually not calculated due to computational expenses. Typically the evolution of the microstructure is computed from a chosen initial configuration based on an explicit time integration scheme where all dislocations are displaced simultaneously within a time step.

Dislocation multiplication

New dislocations are assumed being generated through the operation of Frank-Read sources. The initial dislocation segment of a Frank-Read source bows out under the action of a resolved shear stress until a critical Frank-Read configuration is formed. A Frank-Read source is therefore characterized by the critical stress for activation of the Frank-Read process, the time to form the critical configuration and the diameter of the generated dislocation loop. In the two dimensional approximation of our dislocation model, dislocation nucleation by a F-R source mechanism is mimicked by point sources that generate dislocation dipoles representing dislocation loops in three dimensions. The dipole comprises two opposite dislocations with Burger's vectors $\pm\boldsymbol{b}$. At each time step during the simulation, a nucleation criterion is evaluated by considering the stability of a test dislocation dipole with the average nucleation distance

$$l_{src} = \frac{\mu b}{2\pi(1-\nu)\sigma_{src}}, \tag{3.9}$$

where ν is the Poisson ratio and μ the shear modulus. When the resolved shear stress exceeds the source strength σ_{src} a dislocation pair with a equilibrium spacing of l_{src} is generated. If the dipole expands or is at least stable over an initiation time period, a new dislocation dipole is nucleated. The initiation time period is chosen in such a way that a source is not activated by a single dislocation passing by.

Elementary dislocation processes

The P-K force (per unit length) which drives the dislocation in the slip direction is expressed as

$$f_i = \epsilon_{ij3}\sigma_{jk}b_k. \tag{3.10}$$

Following the Einstein summation convention, ϵ_{ij3} is the permutation tensor, b_k is the Burgers vector with norm $b = 0.25\,\mathrm{nm}$ in the examples presented later. The velocity of dislocations is assumed to be in the overdamped viscous glide regime and follows the form

$$v_{gd} = \frac{1}{B}f \tag{3.11}$$

here the drag coefficient B expresses the resistance to dislocation glide.

Elementary processes related to dislocation behavior are incorporated as constitutive rules, including short range interaction between individual dislocations and interactions between single dislocations and boundaries. For the dislocation-dislocation interaction, a critical distance is used as an onset radius below which formation of obstacles or dislocation annihilation is triggered (Essmann and Mughrabi, 1997), see Figure 3.1. Obstacle formation occurs when two dislocations approach on different intersecting slip planes. When their distance falls below the critical distance for dislocation-dislocation interaction, their motion is stopped. Obstacle formation leads to a macroscopic hardening effect in the material. The obstacles act as barriers to the glide of further dislocations such that dislocation pile-ups form behind the two crossing dislocations, exerting an increasing driving force on them. The strength of an obstacle is assumed to be about 50% of the materials cohesive strength. This quantity controls the highest possible magnitude of pile-up stresses within the bulk material due to the formation of locks. The lock is dissociated when the driving force acting on the locking dislocations exceeds the obstacle strength. On the other hand, if two dislocations of opposite Burgers vectors are found to be approaching each other on parallel slip planes within the critical distance, they annihilate and are subsequently removed from the simulation.

When a single dislocation travels across the mirror symmetry line, i.e. the crack line, it is assumed that its mirror counterpart enters the simulation box which ensures that there is no net dislocation slip across the mirror symmetry line. The dislocation is transferred to a slip plane of the alternative type at the same location. This consequently requires that its Burgers vector be rotated accordingly. Thus its shielding effect with respect to the crack tip changes the sign, which in most situations necessitates the update of the system matrix. Oscillations by successive back and forth mirroring of a dislocation must be avoided since that could tremendously slow down the solution algorithm. Hence, a driving force that pushes the dislocation across the crack line is required to be present over the initiation time period before mirroring is actually performed. Furthermore, for the dislocation-boundary interaction, a larger onset distance of $40b$ is considered.

3.1.3 Numerical solution of the dislocation BVP

The evaluation of the Peach-Koehler force requires the numerical solution of a dislocation boundary value problem. The iterative solution procedure is described in detail in section 3.2.1 after the formulation of the underlying dislocation boundary value problem has been given. The cohesive zone introduces a non-linear material response. The convergence of the iteration process is achieved with a semi-implicit predictor-corrector scheme with the small time step indispensable for the dislocation dynamics. The discretized form of the governing equations leads to a linear system of equations that needs to be solves with system matrix and right-hand-side vector. In order to solve the problem for the current loading step and dislocation microstructure $\xi^k_{t+\Delta t}$, first the body is iterated to be in equilibrium with all the current cohesive nodes being held fixed (predictor step). In the second step, the cohesive zone nodes are free to displace according to the constitutive traction-separation law that specifies the cohesive zone model described below. The new system is solved again and the body is found to be in equilibrium when the residual is negligible (corrector step). After the self-consistently mechanical fields have been obtained the J-integral is evaluated and used as a parameter measuring the effective global loading.

3.2 Numerical modeling of failure and deformation problems

A combined discrete dislocation and cohesive zone model is presented that was first developed to study fracture and crack tip plasticity in thin films and layered structures. The combined DD/CZ model links a two-dimensional dislocation dynamics description of plasticity and a cohesive zone description of fracture. The developed method will be illustrated in detail by means of a fracture analysis. It will be shown how dislocation activities near a crack tip are confined in a thin ductile layer sandwiched between two brittle solids and how measurable, macroscopic quantities like flow stress and fracture toughness of the composite material can be derived within the limitations of a two dimensional dislocation model. Later on it will be demonstrated how this method is extended to describe crack initiation from nanometer sized notches, as well as, the deformation of a dual phase metallic nanocomposites considering the possibility of interfacial sliding.

3.2.1 Fracture in confined thin ductile layer materials

Motivation

In this section special attention is paid to the restrictions that a layer geometry imposes on the expansion of the plastic zone and to the resulting fracture toughness of the composite structure. It will be shown that the fracture toughness of a layered material depends critically on the geometry of the structure. Figure 3.2.1 shows a plane strain mode I crack within a thin plastic layer embedded in an elastic matrix.

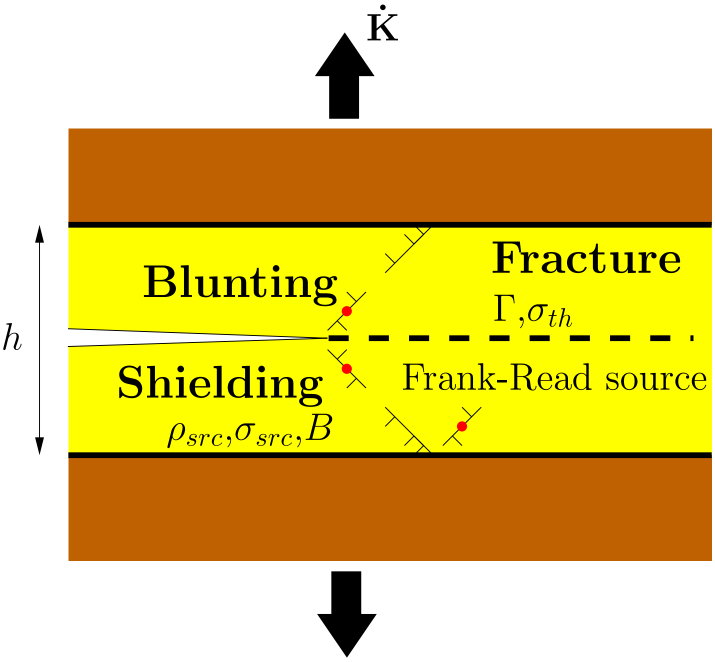

Figure 3.4: An initial crack is located within a ductile layer. The layer thickness and the plastic zone size are the characteristic length scales which control the fracture behavior. See text for annotations.

The region shown is the near tip region of a much larger finite crack with a singular stress field at the left tip (not shown in Figure 3.2.1) and a cohesive zone near the right tip where the crack line is characterized by a traction-separation law with theoretical strength σ_{th} and cohesive energy Γ. The plastic layer and the matrix can have different elastic properties. Dislocations are nucleated at discrete sources within the plastic layer. The intrinsic fracture toughness of the material (i.e. its fracture toughness in the absence of plasticity) is specified by the cohesive energy Γ. The collective dislocation behavior near a crack tip in a ductile layer sandwiched between two brittle solids is analyzed via the developed two dimensional dislocation dynamics (DD) simulations that incorporate a cohesive zone (CZ) model. The cohesive crack tip is treated as part of a much larger finite crack confined in the ductile layer.
The combined DD/CZ model will be formulated by means of boundary integral equations that are based on the Green's function solution of a dislocation near a bimaterial interface (Gutkin and Romanov, 1991; Mura, 1968; Hartmaier et al., 2003).

Simulation description

The simulation starts at zero applied stress with an initially dislocation–free material and the load is increased monotonically with a constant loading rate. A homogenous distribution of Frank-Read sources allows emitting pairs of dislocations when the resolved local shear stress at the source is greater than a source strength for a specific initiation time period. Within the elastic limit below a certain load level, dislocations are absent and the material responds ideal elastic. Beyond this load level, pairs of dislocations are nucleated that move along the slip plane with a velocity obeying the velocity law (3.11).

Dislocation sources close to the crack tip generate a large number of dislocations which, due to the geometrical confinement, pile up at the interface to the elastic matrix. The resulting back-stress prevents further dislocation nucleation in the crack tip region. Dislocations may be attracted by the stress-free crack surface. They are absorbed resulting in a surface step and eliminated from the system. The stress redistribution associated with nucleation and motion of dislocations close to the crack tip causes the driving force for crack extension to change. If the driving force decreases, the dislocation has a shielding character and lowers the local stress intensity factor; otherwise, the dislocation exerts an anti-shielding effect. A change from shielding to anti-shielding is possible since shielding depends on the dislocation position.

At a higher a load level the local stress intensity factor at the crack tip exceeds a critical value and the crack starts to grow under continuous activation of near F-R sources. During this phase the crack behavior is strongly affected by the present dislocation microstructure and the possibility to activate near F-R sources. Eventually at the ultimate load level, the material finally fails by brittle crack propagation. This is detected in the numerical solution procedure if the crack advances unstable without additional load increase. The ultimate remote stress intensity factor where the material finally fails by cleavage is taken as the materials fracture toughness. To deduce the effective shielding factor of the dislocation microstructure the local and the remote stress intensity factors are evaluated though a J-Integral analysis any other ten time steps. The simulations capture the effect of geometrical confinement: as the layer thickness decreases, the crack becomes less shielded and the system behaves in an increasingly brittle fashion. This effect of the layer thickness will be investigated in detail below.

Formulation based on the virtual dislocation technique

The formulation of the model problem and its solution procedure are described as follows. A semi-infinite plane strain mode I crack is assumed to propagate in a thin, ductile layer embedded in an elastic matrix. The crack is subjected to an external load σ_{yy}^{∞} over the entire crack plane. Figure 3.5 shows the boundary value problem of a semi-infinite body with dislocations and a cohesive surface. The crack is modeled as part of the boundary obeying a prescribed cohesive law. The crack length varies with time and is to be determined from the analysis. Assuming the solid to be linear elastic and neglecting body forces, by means of the principle of superposition, the boundary value problem is decomposed into the following three subproblems:

- an infinite, defect-free body subjected to applied remote loads;
- a number of defects with singular fields located in an infinite domain;
- the image fields in a semi-infinite body to correct boundary conditions.

Knowing the closed form solution of a single defect, the solution of the second subproblem can be obtained by simple summation over all defects. The third subproblem is used to correct the boundary conditions on the boundary $\partial\mathcal{B}$. The tractions and displacements at the location of the boundary arising in the first and second subproblems are imposed with the opposite sign to those of a semi-infinite body without defects. The resulting fields of the third subproblem – often regarded as the "image" fields – become the dominant contribution when dislocation interact with the crack tip.

The crack line is modeled as a cohesive zone and assumed to be straight and parallel

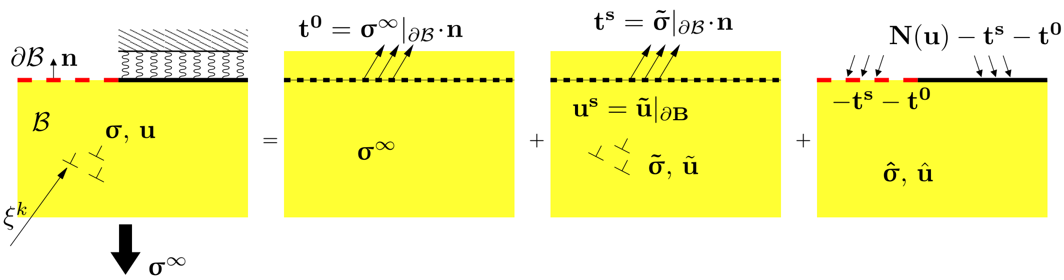

Figure 3.5: The original boundary value problem of a semi-infinite body $\mathcal{B}$ with boundary $\partial\mathcal{B}$ and dislocations. Part of $\partial\mathcal{B}$ with normal vector $\mathbf{n}$ is traction free and the other part is subjected to cohesive tractions. The decomposition leads to an unbounded problem with homogenous fields $(*)^\infty$, an unbounded problem with singular fields $\tilde{(*)}$, and a corrective problem with the image fields $\hat{(*)}$.

to the bi-material interface. Plastic deformation is represented by an evolving ensemble of moving straight edge dislocations. The problem is assumed to be symmetric with respect to the crack plane so that only the lower half needs to be analyzed (see Figure 3.1). Symmetry considerations indicate that on the crack line the tangential tractions vanish

$$\sigma_{xy} = \sigma_{xy}^{\infty} + \hat{\sigma}_{xy} + \tilde{\sigma}_{xy} = 0, \tag{3.12}$$

and the normal displacement ahead of the crack tip remains zero,

$$u_y^{\infty} = 0. \tag{3.13}$$

The normal traction along the crack line can be written as

$$\sigma_{yy} = \sigma_{yy}^{\infty} + \hat{\sigma}_{yy} + \tilde{\sigma}_{xy} = N(\Delta), \tag{3.14}$$

where $\Delta = 2u_y$ is the crack opening displacement and $N(\Delta)$ is the cohesive law specified in the next section. The no-net-dislocation flow condition across the crack line is satisfied by mirroring dislocations instead of propagating them across the crack line.

Cohesive zone model for crack advance

The cohesive zone at the crack tip models the decohesion of the solid along the adjacent atomic crack surfaces ahead of the crack tip. The traction separation (TS) law, a nonlinear stress versus separation relation for decohesion, is one of the key constitutive relations entering in combined DD/CZ model. Two classes of TS-laws have been proposed for implementation, the initially rigid and the initially elastic type, see e.g (Falk et al., 2001). In initially rigid models the cohesive zone is inactive as long as a certain stress level has not been reached. Barenblatt (1962) was the first to propose a cohesive zone model for brittle fracture. The popular model by Dugdale (1960) assumes that the cohesive stress remains constant up to a critical separation distance at which it drops down to zero. The second type of model assumes an initially elastic response of the cohesive zone. Most TS-laws of that type follow a similar scheme: The cohesive traction is zero at the beginning of the deformation. With increasing separation, the traction across the cohesive zone reaches a maximum, then decreases and eventually vanishes allowing for complete decohesion. Crack growth under increasing external loading occurs when the crack surfaces separate gradually to the point where separation at the crack tip exceeds the critical value Δ_c and the cohesive traction vanishes. The applications of the cohesive zone

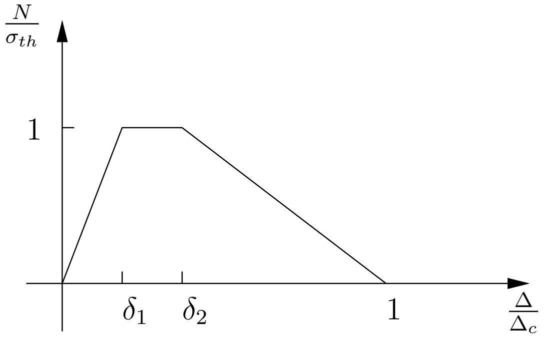

Figure 3.6: TS-law with characteristic parameters including the theoretical strength σ_{th} and the critical crack-tip opening displacement Δ_c. δ_1 and δ_2 are shape parameters giving the fracture energy Γ.

model in this work are reversible. During local unloading of the cohesive element, the same traction curve is followed as during loading. For fatigue studies it would be necessary to consider damage as an irreversible process and unloading should occur in a linear way to the origin. There is an ongoing discussion among researchers working with cohesive zone models whether the shape of the chosen TS-law is of importance, or whether the fracture process depends more or less exclusively on the cohesive strength and energy. In the present work, the material separation near a crack tip is modeled with a simple trapezoidal TS-law which is known to be very appropiate for elastic-plastic materials (Tvergaard and Hutchinson, 1993). The TS-law relates the cohesive normal traction N to the normal separation displacement Δ. In principle, TS-laws of any shape can be implemented with little modification. The reason for choosing a TS-law with straight segments is due to the computational costs. An exponential law would require updating the systems matrix continuously. The shape of the law consists of a rising, a constant and a falling segment and is determined by five parameters; the area under the curve defines the fracture energy

$$\Gamma = 0.5\sigma_{th}\Delta_c(1 - \delta_1 + \delta_2), \tag{3.15}$$

where σ_{th} is the cohesive strength, Δ_c is the crack opening separation above which the cohesive interaction vanishes and δ_1 ,δ_2 are the shape parameters that define the corners of the trapezoid. The variation of the shape parameters controls the initial slope and the slope of the tail, respectively. The corresponding intrinsic fracture toughness for a purely elastic material is obtained as

$$k_{Ic} = \sqrt{\frac{E\Gamma}{1-\nu^2}}. \tag{3.16}$$

In the presence of plastic deformation in the vicinity of the loaded crack tip, higher fracture toughness values are expected due to the elastic shielding of the crack tip.

It is noted that the nucleation of dislocations is influenced by the ratio of the source strength σ_{src} to the cohesive strength σ_{th}.

Numerical solution procedure

Now that we have described the solution strategy that is based on the superposition principle of linear elasticity (Figure 3.5) and having introduced the cohesive zone model (Figure 3.6), this section turns towards the solution procedure for the model problem specified above. The solution procedure for the third subproblem (cf. Figure 3.5) is based on the theory of distributed dislocations where Green's functions are used to construct the corrective stress field (Hills et al., 1996). Consider the schematics of an opened semi-infinite mode I crack parallel to a bimaterial interface with a cohesive surface in front of the crack tip as shown in Figure 3.7. The crack tip is located at the origin of the cartesian coordinate system.

The correcting third subproblem specified above is constructed by introducing a distribution of virtual dislocations along the boundary $\partial\mathcal{B}$. The resulting stress field $\tilde{\sigma}$ due to the virtual dislocation distribution generates the correcting tractions on $\partial\mathcal{B}$.

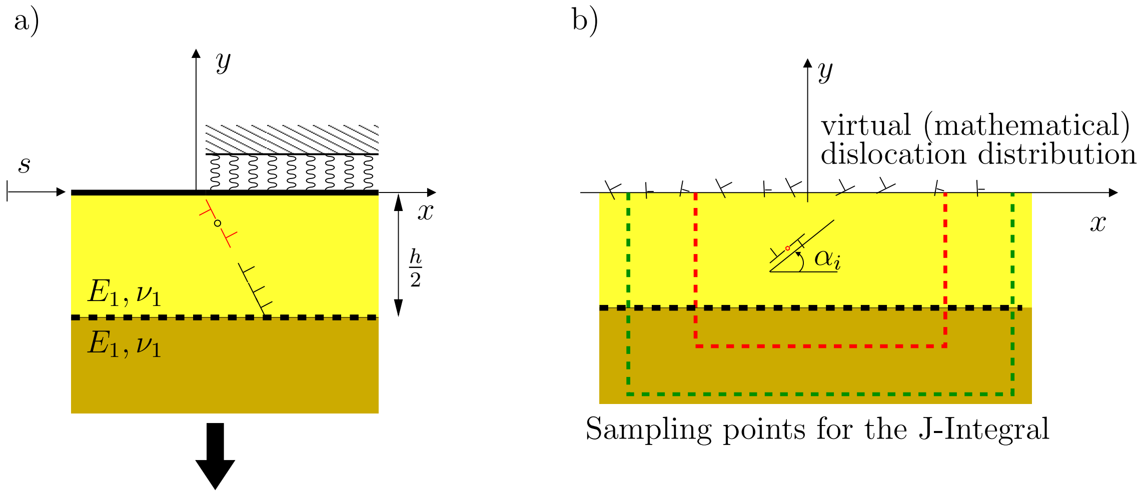

Figure 3.7: Schematics of the model. (a) The equivalent symmetric problem, where only the lower half of the model is analyzed. (b) A sketch of the process zone. The inner (red) frame denotes the process domain where plastic deformation takes place. The crack tip is located at the origin of the cartesian coordinate system. The cut-off length of the virtual dislocation distribution is much greater than the largest expected dislocation shift. The J-integral is used as a parameter measuring the effective global loading. The integration path of the J-Integral (outer frame) lies outside the process domain.

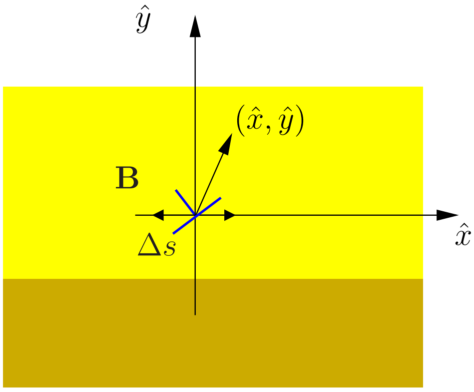

Figure 3.8: Monopole element near a straight bimaterial interface.

On the crack surface, the virtual dislocations create tractions equal but opposite in sign to the surface tractions stemming from the applied loading and the dislocation microstructure in the plastic layer (subproblems 1 and 2). Ahead of the crack tip, the tractions are defined by the cohesive tractions following the traction-separation relation specified above. The resulting displacement jump gives rise to the crack opening displacement. This formulation leads to a system of singular integral equations to determine a vector density of virtual dislocations. The normal traction and displacement fields on the crack line stemming from the virtual dislocation distribution on a straight line are defined by the boundary integrals over the entire crack line (x-axis)

$$\hat{\sigma}_{yy}(x,y) = \int_{-\infty}^{+\infty} [G_{yyx}(x,y,s)B_x(s) + G_{yyy}(x,y,s)B_y(s)]ds, \tag{3.17}$$

$$\hat{\sigma}_{xy}(x,y) = \int_{-\infty}^{+\infty} [G_{xyx}(x,y,s)B_x(s) + G_{xyy}(x,y,s)B_y(s)]ds \tag{3.18}$$

and

$$\hat{u}_y(x,y) = \int_{-\infty}^{+\infty} [M_{yx}(x,y,s)B_x(s) + M_{yy}(x,y,s)B_y(s)]ds, \tag{3.19}$$

where B_x and B_y are the components of the virtual Burgers vector density in tangential and normal direction. The Green's functions G and M are constructed from the basic solution of a single dislocation in the neighborhood of a straight bi-material interface so that the elastic inhomogenity is taken into account (Mura, 1968), see Figure 3.8. The solution for G is described by Hartmaier et al. (2003) and M is constructed in the same way following Gutkin and Romanov (1991) and Mura (1968). To satisfy condition (3.13) the integral over the virtual Burgers vector distribution must be zero, i.e.

$$\int_{-\infty}^{+\infty} B_x(s)ds = 0 \tag{3.20}$$

and

$$\int_{-\infty}^{+\infty} B_y(s)ds = 0. \tag{3.21}$$

After evaluation of the dislocation distribution B_x and B_y that fulfills conditions (3.17) to (3.21), the total stress and displacement fields are computed by superimposing the elastic fields of all virtual and real dislocations together with the applied load. To accomplish this, the system of singular integral equations is evaluated numerically using the boundary collocation method. The distribution of the virtual Burgers vector is defined on boundary elements of constant displacement, such that the boundary conditions are matched at a finite number of points along the crack line. After discretization of the boundary into N elements of segment length Δs^β the discrete tractions and displacements on $\partial\mathcal{B}$ of element α can be expressed as

$$\begin{aligned}\hat{\sigma}_{yy}(x,y) &= \sum_{\beta=1}^{N}\left[G_{yyx}(x,y,s^\beta)B_x^\beta(s^\beta) + G_{yyy}(x,y,s^\beta)B_y^\beta(s^\beta)\right]\Delta s^\beta \\ &= \mathbf{G}_{yyx}(x,y)\mathbf{B}_x + \mathbf{G}_{yyy}(x,y)\mathbf{B}_y,\end{aligned} \tag{3.22}$$

$$\begin{aligned}\hat{\sigma}_{xy}(x,y) &= \sum_{\beta=1}^{N}\left[G_{xyx}(x,y,s^\beta)B_x^\beta(s^\beta) + G_{xyy}(x,y,s^\beta)B_y^\beta(s^\beta)\right]\Delta s^\beta \\ &= \mathbf{G}_{xyx}(x,y)\mathbf{B}_x + \mathbf{G}_{xyy}(x,y)\mathbf{B}_y^\alpha,\end{aligned} \tag{3.23}$$

$$\begin{aligned}\hat{u}_{y}(x,y) &= \sum_{\beta=1}^{N}\left[M_{yx}(x,y,s^\beta)B_x^\beta(s^\beta) + M_{yy}(x,y,s^\beta)B_y^\beta(s)\right]\Delta s^\beta \\ &= \mathbf{M}_{yx}(x,y)\mathbf{B}_x + \mathbf{M}_{yy}(x,y)\mathbf{B}_y,\end{aligned} \tag{3.24}$$

where symbols typeset in boldface represent $(N \times N)$ matrices ($\mathbf{G}$ and $\mathbf{M}$) or N-vectors ($\mathbf{B}$). $\mathbf{B}_x$ and $\mathbf{B}_y$ are accordingly the N-vectors of the x and y-component of the Burgers vector distribution on $\partial\mathcal{B}$.

The unknown stiffnesses of the cohesive zone elements dependent on the current displacement discontinuities and are part of the solution. There is no simple relationship between the tractions and displacements on the crack line which may be used to achieve a linear system of equations to solve the problems numerically. In

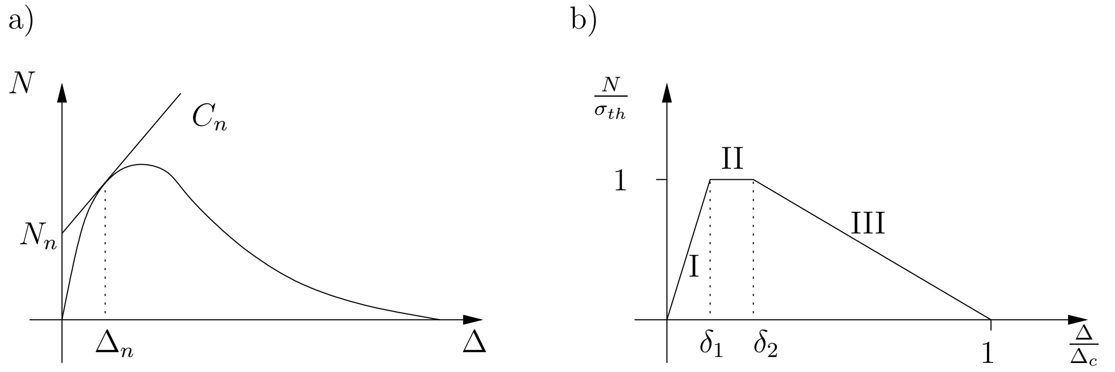

Figure 3.9: a) Schematics of the linearization of a general TS-law $N(\Delta)$ with tangent line at Δ_n, i.e. previous state at time t_n, with offset N_n and slope C_n. b) Characteristic segments of trapezoidal TS-law used in this work, see text.

the strategy followed here, a linear system of equations of the discretized problem is formulated using the stiffness of the cohesive zone material obtained in the previous iteration step. In the general case, see Figure 3.9, the nonlinear stress-separation relationship $N(\Delta)$ of the cohesive elements is linearized at Δ_n, i.e. the previous state at time t_n, as

$$N(\Delta) \approx N(\Delta_n) + N'|_{\Delta=\Delta_n}(\Delta - \Delta_n) = N_n + C_n(\Delta). \tag{3.25}$$

In the implementation of the trapezoidal TS-law which is used in this work, see Figure 3.6, the state of each cohesive element is characterized by the offset N_n and the tangent slope C_n, see Figure 3.9. Depending on the loading state of the cohesive element, the coefficients N_n and C_n are set to

$$N_n = \begin{cases} 0 & \text{segment I} \\ \sigma_{th} & \text{segment II} \\ \dfrac{\sigma_{th}}{(1-\delta_2)} & \text{segment III} \end{cases} \tag{3.26}$$

and

$$C_n = \begin{cases} \dfrac{\sigma_{th}}{\delta_1 \Delta_c} & \text{segment I} \\ 0 & \text{segment II} \\ \dfrac{\sigma_{th}}{(1-\delta_2)\Delta_c} & \text{segment III} \end{cases} \tag{3.27}$$

During the incremental loading the elements pass through the load path prescribed by the TS-law.

With 2N-2 discrete integration, 2N collocation points and the two side-conditions (3.20) and (3.21), the governing equations (3.12)-(3.14) can be written as a system of 2N algebraic equations corresponding to (3.22)-(3.24) in the form

$$\begin{pmatrix} \mathbf{G}_{yyx} - \mathbf{T}_{yyx} & \mathbf{G}_{yyy} - \mathbf{T}_{yyy} \\ \mathbf{G}_{xyx} & \mathbf{G}_{xyy} \end{pmatrix} \begin{pmatrix} \mathbf{B}_x \\ \mathbf{B}_y \end{pmatrix} = - \begin{pmatrix} \boldsymbol{\sigma}^{\infty}_{yy} + \tilde{\boldsymbol{\sigma}}_{yy} - \mathbf{N}_n \\ \boldsymbol{\sigma}^{\infty}_{xy} + \tilde{\boldsymbol{\sigma}}_{xy} \end{pmatrix} \tag{3.28}$$

The matrices $\mathbf{T}_{yyx} = \mathbf{C}_n \mathbf{M}_{yx}$ and $\mathbf{T}_{yyy} = \mathbf{C}_n \mathbf{M}_{yy}$ represent the normal stresses caused by the displacements across the cohesive zone. The linearized representation of the TS-law gives rise to a diagonal matrix $\mathbf{C}_n$ and the vector $\mathbf{N}_n$ that both depend on the loading states of the individual cohesive elements. The element vectors $\boldsymbol{\sigma}^{\infty}$ and $\tilde{\boldsymbol{\sigma}}$ represent the stresses from the external load and the internal stresses stemming from the dislocation microstructure, respectively. The Green's function matrix is validated and inverted at the start of the simulation considering the initial position of the crack. The implementation of the initially elastic TS-law requires the crack path to be specified a priori so that the cohesive elements are distributed over the whole dimension of the crack line. Due to the initial linear response of this cohesive zone model at zero loading, the crack planes separate as soon as loading is applied. The update of the mechanical fields for the updated dislocation microstructure and updated load level at time t_{n+1} are computed from the previous state at time t_n. The effective remote stress intensity factor K_I and the local stress intensity factor K_I are computed from a J-Integral analysis where for K_I the contour of the sampling points is chosen to be far away from the process region, see Figure 3.7.

The system (3.28) is first solved with $\mathbf{C}_n$ and $\mathbf{N}_n$ being taken from the previous time step. In a correcting step it is checked whether the nodal stresses and nodal separations of the elements are consistent with the TS-law and overloaded elements are detected. The transition of an element from one branch of the TS-law to another (cf. Figure 3.6 and (3.26), (3.27)) requires the modification of the cohesive coefficients and a new validation and inversion of the system matrix with an updated matrix $\mathbf{C}_{n+1}$. The stiffness of the cohesive zone material is then modified based on this solution, and the process is repeated until the solution of the desired accuracy is achieved. Accuracy is measured with the residual of the normal stresses, i.e. the difference between the actual normal tractions t_y on the crack line and the imposed stresses $N(\Delta)$ that are prescribed by the TS-law. For a collocation point that lies on the cohesive zone, the traction residual can be written as

$$r = t_y - N(\Delta). \tag{3.29}$$

The convergence of the iterative procedure is achieved with a predictor/corrector scheme with the small time step indispensable for dislocation dynamics. The linear system of equations is usually solved one or two times until the solution is achieved. For points that are in the cohesive zone, both the traction vector and the displacement vector are unknown, but related to each other through the constitutive description of the cohesive zone material provided in (3.25) and (3.26), (3.27). Points on the crack are simply special cases of the cohesive zone with zero stiffness. Suppose that the solution at the previous loading step is known. In order to solve the problem for the current loading step and dislocation microstructure $\xi^k_{t+\Delta t}$, first the solution is iterated till the residual is zero with the known cohesive coefficients taken from the previous loading step (predictor step). In the second step, the cohesive coefficients are updated according to the constitutive laws described above (corrector step). The new system is solved again and the body is found to be in equilibrium when the residual is negligible. This predictor/corrector scheme is found to produce good convergence for the iteration process.

To obtain a physically realistic model a high initial stiffness of the cohesive zone elements is necessary, because otherwise the overall stiffness is reduced and additional deformation will occur. However, a very high stiffness can result in spurious oscillations. Non physical oscillations in the solution for high traction gradient combined with a low order integration scheme has been discussed by Schellekens and de Borst (1999). In this work this behavior has been avoided using mesh refinement. The criterion for crack advance and delamination are both programmed within the iterative process. The incremental loading procedure is indispensable to resolve dislocation dynamics.

3.2.2 Crack initiation from nanometer sized notches

Motivation

Recently pre-cracking methods have been developed for measuring accurate fracture toughness for micro-sized specimens for MEMS applications. With new experimental set ups it is nowadays possible to investigate the effect of grain boundaries on the fracture toughness in bicrystal materials as a function of the distance between the crack tip and the grain boundary (Vehoff, 2007). These researchers prepared micro-cantilever beam type specimens with dimensions of tens of micrometer and introduced notches by focused ion beam machining, see Figure 3.10. The development

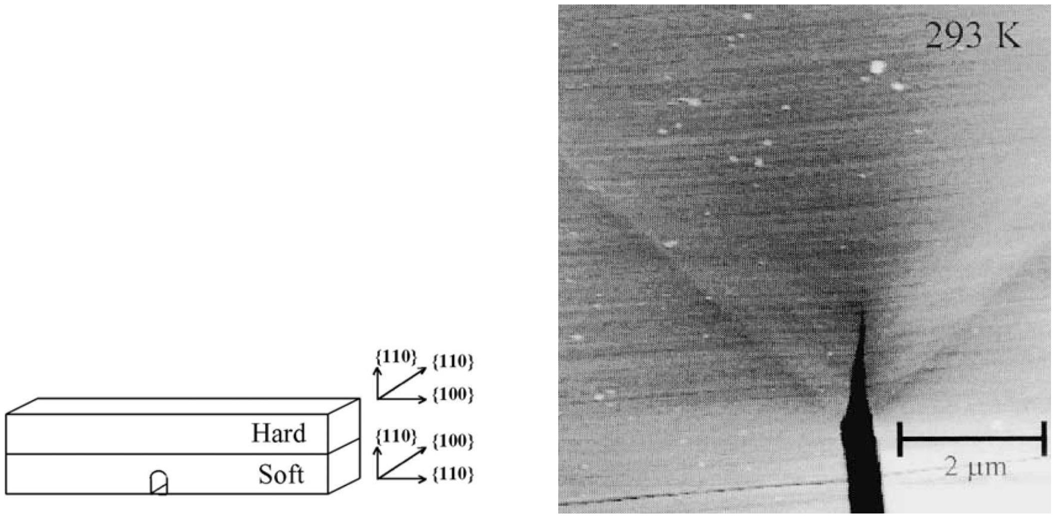

Figure 3.10: Left: Bicrystal fracture speciment (adopted from Vehoff (2007); right: crack tip in a NiAl single crystal as obtained by in-situ straining in a scanning force microscope at 293 K (adopted from Gehling and Vehoff (2002)).

of the dislocation dynamics tool for the simulation of blunted crack tip geometries is motivated by the a discrepancy between experiments and modelling work based on sharp crack tip representation.

Formulation based on distributed displacement discontinuities

In the previous section a straight line with a distribution of virtual dislocations was defined to model the traction boundary value problem of a crack surface within an infinite domain. The loading was represented by a homogenous far field stress. The effective remote stress intensity factor was derived based on a J-Integral analysis on a contour surrounding the crack tip. The model of a blunted crack tip considers a closed contour surrounding a finite domain around the crack tip. This approach was chosen in view of the construction of a simulation cell that describes the deformation of representative volume elements of bulk materials, see next section.

The FIB machined pre-crack tip is modeled as a half circle ahead of the straight crack surface. Under assumption of mirror symmetry with respect to the crack line an equivalent problem is considered as depicted in Figure 3.11. The crack is assumed to grow parallel to the straight pre-crack surface on the x-axis. The whole boundary $\partial\mathcal{B}$ can be separated into two segments $\partial\mathcal{B}_t$ and $\partial\mathcal{B}_u$. $\partial\mathcal{B}_t$ contains the complete crack line with the cohesive zone ahead of the crack tip that is defined in the origin or the (x,y) coordinate system. The straight and the curvilinear crack seg-

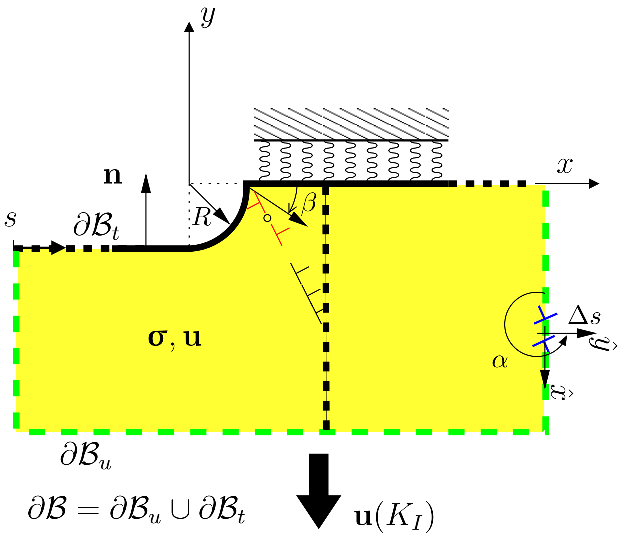

Figure 3.11: Schematics of the blunted crack tip model.

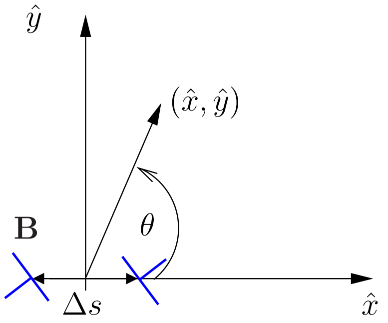

Figure 3.12: Displacement discontinuity element, equivalent to a dislocation dipole, with local coordinate system.

ments are traction free. Cohesive tractions act ahead of the notch on boundary $\partial\mathcal{B}_t$. The loading is prescribed based on the asymptotic K_I-field solution. Displacements

$$u_x^{K_I}(r,\beta) = \frac{K_I}{\mu}\sqrt{\frac{r}{2\pi}}\cos\frac{\beta}{2}(1-2\nu+\sin^2\frac{\beta}{2}), \tag{3.30}$$

$$u_y^{K_I}(r,\beta) = \frac{K_I}{\mu}\sqrt{\frac{r}{2\pi}}\sin\frac{\beta}{2}(2-2\nu+\cos^2\frac{\beta}{2}) \tag{3.31}$$

are implied on boundary segments $\partial\mathcal{B}_u$ denoted in green far away from the crack tip to simulate an acting external far field $\mathbf{u}(K_I)$, where $r = \sqrt{x^2+y^2}$, $\beta = \arctan\frac{x}{y}$. K_I is the mode I stress intensity factor that serves as loading parameter. The equations specifying the mixed boundary value problem for a blunted crack tip with dislocations are summarized as follows:

tractions $\mathbf{t}$ on $\partial\mathcal{B}_t$ displacements $\mathbf{u}$ on $\partial\mathcal{B}_u$

$$\begin{aligned} t_x &= \tilde{t}_x + \hat{t}_x = 0 & \qquad u_x &= \tilde{u}_x + \hat{u}_x = u_x^{K_I} \\ t_y &= \tilde{t}_y + \hat{t}_y = N(\Delta) & \qquad u_y &= \tilde{u}_y + \hat{u}_y = u_y^{K_I}, \end{aligned} \tag{3.32}$$

where tractions are defined as $\mathbf{t} = \boldsymbol{\sigma}|_{\partial\mathcal{B}_t}\cdot\mathbf{n}$. $\Delta = 2u_y$ is the opening of the crack line. The quantities $\hat{(.)}$ and $\tilde{(.)}$ denote the mechanical fields stemming from the real dislocations and displacement discontinuities, respectively.

In contrast to the DD model for straight growing cracks where single dislocation elements (dislocation monopole) were used, now the mechanical fields induced by dislocation dipoles are used as fundamental solutions for the construction of the mixed boundary value problem. This approach allows modeling boundaries of arbitrary shapes in a numerical discretization. However, the use of dislocation dipoles leads to a well defined system of algebraic equations without the need of formulating extra conditions at kinks of adjacent boundary segments or at end points, see also (Hills et al., 1996). The displacement discontinuity element used here for the numerical integration consists of a pair of equal and opposite dislocations that lie in a distance Δs along the axis $\hat{x}$-axis of the local coordinate system $(\hat{x}, \hat{y})$, see Figure 3.12. The two dislocations within an element have the same magnitude, but opposite directions and are equivalent to a constant displacement discontinuity. The discontinuous jump in the displacement field of single dislocations is defined to occur along the connecting line of the two dislocations. Therefore and in contrast to single dislocation elements, the displacement field around a dislocation dipole element is continues. The entire boundary $\partial\mathcal{B}$ in Figure 3.11 is modeled by a discrete distribution of finite displacement discontinuity elements. The influence functions $\bar{G}$, $\bar{M}$ for the displacement discontinuity element can therefore be constructed from the differences of the functions G, M of single dislocations:

$$\begin{aligned}\bar{G}_{ijk}(x, y, s, s) &= G_{ijk}(x, y, s + \frac{\Delta s}{2}, s + \frac{\Delta s}{2}) \\ &\quad -G_{ijk}(x, y, s - \frac{\Delta s}{2}, s - \frac{\Delta s}{2})\end{aligned} \tag{3.33}$$

and

$$\begin{aligned}\bar{M}_{ij}(x, y, s, s) &= M_{ij}(x, y, s + \frac{\Delta s}{2}, s + \frac{\Delta s}{2}) \\ &\quad -M_{ij}(x, y, s - \frac{\Delta s}{2}, s - \frac{\Delta s}{2}),\end{aligned} \tag{3.34}$$

where α is the angle between the global y axis and the local $\hat{y}$ axis. The stress and displacement components in the (x,y) system stemming from the displacement discontinuities can be written as

$$\hat{\sigma}_{ij}(x, y) = \int\limits_{\partial\mathcal{B}} \left[\bar{G}_{ijx}(x, y, s)B_x(s) + \bar{G}_{ijy}(x, y, s)B_y(s)\right] ds, \tag{3.35}$$

$$\hat{u}_i(x, y) = \int\limits_{\partial\mathcal{B}} \left[\bar{M}_{ix}(x, y, s)B_x(s) + \bar{M}_{iy}(x, y, s)B_y(s)\right] ds. \tag{3.36}$$

Dislocation boundary value problems with blunted cracks subject to mode I loading conditions are solved by this displacement discontinuity method in a similar framework presented above. The total dislocation boundary value problem is split into two subproblems, a problem of dislocations embedded in a infinite elastically homogenous body and an auxiliary problem that give rise to the image fields. The boundary is divided into boundary segment which either traction or displacement boundary conditions are known for. In the implementation for the blunted crack tip model all quantities are formulated with respect to the global (x, y)- coordinate system. Tractions t_x, t_y are obtained from the stress components as

$$\begin{bmatrix} t_x(x,y) \\ t_y(x,y) \end{bmatrix} = \begin{bmatrix} \sigma_{xx}(x,y) & \sigma_{xy}(x,y) \\ \sigma_{xy}(x,y) & \sigma_{yy}(x,y) \end{bmatrix} \begin{bmatrix} n_x(x,y) \\ n_y(x,y) \end{bmatrix}. \tag{3.37}$$

Considering the definitions (3.33) - (3.37), the governing equations (3.32) are then solved for the displacement discontinuities B_x,B_y with the collocation method as described above.

Numerical implementation and validation test

The boundary of the finite body considered in the implemented numerical procedure consists of a number of boundary segments. The boundary segments with normal vector $\mathbf{n}$ may be arbitrarily oriented with respect to a global coordinate system. Curvilinear segments, required e.g. to model blunted crack tips, are divided into a number of small straight line segments. In the general case, each line segment may be subject to tractions $\mathbf{t}$, displacements $\mathbf{u}$ or mixed boundary conditions. For the numerical integration of (3.36) all segments are discretized into N boundary elements. Each element i is characterized by the position of the collocation point $\mathbf{x}_i$, the element width Δs_i and a normal vector $\mathbf{n}_i$. The mid points of the elements are taken as the collocation points. The stresses and displacements at the collocation points represent a measure of the average stresses and displacement within the interval Δs.

With 2N discrete integration, 2N collocation points, the governing equations (3.32) - (3.37) can be written as a system of 2N algebraic equations corresponding to (3.22)-(3.24) in the form

$$\underbrace{\left(\begin{array}{cc} \bar{\mathbf{G}}_{xx} & \bar{\mathbf{G}}_{xy} \\ \bar{\mathbf{M}}_{xx} & \bar{\mathbf{M}}_{xy} \\ -\,-\,-\,-\,-\,-\,-\,- & -\,-\,-\,-\,-\,-\,-\,- \\ \bar{\mathbf{G}}_{yx} - \bar{\mathbf{T}}_{yx} & \bar{\mathbf{G}}_{yx} - \bar{\mathbf{T}}_{yy} \\ \bar{\mathbf{M}}_{yx} & \bar{\mathbf{M}}_{yy} \end{array}\right)}_{\text{system matrix } \mathbf{A}} \left(\begin{array}{c} \mathbf{B}_x \\ \mathbf{B}_y \end{array}\right) = \underbrace{\left(\begin{array}{c} -\tilde{\mathbf{t}}_x \\ \mathbf{u}_x^{K_I} - \tilde{\mathbf{u}}_x \\ -\,-\,-\,- \\ \mathbf{N}_n - \tilde{\mathbf{t}}_y \\ \mathbf{u}_y^{K_I} - \tilde{\mathbf{u}}_y \end{array}\right)}_{\text{element vector}} \tag{3.38}$$

The matrices $\bar{\mathbf{T}}_{yx} = \mathbf{C}_n\bar{\mathbf{M}}_{yx}$ and $\bar{\mathbf{T}}_{yy} = \mathbf{C}_n\bar{\mathbf{M}}_{yy}$ represent the normal stresses caused by the displacements across the cohesive zone. The piecewise linear TS-law of the cohesive zone elements is linearized as described in section (3.2.1) and gives rise to a diagonal matrix $\mathbf{C}_n$ and the vector $\mathbf{N}_n$ that both depend on the loading states of the individual cohesive elements.

The computation of the inversion $\mathbf{A}^{-1}$ of the full system matrix, see (3.38), is a major factor for the total computational time in a DD/CZ simulation. Therefore it is important to make use of special properties of $\mathbf{A}$. Note that $\mathbf{A}$ in (3.38) has the block structure

$$\mathbf{A} = \left(\begin{array}{cc} \mathbf{A}_{11} & \mathbf{A}_{12} \\ \mathbf{A}_{21} & \mathbf{A}_{22} \end{array}\right). \tag{3.39}$$

In case of a straight growing crack, only $\mathbf{A}_{21}$ and $\mathbf{A}_{22}$ change when coefficients in $\mathbf{C}$ are modified. The computation of $\mathbf{A}^{-1}$ is computationally more efficient when following decomposition is considered, see e.g. (Steinbach, 2004),

$$\mathbf{A}^{-1} = \left(\begin{array}{cc} \mathbf{B}_{11} & \mathbf{B}_{12} \\ \mathbf{B}_{21} & \mathbf{B}_{22} \end{array}\right), \tag{3.40}$$

where

$$\begin{aligned} \mathbf{B}_{11} &= \mathbf{A}_{11}^{-1} + \mathbf{A}_{11}^{-1}\mathbf{A}_{12}\mathbf{S}^{-1}\mathbf{A}_{21}\mathbf{A}_{11}^{-1} \\ \mathbf{B}_{12} &= -\mathbf{A}_{11}^{-1}\mathbf{A}_{12}\mathbf{S}^{-1} \\ \mathbf{B}_{21} &= -\mathbf{S}^{-1}\mathbf{A}_{21}\mathbf{A}_{11}^{-1} \\ \mathbf{B}_{22} &= \mathbf{S}^{-1} \end{aligned} \tag{3.41}$$

with $\mathbf{S} = \mathbf{A}_{22} - \mathbf{A}_{21}\mathbf{A}_{11}^{-1}\mathbf{A}_{12}$, the Schur complement of $\mathbf{A}$. Note that the numerical effort for the inversion of a matrix of dimension (N*N) scales with N^3 so that the decomposition into block matrices of dimensions $(\frac{N}{2} * \frac{N}{2})$ reduces the effort by factor of 8.

The model for blunted crack tips reduces to the representation of sharp cracks when the blunting radius R is set to zero and the stiffness $C_n = \frac{N}{\delta_1 \Delta_c}$ of the cohesive elements is set to a very large value. The cohesive zone elements respond as rigid springs so that no separation of material is possible ahead of the crack tip. This setup serves to benchmark the implemented model and to check the consistency of this method. The numerical solution for the stress components σ_{xx},σ_{yy} and σ_{xy} are compared with the analytical solution of the asymptotic K_I-field solution

$$\begin{aligned}
\sigma_{xx}^{K_I} &= \frac{K_I}{\sqrt{2\pi r}} \cos\frac{\beta}{2}(1 - \sin\frac{\beta}{2}\sin\frac{3\beta}{2}), \\
\sigma_{yy}^{K_I} &= \frac{K_I}{\sqrt{2\Pi r}} \cos\frac{\beta}{2}(1 + \sin\frac{\beta}{2}\sin\frac{3\beta}{2}), \\
\sigma_{xy}^{K_I} &= \frac{K_I}{\sqrt{2\Pi r}} \cos\frac{\beta}{2}\sin\frac{\beta}{2}\cos\frac{3\beta}{2}, \qquad (3.42)
\end{aligned}$$

where $r = \sqrt{x^2 + y^2}$, $\beta = \arctan\frac{y}{x}$ are cylinder coordinates for a crack along the x-axis. The stresses along the straight line defined by $\beta = 45°$ are plotted in Figure 3.13 and converge with number of elements to the analytical solution (3.42). The deviation for small values of r is a result of the discretization. However, the deviation shows up only within the cut-off distance that is considered for dislocation-interface

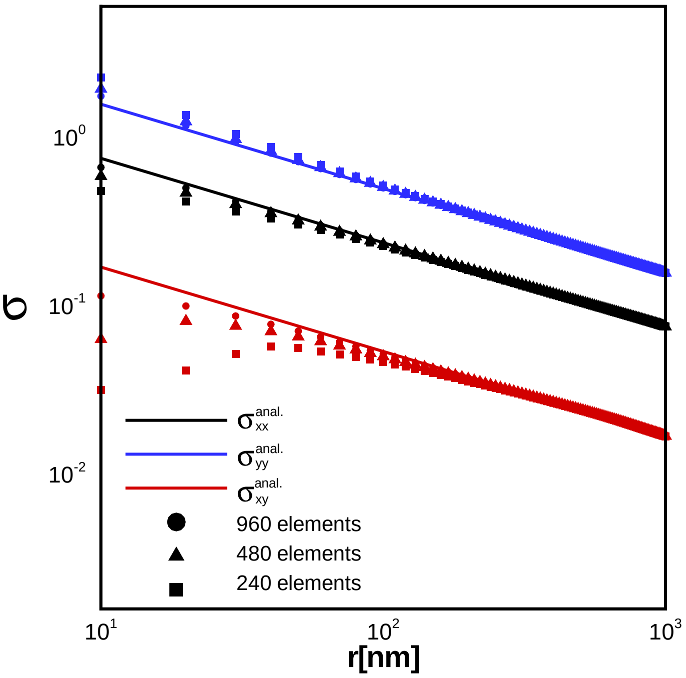

Figure 3.13: Convergence test: comparison of the analytical solution (3.42) with the BEM-solution for different numbers of boundary element. Stresses are plotted along a line with $\beta = 45°$.

interaction in DD simulations. The near crack tip stresses change significantly when the tip is considered to be blunt. The stress intensity vanishes due to the finite curvature of the tip. The normalized stress component σ_{yy} for $R = 200\,\mathrm{nm}$ is shown in Figure 3.14 (left). On top of Figure 3.14 the normalized traction t_y is plotted. The first three boundary elements ahead of the crack tip are in the plateau regime of the TS-law (3.6). The dipole elements in this illustrative example have a constant length. To reduce the number of elements in a DD simulation the element length usually varies along the boundaries. The length is taken to be small (a few b) and constant on the part of the crack line where fracture is expected to occur. On the other boundary segments the stress gradient is small and the element length may increase in order to reduce the total number of elements.

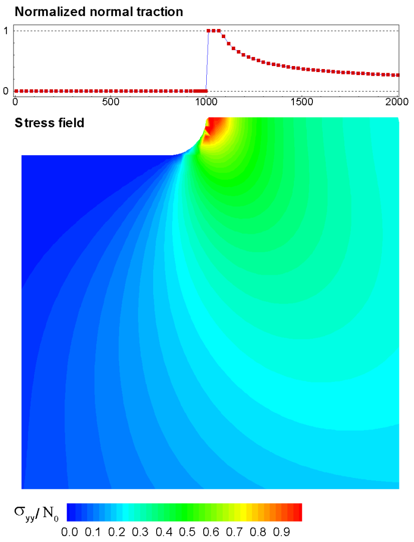

Figure 3.14: The contour plots of the crack opening stress in the simulation box for a blunted crack tip geometry with blunting radius $R = 200\,\mathrm{nm}$. On top, the normal tractions on the crack line are shown, tractions vanish on the free crack surface.

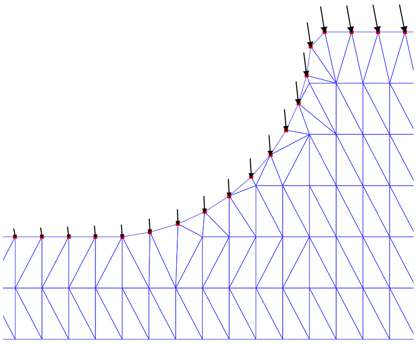

Figure 3.15: Close view on the discretized contour of the crack tip. Shown are the distribution of displacement discontinuities denoted by vectors and the collocation points. The mesh is only used to visualize the stress field, see Figure 3.14.

Influence of blunting radius on plastic zone size

Finite changes in the crack tip geometry significantly affect the stress field around the crack tip and influence crack advance, dislocation nucleation and dislocation migration. For some materials the effect of blunting can be large and might even change the deformation mode from brittle cleavage to ductile dislocation emission. Blunting decreases the local stress concentration and effectively increases the intrinsic toughness. In previous models the effect of blunting has therefore been approximated by assuming the intrinsic fracture toughness to be a function of some blunting parameter, see (Hsia et al., 1994; Rice and Rosengren, 1968). The blunting of the crack tip is taken into account by increasing the intrinsic fracture toughness, i.e. the critical local stress intensity for final fracture. The increase in intrinsic fracture toughness was approximated to be proportional to the number of absorbed dislocations.

The presented model is appropriate to study the effect of crack tip blunting for different crack tip geometries on subsequent crack propagation and dislocation emission. The above procedure may be employed to study either the effect of atomic blunting during dislocation emission from a crack tip source or the re-initiation of a sharp crack from a notch. The implemented procedure is able to handle different assumptions for the crack tip geometry. For the smoothly blunted crack tip that is shown in Figure 3.14 the effect of blunting is large. The loading stress intensity factor K_I, see Figure 3.11, that is required to activate the nearest source to the crack tip is increasing with the blunting radius R.

To illustrate the effect of the blunting radius relaxation simulations were performed for two radii $R = 200\text{nm}$ and $R = 800\text{nm}$, see Figure 3.16 and Figure 3.17. For the simulations with two slip planes at inclination angels $\alpha_1 = 45^\circ$ and $\alpha_2 = -45^\circ$ the system is simply relaxed under a fixed loading of $K_I = 1.1\text{MPa}\sqrt{\text{m}}$. In the final stage dislocations are either in equilibrium or are blocked by the impenetrable grain boundary which is located about 600nm ahead of the crack tip. The result is as could be expected. The stress field decays much slower for $R = 800\text{nm}$ compared to $R = 200\text{nm}$. The tensile stress at the crack tip is also lower as a result of the reduced stress intensity, and thus the loading needed to re-initiate the crack is increased. It is also seen that the higher stress concentration caused by the smaller blunting radius activates more sources in the vicinity of the crack tip. Less dislocations are nucleated near the crack tip with $R = 800\,\text{nm}$ as a result of the lower stress concentration compared to the crack with $R = 200\,\text{nm}$.

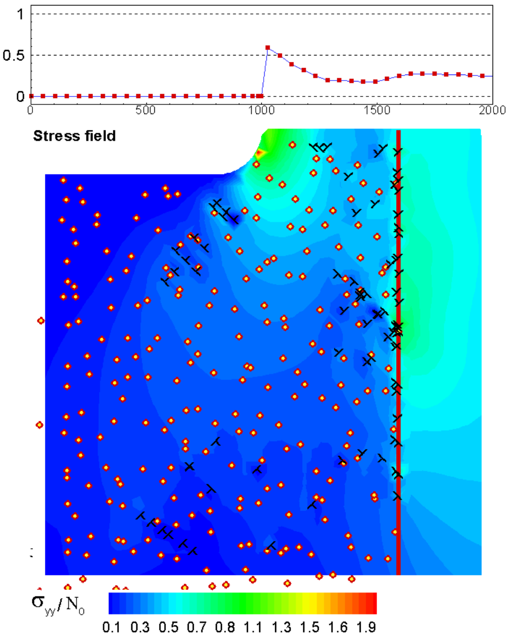

Figure 3.16: Dislocation microstructure for $R = 200\,\text{nm}$ and $K = 1.1\,\text{MPa}\sqrt{\text{m}}$.

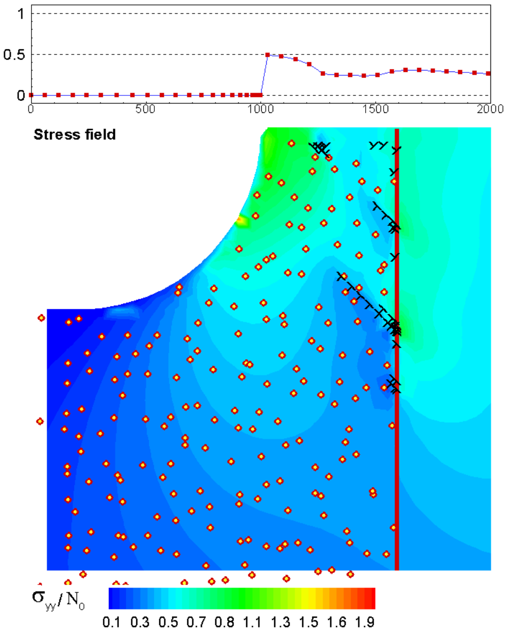

Figure 3.17: Dislocation microstructure for $R = 800\,\text{nm}$ and $K = 1.1\,\text{MPa}\sqrt{\text{m}}$.

3.2.3 Deformation of a dual phase metal matrix composite

Motivation

An important class of interface controlled materials are reinforced metal-matrix composites (MMC) due to their big potential in light weight applications. Typically, fibers or particles of high strength and stiffness are used as reinforcements. For example, SiC particle reinforced aluminum matrix composites achieve high yield stress, high strength and high stiffness. The density of this composite material is decreased by increasing the volume of SiC particles. Various methods for the production of reinforced MMC have been developed in automotive and aircraft industries to improve the mechanical properties of the materials and to gain weight reduction in structural applications. Particle, short fiber and layered MMCs are distinguished according to the characteristics of their reinforcement. One important quantity of the microstructural design of these materials is the aspect ratio of the reinforcement defined as the length over diameter. The aspect ratio is directly proportional to the load transfer from the matrix to the reinforcement. Another critical aspect is the strength of the interfaces between reinforcement and matrix, which is extremely important for the material properties such as strength and toughness.

For the understanding of the strengthening mechanisms in metallic composites due to reinforcements the characteristic length scale of the underlying fiber microstructure is of great importance. In the extreme case of large particles of micrometer size and above the behavior of the composite can be described by conventional continuum plasticity models. The elastic and plastic properties are described in terms of fixed microstructural features, i.e. the matrix and reinforcement properties, the volume fraction, shape and distribution of the reinforcement (Bao et al., 1991; Brockenbrough et al., 1991). Damage initiation can occur either by the cracking of the brittle reinforcements (Corbin and Wilkinson, 1992), or by the failure of the reinforcement-matrix interface (Shen et al., 1995).

There is a range of length scales [100 nm; 1000 nm] where plasticity in MMCs is governed by the nucleation and movement of discrete dislocations within the matrix near the interfaces. The response of dislocations to external loads and to internal fields due to the presence of interfaces dictates the plastic behavior of the matrix in several ways. High stress concentrations due to dislocation pile-ups at material interfaces facilitate additionally interface mediated deformation modes. These sites are initiation spots for interfacial delamination and interfacial sliding that contribute to the plastic deformation by dislocation glide. In turn, local high tensile stresses at the interfaces preferably at corners partially open the interface. Spots of initiating interfacial delamination operate as dislocation sources at low load levels and may provide sinks for dislocation annihilation at higher loads and proceeding damage evolution. The microscale plastic flow processes within the metal phase are not accessible by conventional continuum crystal plasticity formulations. Neither can this size regime be approached by an atomistic analysis. Understanding of the role of interfaces for the strength of MMC can only be reached by simulating discrete dislocation processes interplaying with the stress fields exerted by the interfaces.

So far dislocation dynamics simulations have only been presented for crystalline bulk materials or nanocomposites with coherent interfaces. The grain boundaries or interfaces were characterized by their impenetrability to dislocation motion (Cleveringa and Van der Giessen, 1999; Cleveringa et al., 1997; Biner and Morris, 2003, 2002) and by their discontinuously changing elastic properties across the interface (Cleveringa and Van der Giessen, 1999; Cleveringa et al., 1997). A major shortcoming of these models is the neglect of interfacial damage processes and interface mediated plastic deformation. Interfacial decohesion and interface sliding however have a great effect on the load transfer at the interfaces and, thus, on the ultimate material properties. From physical experiments and atomistic simulations reported in the literature, it is clear that grain-boundary-related slip and separation phenomena play an important role in the overall deformation of nanocomposite and noncrystalline materials when the characteristic length scale decreases under 100 nm and dislocation activities become more difficult. Besides molecular dynamics, only few modeling studies including grain boundary phenomena have been presented, see e.g. (Wei and Anand, 2004). These approaches, however, are on the continuum level and not capable describing discrete dislocation based plasticity in the interior of metal phases of MMC.

The objective here is the development of a simulation tool to study mechanical properties of MMCs with a full resolution of the microscale plastic flow and interfacial glide processes. In the combined DD/CZ model the deformation of a two-dimensional dual phase MMC material is considered. This material contains rectangular hard platelets that are regularly arranged in a soft plastic matrix. The parameter describing the microstructure are the distribution wavelength of the hard particles in the two dimensions, their aspect ratio, as well as, the particle-volume fraction. The objective criterions are the macroscopic strength and toughness that are deduced from the computed stress-strain curves that are the outcome of the analysis.

Implementation of the RVE

The MMC structures are idealized as uniformly distributed periodic arrays of aligned unit cells. Each unit cell consists of an elastic rectangular platelet surrounded by an plastically deforming matrix as illustrated in Figure 3.5. Under external loading, each unit cell is regarded to behave identically. The effective mechanical properties of the model material is then determined by considering a representative volume element (RVE). A RVE is characterized as a lower bound of a microstructural unit cell that is entirely typical for the whole material and that contains a sufficient number of inclusions. The cell should be large enough, so that the computed macroscopic quantities does not depend on the dislocation source configurations and that the deformation due to the motion of dislocations can be regarded as homogenous. To reduce the computation time in practical applications its finite size is chosen as small as possible to limit the area of interfaces. The simulation cell has width w and height h which are the distribution wavelengths of the particles in x and y direction. The reinforcing particles remain elastic with the same modulus as

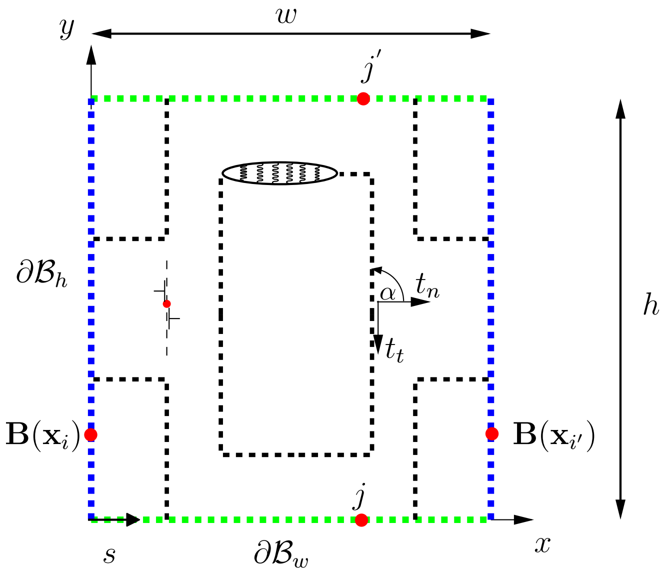

Figure 3.18: Schematics of the periodic simulation cell. Element pairs (i, i') are defined on opposite boundary segments $\partial\mathcal{B}_h$ and $\partial\mathcal{B}_w$.

the soft matrix. To model the behavior of a bulk composite material the unit cell is subjected to pure tension, which is prescribed through the macroscopic boundary condition. Macroscopic stresses and strains are defined in an average sense as

$$\bar{\sigma}_{\alpha\beta} = \frac{1}{2w} \int\limits_{\partial\mathcal{B}_w} \sigma_{\alpha\beta}(s) ds \tag{3.43}$$

To reflect the real bulk situation both a stress field and a kinematic correction need to be implemented for the boundaries of the simulation box, see Figure 3.18. In the formulation only displacement and traction differences $\Delta\mathbf{u}$ and $\Delta\mathbf{t}$ are considered on the boundary.

To ensure the periodicity of the mechanical fields on opposite boundary segments $\partial\mathcal{B}_h$ and $\partial\mathcal{B}_w$, the boundary tractions $\mathbf{t}$ follow the condition

$$\begin{aligned} \Delta\mathbf{t}|_{\partial\mathcal{B}_h}(y) &= \mathbf{t}(x=0,y) - \mathbf{t}(x=w,y) = \mathbf{0} \\ \Delta\mathbf{t}|_{\partial\mathcal{B}_w}(x) &= \mathbf{t}(x,y=0) - \mathbf{t}(x,y=h) = \mathbf{0} \end{aligned} \tag{3.44}$$

and the boundary displacements are forced to satisfy

$$\begin{aligned} \Delta\mathbf{u}|_{\partial\mathcal{B}_h}(y) &= \mathbf{u}(x=0,y) - \mathbf{u}(x=w,y) = w_0 \\ \Delta\mathbf{u}|_{\partial\mathcal{B}_w}(x) &= \mathbf{u}(x,y=0) - \mathbf{u}(x,y=h) = h_0, \end{aligned} \tag{3.45}$$

where h_0 is the loading parameter that controls the macroscopic effective tensile strain

$$E_{yy} = \frac{h_0}{h} \tag{3.46}$$

and w_0 is determined from the condition

$$\bar{\sigma}_{xx} = \frac{1}{2w} \int_{\partial \mathcal{B}_t} \sigma_{xx} \mathrm{d}s = 0. \tag{3.47}$$

Condition (3.47) ensures a uniaxial stress state as the lateral stresses are forced to be zero. The total tractions $\mathbf{t}$ and displacements $\mathbf{u}$ are decomposed additively

$$\begin{aligned} \mathbf{t} &= \hat{\mathbf{t}} + \tilde{\mathbf{t}} \\ \mathbf{u} &= \hat{\mathbf{u}} + \tilde{\mathbf{u}}, \end{aligned} \tag{3.48}$$

where $\tilde{(.)}$ are the known mechanical fields stemming from the dislocation microstructure and $\hat{(.)}$ are the corrective fields that are determined from the auxiliary boundary value problem. For the implementation of the conditions (3.44)-(3.47) with definition (3.48), element pairs $(i, i^{'})$ are defined on opposite sides of the boundaries $\partial\mathcal{B}_t$ and $\partial\mathcal{B}_w$. Each element pair $(i, i^{'})$ is characterized by two collocation points at the positions $\mathbf{x}_i$ and $\mathbf{x}_{i'}$ and 4 degrees of freedom stemming from the displacement discontinuities $\mathbf{B}^{(i)} = \mathbf{B}(\mathbf{x}_i)$ and $\mathbf{B}^{(i^{'})} = \mathbf{B}(\mathbf{x}_i^{'})$. The four necessary equations originating from the periodicity conditions of the traction and displacement components for each element pair $(i, i^{'})$ are

$$\begin{aligned} \Delta u_x^i &= w_0, \text{ if } \mathbf{x}_i \text{ on } \partial\mathcal{B}_h \\ \Delta u_y^i &= 0, \text{ if } \mathbf{x}_i \text{ on } \partial\mathcal{B}_h \\ \Delta u_x^i &= 0, \text{ if } \mathbf{x}_i \text{ on } \partial\mathcal{B}_w \\ \Delta u_y^i &= h_0, \text{ if } \mathbf{x}_i \text{ on } \partial\mathcal{B}_w \end{aligned} \tag{3.49}$$

and

$$\begin{aligned} \Delta t_x^i &= 0, \text{ if } \mathbf{x}_i \text{ on } \partial\mathcal{B} \\ \Delta t_y^i &= 0, \text{ if } \mathbf{x}_i \text{ on } \partial\mathcal{B}. \end{aligned} \tag{3.50}$$

With 2N discrete integration points, the governing equations (3.45) - (3.47) can be written as a system of 2N algebraic equations in the form

$$\underbrace{\begin{pmatrix} \bar{\mathbf{G}}_{tx} - \bar{\mathbf{T}}_{tx} & \bar{\mathbf{G}}_{ty} - \bar{\mathbf{T}}_{ty} \\ \Delta\bar{\mathbf{G}}_{xx} & \Delta\bar{\mathbf{G}}_{xy} \\ \Delta\bar{\mathbf{M}}_{xx} & \Delta\bar{\mathbf{M}}_{xy} \\ -\,-\,-\,-\,-\,-\,-\,- & -\,-\,-\,-\,-\,-\,-\,- \\ \bar{\mathbf{G}}_{nx} - \bar{\mathbf{T}}_{yx} & \bar{\mathbf{G}}_{ny} - \bar{\mathbf{T}}_{yy} \\ \Delta\bar{\mathbf{G}}_{yx} & \Delta\bar{\mathbf{G}}_{yy} \\ \Delta\bar{\mathbf{M}}_{yx} & \Delta\bar{\mathbf{M}}_{yy} \end{pmatrix}}_{\text{system matrix } \mathbf{A}} \begin{pmatrix} \mathbf{B}_x \\ \mathbf{B}_y \end{pmatrix} = \underbrace{\begin{pmatrix} \mathbf{S}_n - \tilde{\mathbf{t}}_t \\ -\Delta\tilde{\mathbf{t}}_x \\ \mathbf{w}_0 - \Delta\tilde{\mathbf{u}}_x \\ -\,-\,-\,- \\ \mathbf{N}_n - \tilde{\mathbf{t}}_n \\ -\Delta\tilde{\mathbf{t}}_y \\ \mathbf{h}_0 - \Delta\tilde{\mathbf{u}}_y \end{pmatrix}}_{\text{element vector}} . \tag{3.51}$$

The matrices and vector quantities $\Delta(.)$ that couple elements on opposite sides of the boundaries are defined as

$$\Delta(.) = (.)(\mathbf{x}_i) - (.)(\mathbf{x}_{i'}) \tag{3.52}$$

$\Delta\bar{\mathbf{G}}$ and $\Delta\bar{\mathbf{M}}$ arise from the periodicity conditions for traction (3.44) and displacement (3.45) components. The matrices $\bar{\mathbf{T}}$ represent the normal stresses caused by the separation of the cohesive zone. The tractions and displacements defined on the cohesive interfaces are now written with respect to normal $(.)_n$ and tangential $(.)_t$ components following the transformation

$$\begin{bmatrix} (.)_t \\ (.)_n \end{bmatrix} = \begin{bmatrix} \cos(\alpha) & \sin(\alpha) \\ -\sin(\alpha) & \cos(\alpha) \end{bmatrix} \begin{bmatrix} (.)_x \\ (.)_y \end{bmatrix} . \tag{3.53}$$

The piecewise linear TS-laws of the cohesive element – now for both normal $N(\Delta_n)$ and tangential components $S(\Delta_t)$, where Δ_n and Δ_t are the normal and tangential opening displacements (see Figure 2.1)– is linearized as

$$\begin{aligned} N(\Delta) &= N_n + C_n\Delta \\ S(\Delta) &= S_n + C_n\Delta \end{aligned} \tag{3.54}$$

for normal and for tangential tractions at the previous time t_n, respectively.

To demonstrate the methodology a test dipole is introduced in the simulation cell in close vicinity to the left boundary as shown in Figure 3.19. The stress fields from the corrective boundary value problem give rise to the periodic image that appears at the opposite right hand side boundary. The displacement discontinuities of each boundary element are denoted as black vector symbols. At the bottom and top boundaries the displacement discontinuities are homogenous due to the applied homogenous stretch h_0. The variation of displacement discontinuities along the right boundary is rather strong due to the close distance of the test dipole to the boundary.

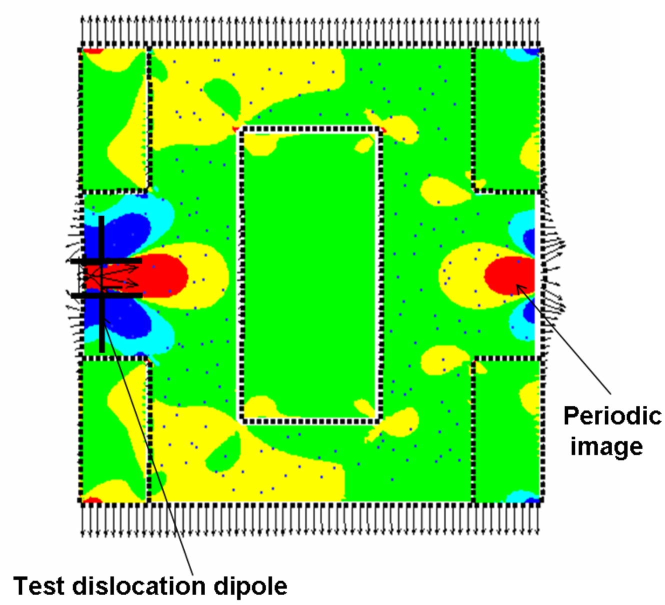

Figure 3.19: Computation of periodic images. Shown is the distribution of the stress component σ_{xx}.

Demonstration for a porous metal material

The model for reinforced dual phase MMC will be illustrated by means of a fictitious porous metal material, see Figure 3.20. To model rectangular pores embedded in a ductile metal matrix the interaction between matrix and reinforcement is set to zero. Only the ductile matrix transfers the applied loading so that effectively a porous metal material is considered. The two materials differ only in the pore volume

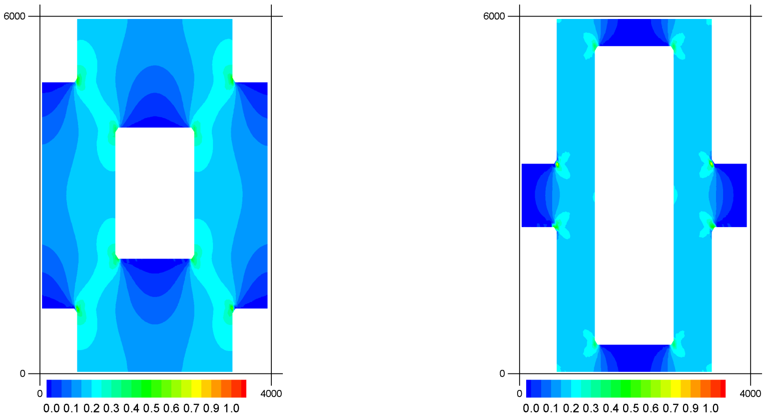

Figure 3.20: Two porous metal materials under loading in the initial state of the relaxation simulation. Shown is the normalized stress component $\frac{\sigma_{yy}}{\bar{\sigma}_{yy}}$.

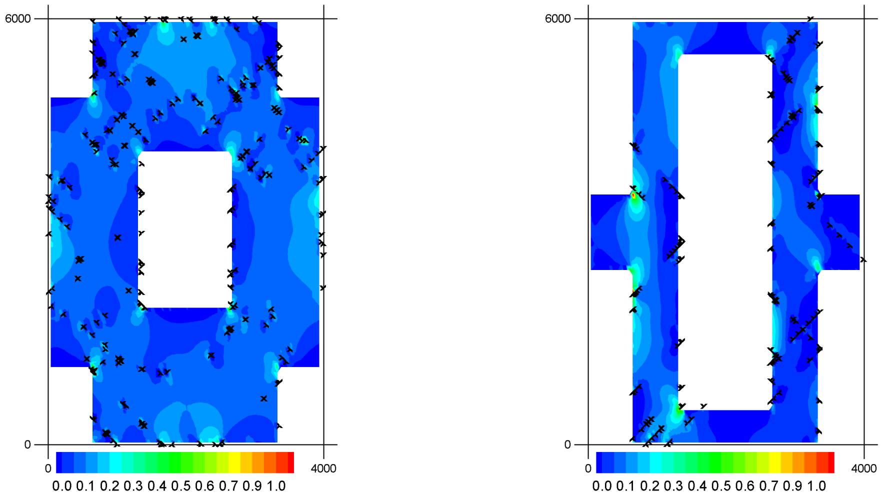

Figure 3.21: The normalized tensile stress $\frac{\sigma_{yy}}{\bar{\sigma}_{yy}}$ in the two porous metal materials.

fractions. The width and height of the simulation cell is $w = 4\,\mu$m and $h = 6\,\mu$m in both cases. Sources are placed at random positions with slip plane orientations $\alpha_1 = 45^\circ$ and $\alpha_2 = -45^\circ$. The source strength is $\sigma_{src} = 0.05\,$GPa. Dislocations that glide towards the boundary of the simulation cell as well as dislocations that are attracted by the free surface are simply pinned. The elastic tensile stresses that build up in the material are large enough to operate most of the dislocation sources. Dislocation generation and motion during loading of the composite tend to relax the overall stresses in the matrix. Figure 3.21 shows the distribution of the tensile stress component σ_{yy} in the materials and the corresponding dislocation microstructure. The stresses are normalized by the macroscopic tensile stress $\bar{\sigma}_{yy}$. Note that the stress concentrations in the metallic interlayer have been significantly relaxed by dislocation motion. The dislocation distributions reveal that dislocations add up to super-dislocations at blocking interfaces with an effective net Burgers vector parallel to the interfaces. The total strain fields are highly non-uniform over the material. This is illustrated very clearly by the deformed boundary meshes shown for both materials in Figure 3.22. The deformation is scaled by a factor of 100 to make it visible. Regardless of the reinforcement morphology, the discrete dislocation results show regions of highly localized deformation that arise as a consequence of localized dislocation activity on one or a few slip systems. After some relaxation time the dislocations are either in equilibrium or immobile. Both initially dislocation free materials are relaxed under a constant loading of $E_{yy} = 0.17\,\%$. The initial macroscopic tensile stress $\bar{\sigma}_{yy}$ is about $0.11\,$GPa for the material with higher pore volume

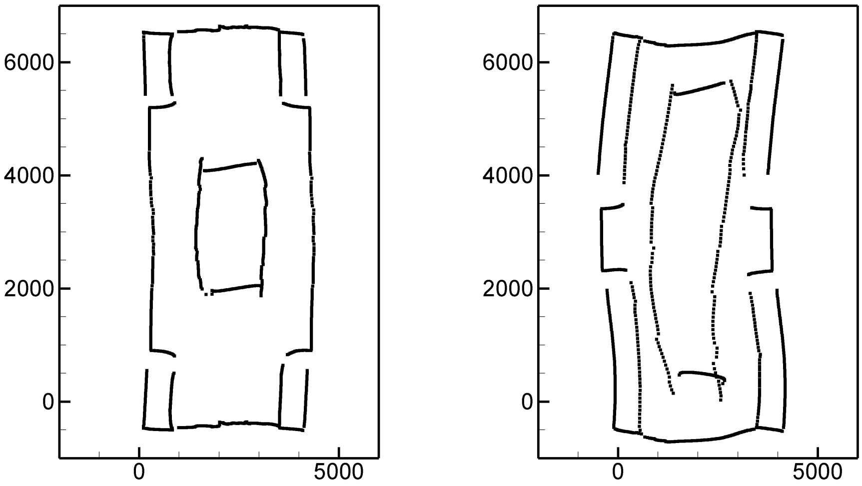

Figure 3.22: The deformed boundaries and interfaces of the RVE. Deformation is scaled up by a factor 100 in order to show the periodic deformation.

fraction and 0.14 GPa for the other material with lower pore volume fraction, see Figure 3.23.

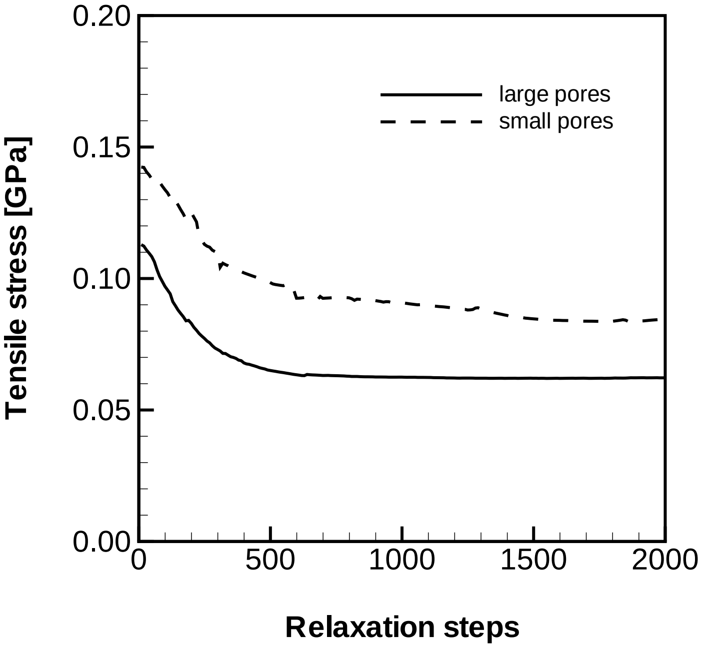

Figure 3.23: Comparison of two porous metal materials. Shown is the macroscopic tensile stress component $\bar{\sigma}_{yy}$ as a function of relaxation steps.

3.3 Discussion of the method

The presented numerical methods are particularly suitable for the implementation of cohesive zones that are used to describe crack nucleation and propagation in elastically inhomogeneous plastic layer materials, as well as interfacial mediated processes during the deformation of dual phase MMCs. The technique has been thoroughly tested for the simple geometry of a single crack on a predefined crack line in a combined DD/CZ model and has been shown to be accurate and numerically stable. In this section a few examples are presented for a crack propagating in a ductile layer. The correlation between the developing dislocation microstructure and the computed macroscopic response of the material as well as the statistical effects of random source distribution on fracture toughness and the influence of the cohesive zone parameters are briefly discussed.

Numerical solution of the dislocation BVP: BEM versus FEM

The combined DD/CZ model for fracture in thin metal layer materials has been formulated by means of a boundary integral method based on distributed virtual dislocations. The governing boundary integral equations are based on Green's function of a single dislocation near a bimaterial interface (Broedling et al., 2006; Gutkin and Romanov, 1991; Mura, 1968; Hills et al., 1996). The numerical procedure follows a collocation scheme.

Compared to FEM based techniques, the Green's function approach has the following computational advantages. First, the solution procedure for the elastic fields includes only physical quantities (separation and traction) on the crack line so that fewer matrix equations need to be solved. The evaluation of stresses in the interior of the continuum can be calculated once the boundary values are determined. Second, the FEM based approaches require discretization of the interior of the continuum, especially in regions of dislocation activity. The evaluation of stress components at the location of an individual dislocation involves two steps at each time increment: identifying the surrounding Gaussian points and extrapolating stresses from the Gaussian points to the dislocation position. With the method used in this work, dislocation numbers on the order of 2000 together with an accurate description of the cohesive zone can easily be handled on a single CPU. On the other hand, there are also drawbacks of the present method.

The applicability of Green's function based approaches relies on whether an appropriate dislocation solution exists for a given problem of interest. Even though a few fundamental dislocation solutions can be found in the literature, the number of possible geometries is still quite limited (Mura, 1968; Hills et al., 1996). For composite materials with elastically dissimilar materials, this method can only be applied for simple geometries. For more complex geometries, e.g. as in the blunted crack model, the effect of elastic inhomogeneity is usually assumed to be small compared with the inhomogeneity associated with plastic deformation so that the assumption of an elastically homogenous, but plastically inhomogeneous material can be used. In conclusion, Green's function based methods are less flexible, but may be more efficient than the DD/FEM models.

Crack growth modeling in dislocation dynamics

There are two strategies that allow modeling crack propagation problems: incremental crack extension methods and a priori definition of the entire crack line. The first method is appropiate for cracks under mixed mode loading embedded in homogenous materials where the path of crack propagation is not known in advance and the direction of crack extension needs to be evaluated based on postulated fracture criteria. The maximum principal stress criterion, for example, is probably the most intuitive one. It assumes that the crack will propagate in the direction perpendicular to the maximum principal stress. In an incremental crack extension analysis, each crack extension increment is modeled with a new virtual dislocation element that introduces new unknowns and extra algebraic equations that need to be solved. Correspondingly the system matrix needs to be updated by generating new rows and columns. Recently, more sophisticated models such as the virtual internal bond (VIB) model were proposed (Klein and Gao, 1998; Ji and Gao, 2004). The VIB model considers cohesive interactions between material particles as an alternative approach to modeling fracture. It differs from cohesive zone models in that, rather than imposing a cohesive law along a prescribed crack line, a network of cohesive bonds is statistically incorporated into the constitutive law of the material via the Cauchy-Born rule, i.e. by equating the strain energy density on the continuum level to the potential energy stored in the cohesive bonds due to an imposed deformation.

In this work, we consider symmetric crack problems propagation along weak interfaces and the crack path is assumed to be known. In this case it is more convenient for the implementation to discretize the whole crack path in advance. We found that for the underlying dislocation boundary value problems, an algorithm based on a fixed systems size is more robust. For the investigation of the influence of the shape parameters of the TS-law, simulations were performed with $\rho_{src} = 120/(\mu m)^2$ for layers of 2000nm thickness with varying shape parameter δ_1 (from 0.05 to 0.45); δ_2 varies correspondingly since the other cohesive zone parameters were kept constant: $\sigma_{th} = 0.8\,\mathrm{GPa}$, $\Delta_c = 2\,\mathrm{nm}$ and $k_{Ic} = 0.37\,\mathrm{MPa}\sqrt{\mathrm{m}}$. The reduction of the initial slope of the TS-law reduces the sharpness of the stress concentration slightly so that the tractions close to the crack tip decrease less rapidly. However, from Figure 3.24 it is clear that the shielding effect is not affected during loading. For clarity, the results of only three different shape parameters are plotted. Figure 3.25 shows the computed fracture toughness and the normalized stress intensity factor at the onset of plasticity for nine different sets of shape parameters. The fluctuation of the values is less than 5% from each other without an identifiable trend.

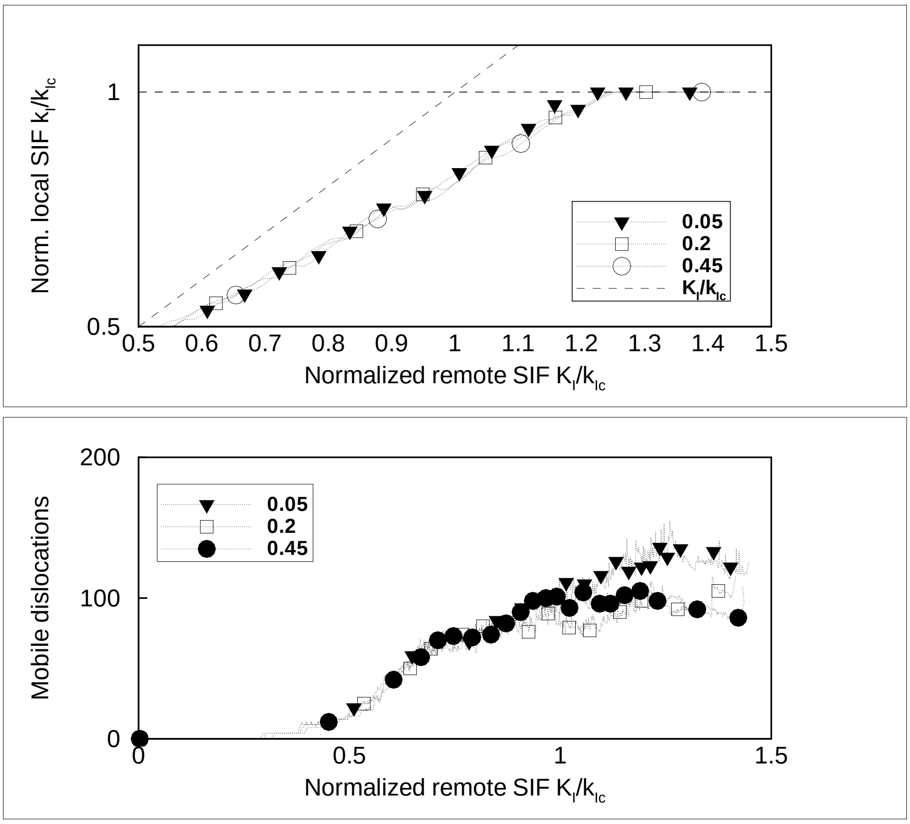

Figure 3.24: Comparison for different shape parameters. The values for the fracture toughness (top) and the number of mobile dislocations (bottom) for three different shape parameters. Symbols are plotted sparsely to identify the curves according to the legend. The data points lie dense along the plotted lines.

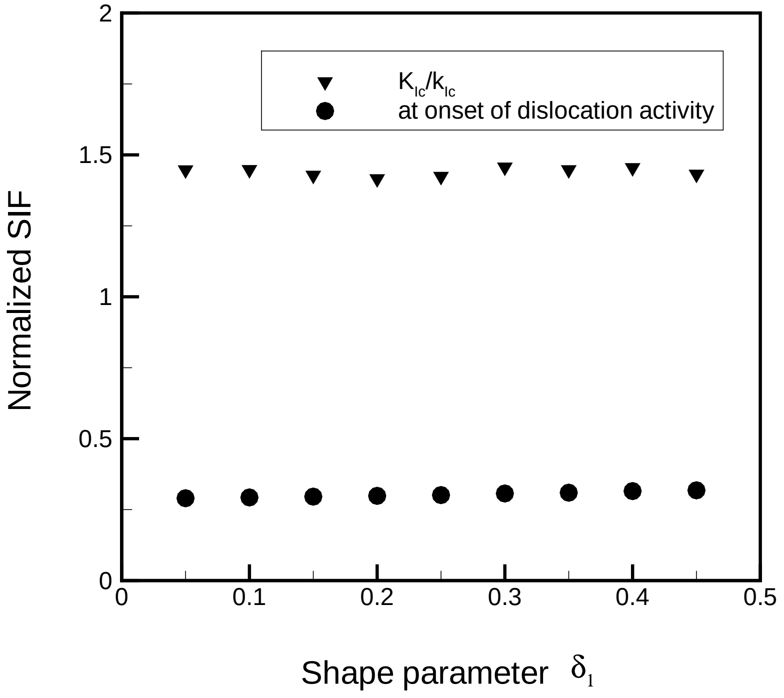

Figure 3.25: Fracture toughness as a function of the shape parameter

Interaction between crack and dislocation microstructure

In the following, three numerical examples for fracture in a plastic layer are given. The setup of the geometry follows Figure 3.7. The material is taken to be elastically homogeneous with shear modulus $G = 26\,\mathrm{GPa}$ and Poisson ratio $\nu = 0.33$. Typical velocities of dislocations near the crack tip are 100 to $200\frac{m}{s}$. In order to resolve the whole spectrum of velocities a comparatively (Cleveringa et al., 2000) small time step of $\Delta t = 2 \cdot 10^{-4}\,\mathrm{ns}$ is chosen. The simulations start at zero applied stress with an initially dislocation free material and the load is increased monotonically with a high constant loading rate $\dot{K}_I = 10^5\,\mathrm{GPa}\frac{\sqrt{m}}{s}$ in order to reduce computational time.

The nucleation and motion of dislocations close to the crack tip causes the driving force for crack extension to change. If the driving force decreases, the dislocation has a shielding character and lowers the local stress intensity factor; otherwise, the dislocation exerts an anti-shielding effect. A change from shielding to anti-shielding is possible since shielding depends on the dislocation position. The two slip planes at inclination angels α_1 and α_2 considered in our model give rise to two types of active slip systems. Taking the anticlockwise direction to be positive, $\alpha_1 = -45^\circ$ is the more active slip system due to the higher resolved shear stress and therefore referred to as the primary slip system. The secondary slip system $\alpha_1 = 45^{\circ}$ is expected to respond harder and needs additional local stress concentrations to be activated. Local stress concentration may arise at pile-ups forming at obstacles or at interfaces. Upon loading there is a local stress intensity factor at which first nucleation occurs on the primary slip system. For a high source density the initially active slip system usually intersects the crack plane behind the crack tip such that the nucleated anti-shielding dislocation migrates towards the free crack surface where it is absorbed and causes crack blunting. The shielding dislocations migrate away from the crack tip. For low source densities, however, it is possible that sources are active with their slip planes intersecting the crack plane at a position ahead of the crack tip. If the source is associated with an α_1-slip plane, an anti-shielding dislocation migrates in the region right in front of the crack tip, such that the crack tip is exposed to the tensile stress field of the dislocation. If this source is continuously active, the resulting dislocation array increases the driving force until it exceeds a critical value and the crack moves to the point where the tip is exposed to the compressive stress of the dislocation array. This sudden drop of the local stress intensity causes the crack to be arrested again. The remote loading can be increased further and the dislocations migrate now into the newly created free surface where they are absorbed and blunt the crack tip. The ultimate remote stress intensity factor, where the material finally fails by cleavage is taken as the materials fracture toughness K_{Ic}. Figure 3.26 shows simulation results for the thicknesses $1\,\mu$m, $2\,\mu$m and $4\,\mu$m of the plastic layer with a source density of $80/\mu\text{m}^2$. The values of the cohesive zone parameters are $\sigma_{th} = 0.8\,\text{GPa}$, $\Delta_c = 2\,\text{nm}$, $\delta_1 = 0.1$, $\delta_2 = 0.2$, leading to an intrinsic fracture toughness of $k_{ic} = 0.37\,\text{MPa}\sqrt{\text{m}}$. On top of Figure 3.26, at an intermediate loading stage $K_I = 0.83k_{ic}$ (a1)-a3)), most of the dislocations have been nucleated on the primary slip system. The loading is subcritical so that the crack tip remains at its initial position. An array of shielding dislocations is positioned ahead of the crack tip. Considering the final stage at failure (b1)- (b3), the crack in (b3) has moved a distance ahead and has been arrested due to the sudden drop of the local stress intensity caused by the shielding dislocation array. The simulations suggest that under multiple active slip systems an unstable crack can be arrested if a sufficient number of shielding dislocations have migrated ahead of the crack tip before first crack advance occurs. The fracture toughness increases with the ductile layer thickness from $K_{Ic} = 1.24k_{ic}$ $(h = 1\mu m)$, over $K_{Ic} = 1.36k_{ic}$ $(h = 2\mu m)$ to $K_{Ic} = 1.56k_{ic}$ $(h = 4\mu m)$.

Statistical effects due to the source distribution

The nucleation of dislocations in the model material is specified by the critical stress for dislocation nucleation and the distribution of the sources in the process domain. For thin layered structures, however, the source distribution degenerates to

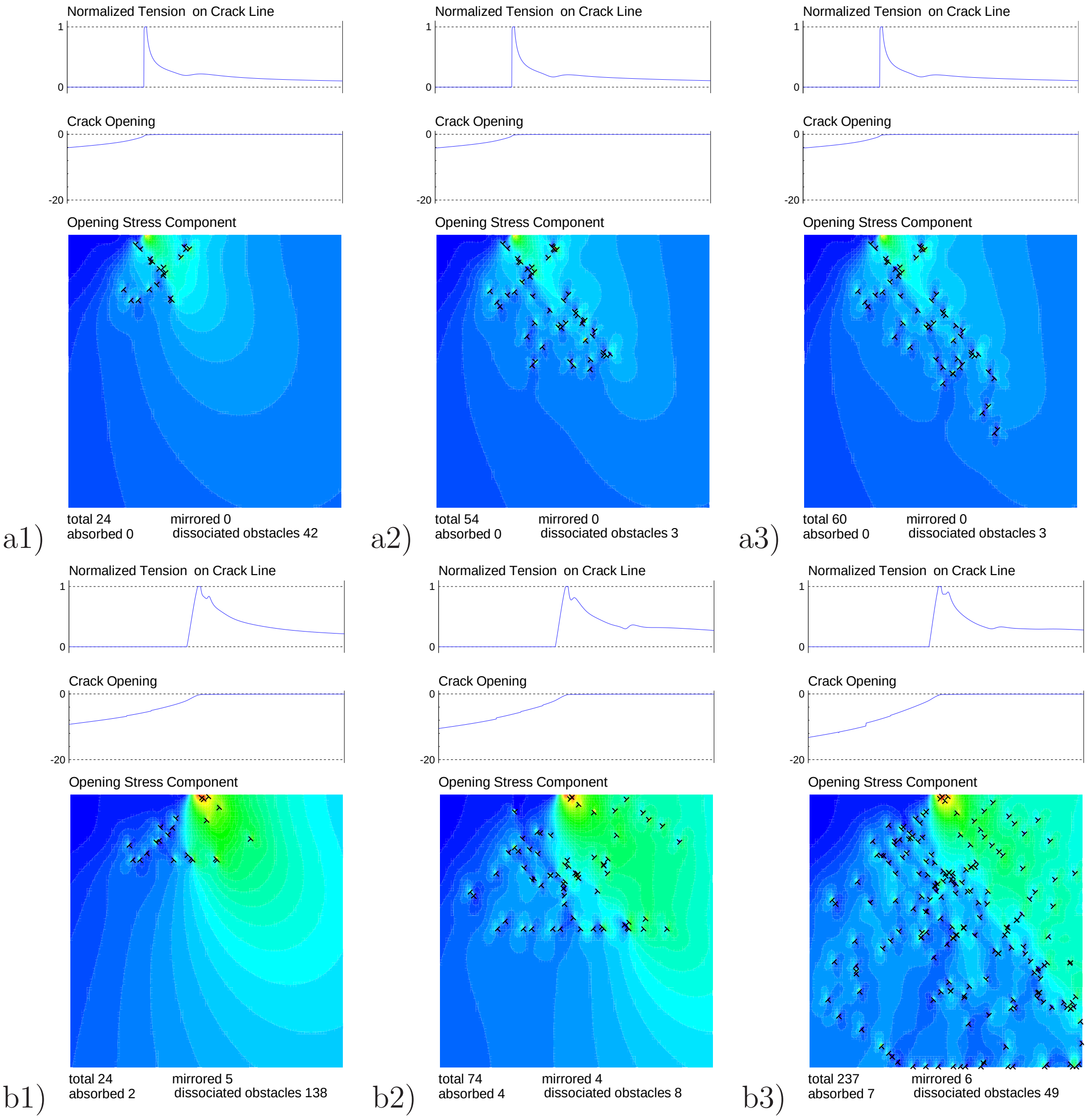

Figure 3.26: The contour plots of the crack opening stress in the simulation box and the evolving dislocation microstructure. Dislocations are marked with the usual symbols. The columns 1-3 are obtained for different $h(1\,\mu\mathrm{m},\ 2\,\mu\mathrm{m},\ 4\,\mu\mathrm{m})$. Below the contour plots the numbers of the total, mirrored and absorbed dislocations are given, as well as the number of disassociated locks. On top, the normal tractions on the crack line are shown, tractions vanish in the part where the crack is fully open. The crack opening is plotted in the middle subplot as indicated. The plots (a1) -(a3) show an intermediate state at $K_I = 0.83\,k_{Ic}$, whereas the stages of final failure are plotted in (b1)-(b3).

a one-dimensional array with only a few sources being active. Below a certain layer thickness a source density is not defined anymore and the results will more or less depend on the positions of the few discrete sources near the crack tip. For the source density in the present simulations, materials with a layer thickness below about 300 nm can be considered to exhibit a brittle response, as the shielding effect of the few involved dislocations is below 5% of the intrinsic fracture toughness. However, for thicker layers it is worth testing how the results would depend on the randomly generated source distribution. In Figure 3.27 and Figure 3.28 the results for two different source distributions are displayed. Simulations were carried out for two different layer thicknesses of 1000 nm and 2000 nm with $\rho_{src} = 80/(\mu\text{m})^2$. The values of the cohesive zone parameters are $\sigma_{th} = 0.8\,\text{GPa}$, $\Delta_c = 2\,\text{nm}$, $\delta_1 = 0.1$, $\delta_2 = 0.2$, with an intrinsic fracture toughness of $k_{Ic} = 0.37\,\text{MPa}\sqrt{\text{m}}$. Figure 3.27 shows the microstructure at the final stage of failure. It is seen that for both thicknesses, the source distribution has an impact on the position of the crack tip when final failure occurs. The distribution 1 provides more sources with primary slip planes in front of the initial crack tip position. Activation of these sources leads to emission of shielding dislocations as the crack advances Figure 3.27. As a result, the fracture toughness is slightly enhanced for both layer thicknesses. For both distributions an obstacle forms almost 1 μm away from the crack tip. This obstacle shuts down some sources on the most active primary slip plane. However, plasticity circumvents this

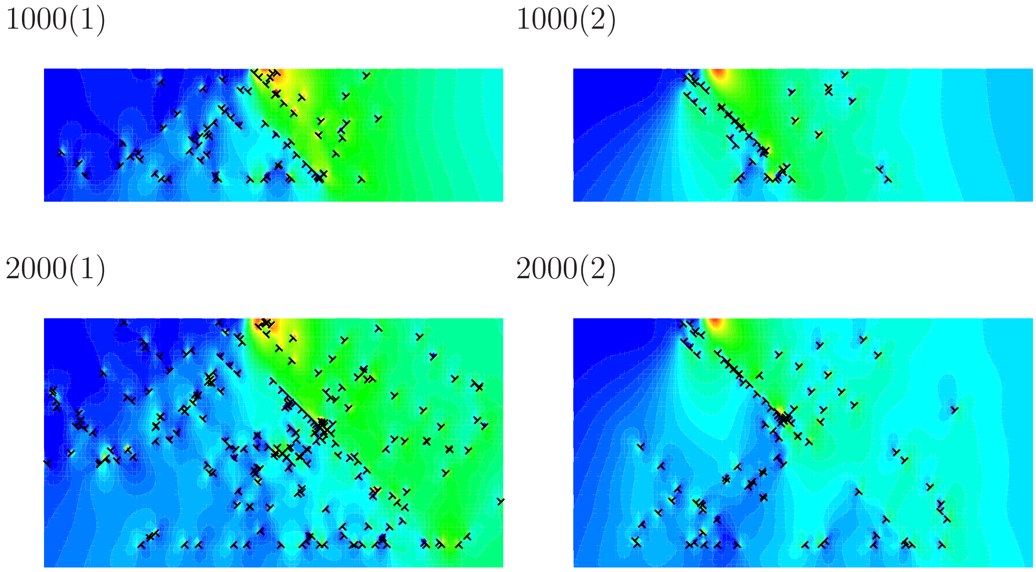
1000(1)
1000(2)
2000(1)
2000(2)

Figure 3.27: Comparison of two different source distributions 1 (left) and 2 (right) for layers of 1000nm (top) and 2000nm (bottom). Shown is the microstructure at critical loading.

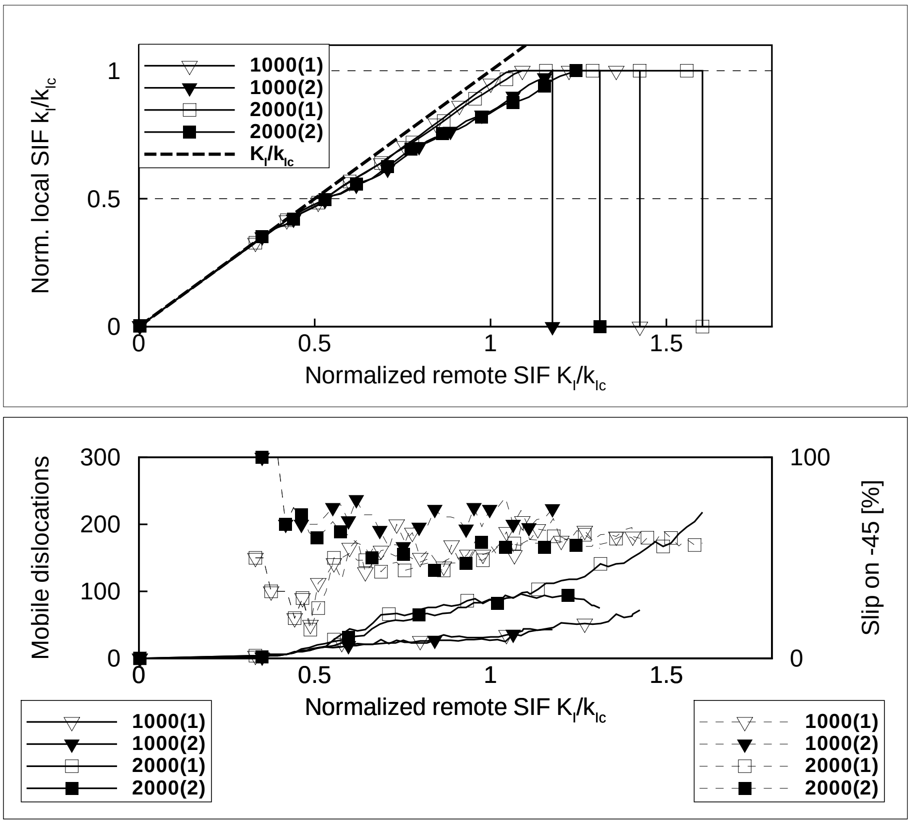

Figure 3.28: Comparison of two different source distributions 1 and 2 for layers of 1000 nm and 2000 nm. On top the local stress intensity factor k_I is plotted versus the remote loading K_I. The symbols on the horizontal axis denote the critical values of K_{Ic} at which failure occurs for the corresponding materials. At the bottom, information about the dislocation activity is displayed. The number of mobile dislocations is assigned to the left axis. The corresponding curves are plotted solid. The dashed curves show the relative contribution of the primary slip system and are assigned to the right axis. Symbols are plotted sparsely to identify the curves according to the legend. The data points lie dense along the plotted lines.

blocked slip plane and dislocation activity jumps over to neighboring slip planes. In Figure 3.28 the shielding effect (top) and dislocation activity (bottom) is displayed. For this model material the increase in fracture toughness due to the development of a plastic zone is about 50 % of the intrinsic fracture toughness. The deviation of k_I from K_I with onset of dislocation activity is clearly seen in Figure 3.28, top. It is also apparent that in the material with distribution 2 (right) first nucleation of dislocations occurs on the primary slip plane, whereas in the other material (left) both slip systems are active at the onset of plasticity (Figure 3.28, bottom). For the total dislocation activity however, both slip systems contribute equally for both layer thicknesses. The influence of dislocation source distribution on the apparent fracture toughness is found to be about 5 to 10 percent. Even though the dislocation microstructure might develop slightly differently, its shielding effect on the crack tip is not changing significantly. The influence is expected to be decreasing with increasing ductility and layer thickness.

Deformation of dual phase MMC

Although the model for reinforced dual phase MMC is highly idealized, it is expected to exhibit characteristic features of plastic flow in dual phase nanocomposite materials with internal interfaces and to demonstrate the scale dependence of material properties such as strength and toughness. The deformation fields in small-scale composites have regions of highly localized deformation. Sliding and separation deformations at the interfaces might occur prior to failure influencing dislocation nucleation and motion processes. Furthermore, the effective plastic flow properties within the matrix depend on the reinforcement morphology, the slip plane orientation as well as on the opening and shear properties of the interface.

The advantage of simulating the deformation of a RVE with periodic boundary conditions is the small system size. However, instead of a finite number of single dislocations, the periodicity of the system introduces an infinite array of dislocations. The price of this approach is the necessary evaluation of periodic image fields. It is possible to consider the effects of PBCs embedding the simulation cell in an infinite and periodic array of image supercells that are exact replica of the primary cell (Cai et al., 2003). Cai et al. (2003) constructed the elastic fields of the dislocations due to PBCs by superimposing the fields produced by the dislocation in the primary simulation cell and image fields of its periodic replica. The superposition is written as a summation of individual contribution from the image cells. The sum is then evaluated semi-analytically with respect to one dimension by choosing a truncation limit. In this work, the image fields are determined by setting up and solving an auxiliary boundary value problem. The computational effort is closely linked to the discretization of the boundary of the simulation cell and does not depend on the number of dislocations that are introduced in the simulation. Note that the necessity of boundary discretization comes from the implementation of the displacement-controlled boundary loading procedure. This procedure is generally required for the tensile deformation simulation of softening materials, see e.g. (Lin et al., 2006).

The evaluation of the materials stress-strain response can be carried out in an incremental manner. For a quasi-static simulation under monotonic loading an incremental loading step is followed by a relaxation phase as presented in section 3.2.3. During this relaxation phase the dislocation microstructure reaches an relaxed state where the macroscopic stress levels off, see Figure 3.23. In the case of dynamic simulations where complete relaxation is not allowed, the extent of relaxation depends on the rate of change of the dislocation microstructure that is defined by the mobility law in comparison with the applied loading rate.

In this work the model for dual phase MMC is applied to the extreme case of non interacting interfaces to demonstrate the possibilities and limitations of the present model. In the case of reinforced MMC with strong interfaces, the stresses are rather high within the reinforcement due to the occurrence of superdislocations at the interfaces. The stress contribution from the plastic flow leaves the reinforcement in residual tension and the matrix in compression. Dislocation nucleation in this model occurs first at the corners of the rectangular reinforcements where stress concentrations are high. Since the elastic properties of matrix and reinforcements are equal tensile stresses will only build up in the reinforcements after the generation of a sufficient amount of plastic flow in the matrix. At later stages of deformation, dislocation nucleation is expected also to occur in the vicinity of the entire front-ends of the reinforcements.

4 Cleavage fracture of metal layers

The fracture toughness of a layered composite material is analyzed employing the combined two-dimensional DD/CZ model presented in section 3.2.1. The fracture mechanism of an elastic-plastic (ductile) material sandwiched within purely elastic layers approaches ideally brittle behaviour with decreasing layer thickness. We investigate the influence of different constitutive parameters concerning dislocation plasticity as well as the effect of cohesive strength of the ductile material on the scaling of fracture toughness with layer thickness.

4.1 Motivation and problem statement

The fracture toughness of the layered composite material is known to be strongly correlated with the layer thickness and is directly influenced by the cohesive strength of the ductile layer (Hsia et al., 1994; Broedling et al., 2006). The analytical super-dislocation model by Hsia et al. (1994) predicts a gradual scaling behavior with a smooth increase in fracture toughness as a function of layer thickness. However, it is known that under strong confinement individual secondary plastic flow processes have a great impact on the materials behavior. The distribution of the shielding dislocations may be critical for the scaling behavior of the fracture toughness. To clarify the remaining question whether there is a critical length scale that is characteristic for the scaling behavior, extensive parameter studies were conducted to deduce the scale dependent fracture toughness as a function of the layer thickness. Special focus is directed towards the effect of microstructural surroundings near the crack tip as well as the influence of the intrinsic material properties on the scaling behavior.

Cleavage failure of dual phase layered nanocomposites is simulated accounting for the collective dislocation behaviour near a moving crack tip. The crack tip is embedded in a metal layer sandwiched between two brittle solids. Special attention is paid to the restrictions that a layer geometry imposes on the expansion of the plastic zone and to the resulting fracture toughness of the composite structure. For the analysis of the fracture toughness of the layered composite material the combined discrete dislocation and cohesive zone model for the simulation of fracture in thin metal films is employed (section 3.2.1). The combined DD/CZ model links a two-dimensional dislocation dynamics (DD) description of plasticity and a cohesive zone (CZ) description of fracture. The cohesive crack tip is treated as part of a much larger finite crack confined in the ductile layer. The underlying boundary value problem is formulated with a set of boundary integral equations and numerically evaluated with a collocation method. A detailed description of the elastic boundary value problem and the constitutive rules associated with the model is given in sections 3.2.1 and 3.1.2, respectively.

4.2 Simulation results for the scaling behavior

The results obtained are presented and discussed in two parts. First, the influence of the source distribution on the toughness-thickness dependence is shown. Second, the correlation of the toughness-thickness dependence with cohesive strength and source strength indicated by the results will be pointed out. The setup of the geometry follows Figure 3.2.1. The simulations start at zero applied stress with an initially dislocation free material and the load is increased monotonically with a constant loading rate of $\dot{K}_I = 10^3\,\mathrm{GPa}\frac{\sqrt{\mathrm{nm}}}{\mathrm{ns}}$. The material is taken to be elastically homogeneous with shear modulus $G = 26\,\mathrm{GPa}$ and Poisson ratio $\nu = 0.33$.

4.2.1 Influence of the microstructural surrounding

In this section the influence of the local source distribution as well as that of the source density within the bulk material are investigated. For fracture of thin layers the availability of sources close to the crack tip rather than the overall source density becomes important. In Figure 4.1 simulation results for four $1\,\mu\mathrm{m}$ thick layer materials A, B, C and D with different source distributions are plotted. Figure 4.1 a) and Figure 4.1 b) show clearly the effect of dislocation emission right at the crack tip. The source density of the bulk material in both simulations has been chosen to be $80\,(\mu\mathrm{m})^{-2}$ with an overall identical distribution, but in one case (shown in Figure 4.1 b)) a source with a slip plane angle of -45° has been placed at position $(x, y) = (40\,\mathrm{nm}, -50\,\mathrm{nm})$. Note, that the serrated shape of the local stress intensity factor in Figure 4.1 b) is a result of the strong dislocation-interface interaction and reflects single nucleation events of the near crack tip source. The consequence of the existence of a crack tip source is that the number of nucleated dislocations has been doubled. The formation of a compact dislocation pile-up of 20 dislocations exerts a strong shielding effect and causes an increase in fracture toughness of about 20%. The results for a higher bulk source density of $120\,(\mu\mathrm{m})^{-2}$ are shown in Figure 4.1 c) and for only one crack tip source in figure Figure 4.1 d). The resulting fracture toughnesses for the different source distributions are shown in Figure 4.2 as a function of film thickness. It is seen that for thicknesses below 1000 nm the crack tip source is dominant, because the curves for the materials with the crack tip source (B, C and D) do not deviate from each other in this regime. Above this thickness the fracture toughness of the material D with only on source close to the crack tip remains approximately constant. The curves of materials B and C start to

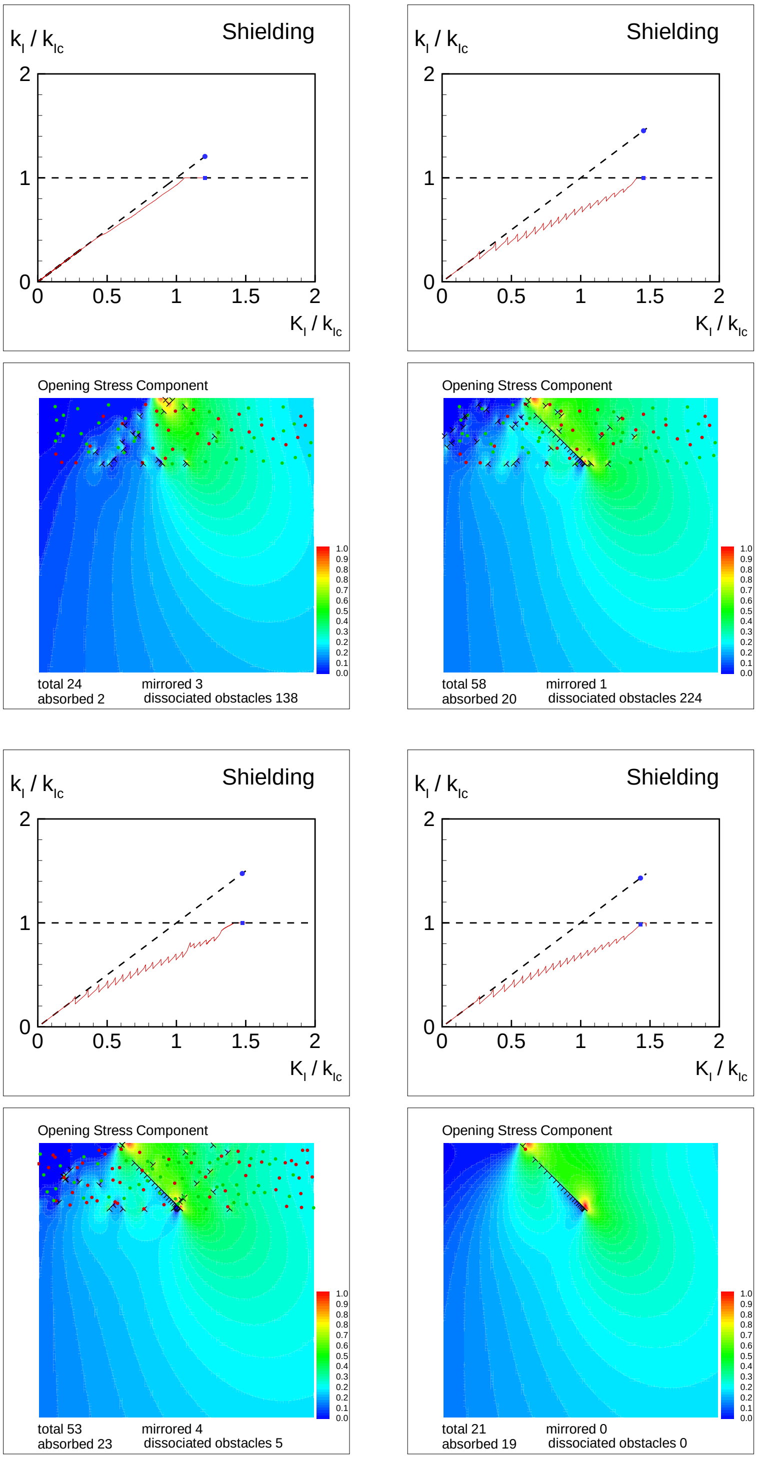

Figure 4.1: Comparison of four different source distributions for a $1\mu m$ thick layer. Shown is shielding and final microstructure for each distribution: a) $80(\mu m)^{-2}$ without crack tip source, b) $80(\mu m)^2$ with crack tip source, c) $120(\mu m)^{-2}$ with crack tip source, d) only a single crack tip source.

deviate from each other at a thickness of 2000 nm. Interestingly the material with the higher source density gives the lower fracture toughness, which is explained by the higher dislocation density in this case, hindering the free expansion of the shielding dislocations emanating from the near crack source. Thus, the material with a higher source density exhibits a more pronounced work hardening. The comparison of material A and B shows that the bulk fracture toughness of a material with a bulk source density of 80 $(\mu\mathrm{m})^{-2}$ increases by about 15% when additionally a crack tip source is considered. The influence of the bulk sources on the fracture toughness of a layered mate-rial is noticeable only above a thickness of 1000 nm. The bulk toughness of a material with a crack tip source increases by about 20% (10%) when in addition to the crack tip source a distribution of bulk sources with a density of 80 $(\mu\mathrm{m})^{-2}$(120 $(\mu\mathrm{m})^{-2}$) is considered.

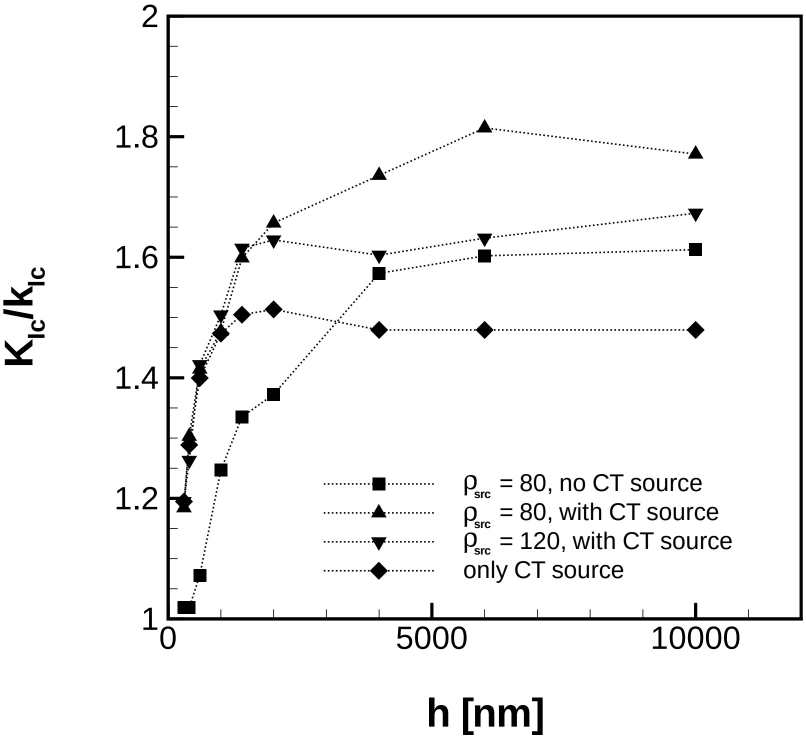

Figure 4.2: Normalized fracture toughness as a function of layer thickness for four different source distributions, see also Figure 4.1.

4.2.2 Influence of intrinsic material properties

We have conducted extensive parameter studies to investigate the effect of cohesive strength, intrinsic fracture toughness as well as source strength on the resulting fracture toughness. Figure 4.3 shows toughness-thickness curves for different sets of parameters for a layer material with $\rho_{src} = 80\,(\mu\mathrm{m})^{-2}$ with crack tip source. Figure 4.3 a)-d) reveal the effect of cohesive strength and intrinsic fracture toughness.

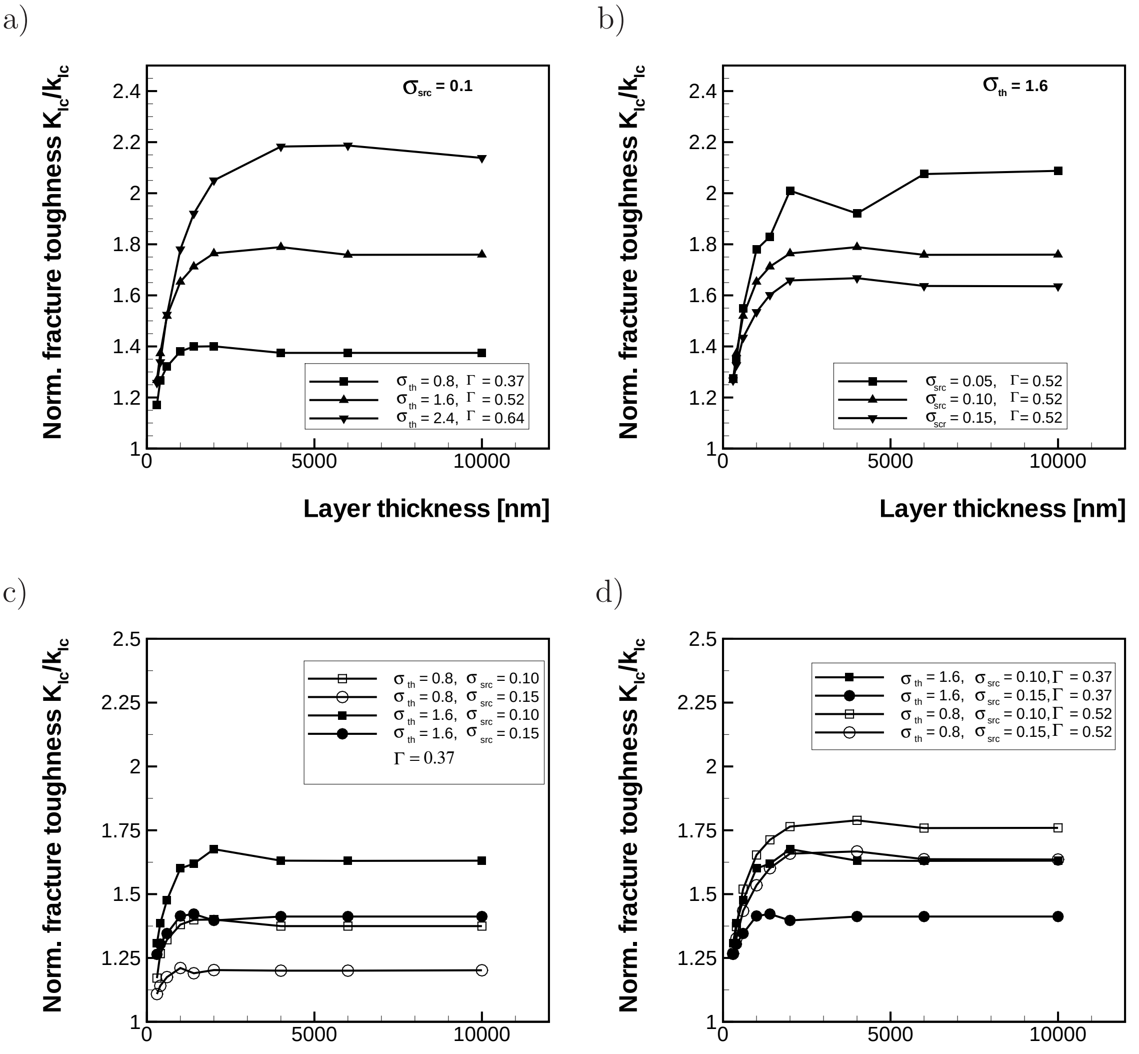

Figure 4.3: Toughness-thickness dependencies for a layer material with $\rho_{src} = 120\,(\mu\mathrm{m})^{-2}$. The stresses are given in units of $1\,GPa$, intrinsic fracture toughnesses in $MPa\sqrt{m}$. a) Three different sets of cohesive parameters and a constant source strength of 0.1 GPa. b) Influence of source strength for a constant cohesive strength of 1.6 GPa. c) Influence of cohesive strength for two different source strengths of 0.1 GPa and 0.15 GPa. d) Influence of cohesive energy for two sets of source and cohesive strengths.

Both parameters enhance the macroscopic fracture toughness significantly. Figure 4.3 c) shows simulation results for two different intrinsic fracture toughnesses for two different source strengths σ_{src}. A 40% increase of the intrinsic fracture toughness enhances the bulk toughness by about 10%. We define the critical layer thickness to be that thickness where the fracture toughness of the layer material reaches 95% of the material's bulk toughness. The bulk toughness as well as the critical layer thickness is increasing with the cohesive strength. A 100% increase of the cohesive strength enhances the bulk toughness about 10% and the critical layer thickness about 20%. More significant is the influence of the source strength, corresponding to the initial yield strength of the material. When dislocation nucleation is harder (100% higher yield strength), the bulk fracture toughness drops about 20% and the critical layer thickness decreases about 80%.

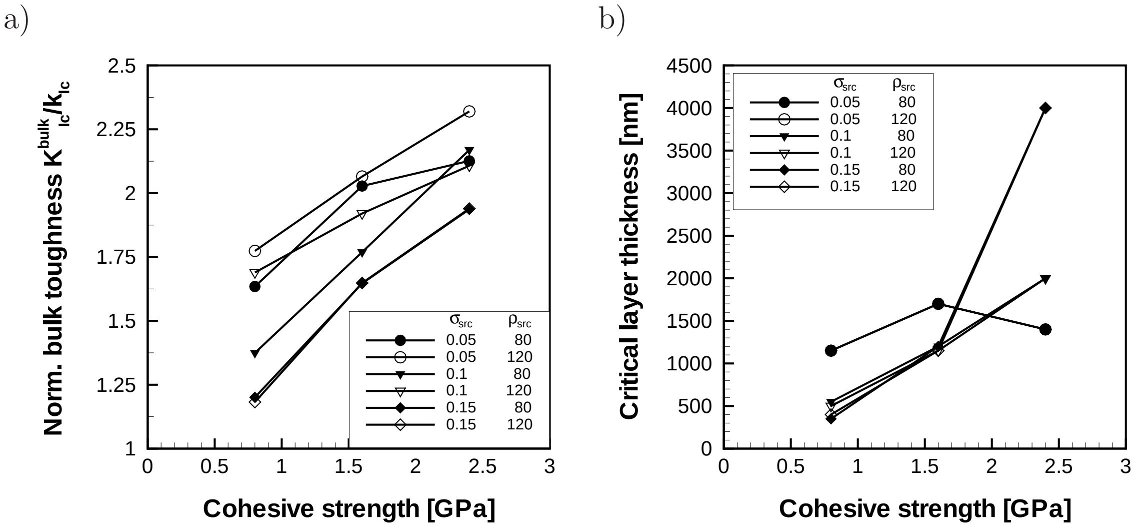

Figure 4.4: Bulk fracture toughness (a) and critical layer thickness (b) as a function of cohesive strength for different source strengths. Curves correspond to two source densities of $\rho_{src} = 80\,(\mu\mathrm{m})^{-2}$ (filled symbols), $\rho_{src} = 120\,(\mu\mathrm{m})^{-2}$ (open symbols), and three different source strengths $\sigma_{src} = 0.05\,\mathrm{GPa}$, $0.1\,\mathrm{GPa}$, $0.15\,\mathrm{GPa}$

4.3 Discussion

4.3.1 Fracture behavior under confinement

The semi-brittle bulk materials considered here show a rather low fracture toughness determined by the competition of loading rate and expansion rate of the plastic zone. Due to this rate effect the layer materials reach their bulk fracture toughness at a layer thickness of a few micrometers at the high loading rate applied. The results of the numerical model are consistent with the expectation that fracture toughness decreases with increasing yield stress, but increases with the cohesive strength for a material with a constant layer thickness. The scaling behaviour of the fracture toughness with layer thickness depends on these material parameters, but also on the microstructure in the vicinity of the crack tip. Strain localization due to easy dislocation generation right at the crack tip improves toughness in thin layers and leads to a jump-like increase of fracture toughness with layer thickness. However, the fracture toughness after the transition towards bulk behaviour proves to be higher when the distribution of dislocation is more homogeneous, because in this case the crack grows in a stable fashion over some distance. In this model the dislocations nucleating close to the crack tip and piling up against the interface to the elastic region do not cause decohesion at the ductile/elastic interface, nor cracking of the brittle layer. Figure 4.5 shows that the stress at the dislocation pile-up stays below the theoretical strength of the cohesive zone model even for the smallest layer thicknesses. The results show that crack initiation at the ductile/elastic interface is only expected if the interface strength is less than 50% of the bulk cohesive strength. For numerical purposes dislocations pile up at a minimum distance of 40b to the interface, see Figure 3.1. In the following we analyze the importance of dislocation nucleation right at the crack tip for the overall fracture toughness of the layer materials. Various simulations have been performed with the present DD model suggesting that for thick layers a propagating crack temporarily arrests when it comes close to a source. This is caused by the sudden increase in the local stress at the source due to the approaching crack tip, which causes the source to emit a number of dislocations within a short period of time. These dislocations suddenly exert a strong shielding effect on the crack tip, thus causing its arrest. This mechanism has also been described by Cleveringa et al. (2000), where crack growth in a bulk material was studied. However, we observe that for thin layers the back stress from dislocation pile up at the ductile-elastic interface not only

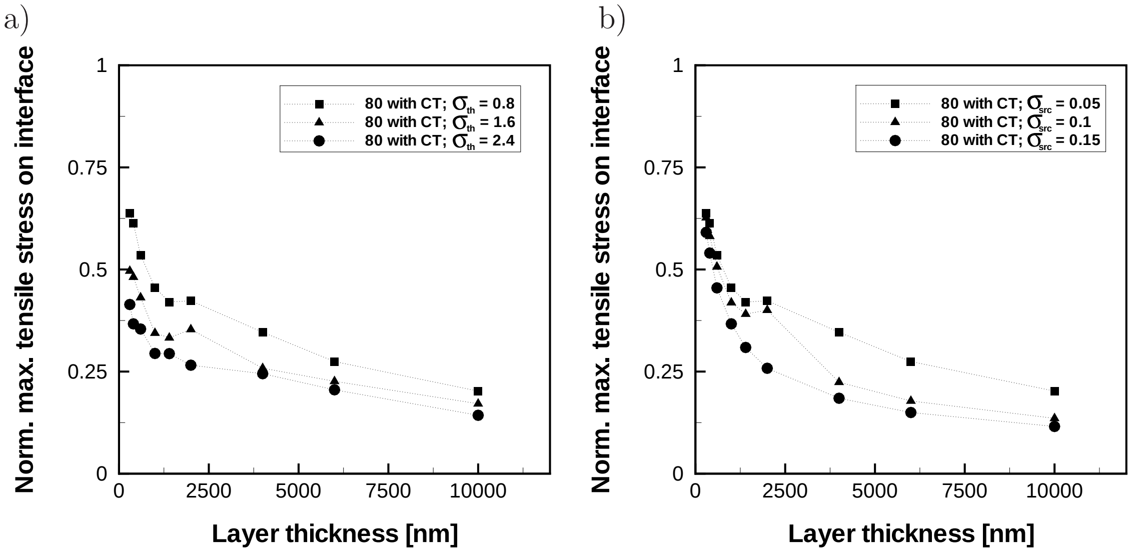

Figure 4.5: Maximum tensile stresses at the ductile/elastic interface as a function of layer thickness for a source distribution $\rho_{src} = 80\,(\mu\mathrm{m})^{-2}$ with a crack tip source. The stresses are normalized with respect to the theoretical strength employed in the cohesive zone model. Curves are plotted for different cohesive stresses a) and for different source strengths b).

inhibits further dislocation generation at the source, but also increases the local stress intensity factor in front of the crack tip. Therefore, crack arrest seems to be more difficult in thin layers.

The crack tip source implemented in this model in order to enable dislocation activity right at the crack tip nucleates complete dislocation dipoles, representing dislocation loops in three dimensions. However, the anti shielding dislocations emitted from this source are absorbed from the free crack surface right after each nucleation event and hence the results are identical to the monopole source model used in other work (Roberts et al., 1994; Hartmaier and Gumbsch, 2005). The strongest effect of enabling dislocation nucleation right at the crack is that the materials fracture toughness increases more rapidly with the layer thickness. At a thickness of about 300 nm the materials fracture toughness can already reach 120% of the intrinsic fracture toughness, whereas a material without crack tip source still exhibits an almost brittle response.

4.3.2 Shielding dislocations under confinement

The analytical “superdislocation“ model in (Hsia et al., 1994) considers the total dislocation density and hence the origin of the shielding factor to be concentrated at a point where the slip plane that is associated with the crack tip intersects the ductile/elastic interface. The super dislocation model underestimates the shielding effect of a compact dislocation pile-up right at the crack tip that we found to be the reason for a jump like increase of fracture toughness with the layer thickness. Furthermore, in our multi source model the back stress originating from dislocation pile-ups at the interface triggers source operation close to the interface and thus remote to the crack tip. If the source generates dislocations on a slip plane parallel to that of the piled-up dislocations, the newly created dislocations move back to the crack tip and increase the local stress at the source that generated the piled-up dislocations. Thus the secondary dislocations reduce the back stress of the pile-up and enable further generation of shielding dislocations. The activation of the second slip system produces dislocations that travel in front of the crack tip and exert a strong shielding effect once the crack starts to advance. In both cases, dislocation nucleation at the interface enhances the toughness either by reactivating crack tip sources or by direct shielding of the advancing crack.

Hence the present numerical model predicts a rapid transition at smaller layer thicknesses whereas the analytical super dislocation model predicts a rather gradual toughness-thickness dependence. Moreover, the super dislocation model does not account for rate effects due to the competition between loading rate and expansion rate of the plastic zone and does not indicate saturation of fracture toughness at large layer thicknesses. Figure 4.6 a) shows that in the multiple source model the number of total dislocations that participate in the system increases strongly with increasing thickness. However, not all of the nucleated dislocations contribute equally to the overall shielding factor, in fact some dislocations do not contribute at all, as can be seen by comparing the large differences in the total number of dislocations plotted in Figure 4.6 a) to the relatively small difference in the fracture toughness of the different source distributions. The comparison reveals that the crack tip source provides the most efficient shielding and thus the best ratio of fracture toughness versus number of dislocations. In Figure 4.6 b) it is shown that the number of blunting dislocations gives a much better correspondence to the fracture toughness than the total number of dislocations. This number of blunting dislocations is also related to the magnitude of the net Burgers vector within the plastic zone and hence to the density of geometrically necessary dislocations. In all cases where dislocation generation at the crack tip is considered, the shielding is mainly caused by the dislocations emanating from that source. If dislocation nucleation directly at the

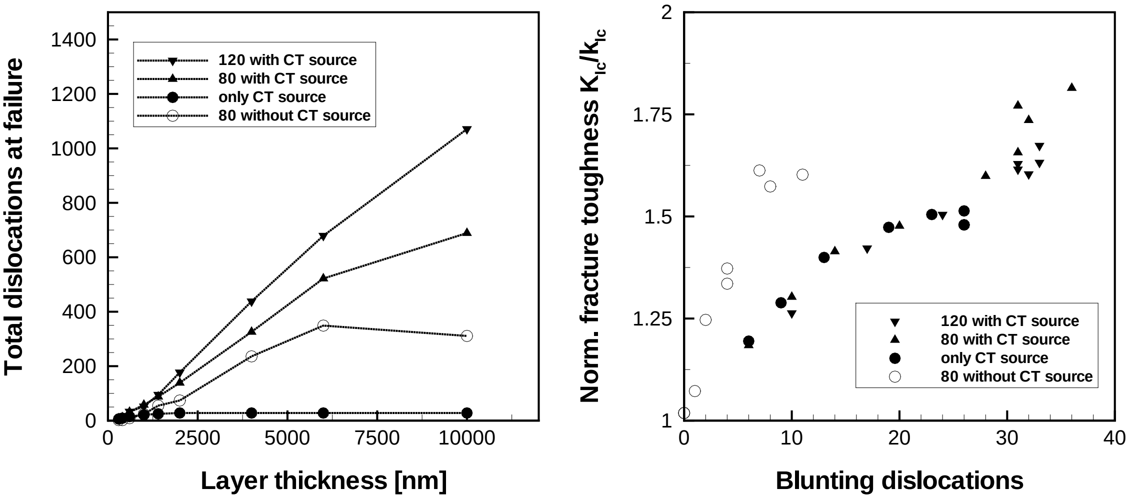

Figure 4.6: Comparison of four different source distributions (see text): a) Number of dislocations present at failure as a function of layer thickness. b) Normalized fracture toughness as a function of blunting dislocations (right). The values in the legends are the densities of the bulk source distribution per $(\mu m)^2$.

crack tip is not enabled, the net Burgers vector at failure is lower, which means that the shielding has to be produced by non-blunting dislocations. Our results show that fracture toughness in the regime below the critical layer thickness is strongly dependent on the availability and activity of dislocation sources right at the crack tip. Consequently it can be argued that since a propagating crack tip can be stopped when it comes close to a dislocation source this configuration, which yields the maximum fracture toughness, dominates the fracture process in layered structures.

5 The strength limit in a bio-inspired metallic nanocomposite

Large-scale molecular dynamics simulations are performed to investigate the plastic deformation behavior of a bioinspired metallic nanocomposite which consists of hard nanosized Ni platelets embedded in a soft Al matrix. The investigation is restricted to an idealized nanocomposite structure with regular platelet distributions in a quasi-twodimensional geometry under quasi-static loading conditions. This restriction enables us to study size dependent material properties over a wide range of length scales with a fully atomistic resolution of the material and thus without any a priori assumptions of the deformation processes. The simulation results are analyzed with respect to the prevailing deformation mechanisms and their influence on the mechanical properties of the nanocomposite with various geometrical variations. It is found that interfacial sliding contributes significantly to the plastic deformation despite a strong bonding across the interface. Critical for the strength of the nanocomposite is the geometric confinement of dislocation processes in the plastic phase, which strongly depends on the length scale and the morphology of the nanostructure. However, for the smallest structural scales, the softening caused by interfacial sliding prevails, giving rise to a maximum strength.

5.1 Motivation and problem statement

The focus on bio-inspired metallic nanocomposites is motivated by the current research initiatives in the area of interface engineering and biomimetic design. A number of experimental studies on the deformation behavior of nanocrystals with average grain size less than 100 nm show generally an Hall-Petch behavior, i.e. an increasing yield stress and hardness with decreasing grain sizes down to 20 nm (Kauffmann et al., 2005; Wang et al., 2002; Yip, 1998; Arzt, 1998; Chen et al., 2006). However, the inverse Hall-Petch effect that has been reported for grain sizes below 10 nm regards the decrease in strength with further grain refinement, see e.g. (Volpp et al., 1997). It is assumed that in this regime deformation is mainly accommodated by grain boundary sliding (M.A. Meyers, 2006; Weertman, 2000; Koch, 2002). In spite of significant progress, understanding of the deformation mechanisms of nanostructured materials at ultrafine scales is still lacking although it is of great scientific interest. Knowledge of the governing deformation mode would enable material designers to suppress the fall-off in strength at ultra fine scale and develop novel super hard and tough materials.

Part of the motivation for this work also comes from the increasing evidence that the superior strength and toughness of biological materials including nacre, bone and tendon may be attributed to a generic parallel staggered arrangement of their microstructure (Landis, 1995; Menig et al., 2000; Gao et al., 2003). Ji et al. (2004) showed that the large aspect ratio and the nanometer size of inclusions in the biomorphous MMC lead to significantly improved properties with increased tolerance of interfacial damage. For example, it was found that partially debonded inclusions continue to carry mechanical load transferred via longitudinal shearing of the matrix material between neighboring inclusions. The larger the inclusion aspect ratio, the larger is the flow stress and work hardening rate for the composite. Increasing the volume concentration of inclusion also makes the biomorphous MMC more tolerant of interfacial damage.

The atomistic model for a dual phase (hard/soft) metallic nanocomposite is set up as follows. The prevailing deformation mechanisms are investigated under tensile loading for different length scales and morphologies. In particular we are quantifying the contributions of conventional dislocation based plasticity and mechanical twinning on the one side and interfacial shearing on the other side which enables us to identify the critical length scale at which the dominant mechanisms change roles. We furthermore study the influence of interfacial damage nucleation and evolution on the materials strength as a function of structural scaling. Large-scale molecular dynamics simulations are performed to investigate the plastic deformation behavior of a bio-inspired metallic nanocomposite which consists of hard nanosized Ni platelets embedded in a soft Al matrix. The investigation is restricted to an idealized nanocomposite structure with regular platelet distributions in a quasi-two-dimensional geometry under quasi-static loading conditions. This restriction enables us to study size dependent material properties over a wide range of length scales with a fully atomistic resolution of the material and thus without any a priori assumptions of the deformation processes. The simulation results are analyzed with respect to the prevailing deformation mechanisms and their influence on the mechanical properties of the nanocomposite with various geometrical variations.

5.2 Model and analysis techniques

As a model system for our investigations of strength and ductility resulting from different deformation mechanisms in a metallic nanocomposite we consider a dual phase system consisting of hard nanosized nickel platelets embedded in a soft aluminum matrix with a nanostructural morphology similar to that of bone, see Figure 5.1. The specific system chosen consists of Ni platelets embedded in an Al matrix because reliable descriptions of the atomic interaction for these atom species are described in the literature (Ludwig and Gumbsch, 1995).

The platelets have a high aspect ratio and are in staggered alignment. Under tensile loading in direction of the platelets this structure is expected to show high stiffness and strength, but also enhanced toughness since large amounts of energy can be absorbed by successive decohesion at the ends of the platelets, as well as by plastic shearing of the metallic interlayer and finally interfacial shearing after saturation of dislocation activity. The question is how such a microstructure design is correlated with its mechanical properties.

We study plastic deformation of such structures under quasi-static loading conditions with classical molecular dynamics simulations and compute the macroscopic stiffness and strength of the material under geometrical variation of the nanostructure. The investigation is restricted to nanocomposites containing platelets with an infinite extension in the out of plane direction in Figure 5.2. This allows us to study systems with small unit cells and periodic boundary conditions in this direction in a quasi two-dimensional analysis. It is noted here that the computation is fully three-dimensional with the correct crystal structures for both constituents. However, the smallness of the numerical samples in the out-of-plane direction allows us to investigate size dependent material properties over a wide range of length scales and to conduct extensive studies on the governing deformation mechanisms and on their influence on the mechanical properties of the nanocomposite structure.

For the deformation analysis of the nanocomposite a periodic unit cell of the mate-

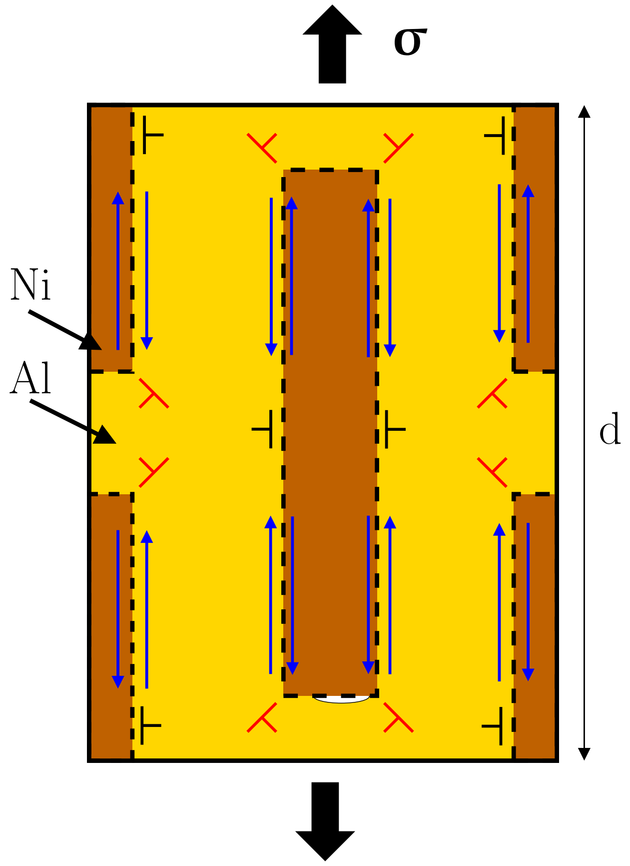

Figure 5.1: Schematic of the nanocomposite material considered: Hard Ni platelets are embedded in a soft Al matrix in a staggered alignment. High stress concentrations at the fronts of the platelets due to elastic mismatch of the two phases lead to interfacial debonding under dislocation nucleation (red symbols). The black symbols denote the effective distribution of glide dislocations that gives rise to plastic shear deformation. Interfacial shearing when pullout sets in after debonding is marked with blue arrows. The platelets are mainly under tensile load, while the matrix is heavily sheared.

rials building block is considered, as depicted in Figure 5.2. The lattice constants of Al and Ni are $a_{Al} = 4.049\,\text{Å}$ and $a_{Ni} = 3.524\,\text{Å}$ according to the potential adopted in this study. We restrict our analysis to laminated nanocomposites with discontinuous platelet reinforcements in the x-y plane that are infinitely extended in the z direction. Total deformation is therefore governed by a state of plane strain in planes with normal vectors pointing in the z-direction. The simulated $[\bar{1}10]$ textured columnar nanostructures consist of two phases Ni and Al with the same crystallographic orientation. The orientation and the periodic boundary conditions cause the nucleation of dislocations with mixed edge and screw character with Burgers vectors $\boldsymbol{b}_1 = [112]$ and $\boldsymbol{b}_2 = [11\bar{2}]$ on two $\{111\}$ slip planes. This implies that the number of possible slip planes that can accommodate the plastic deformation is limited to

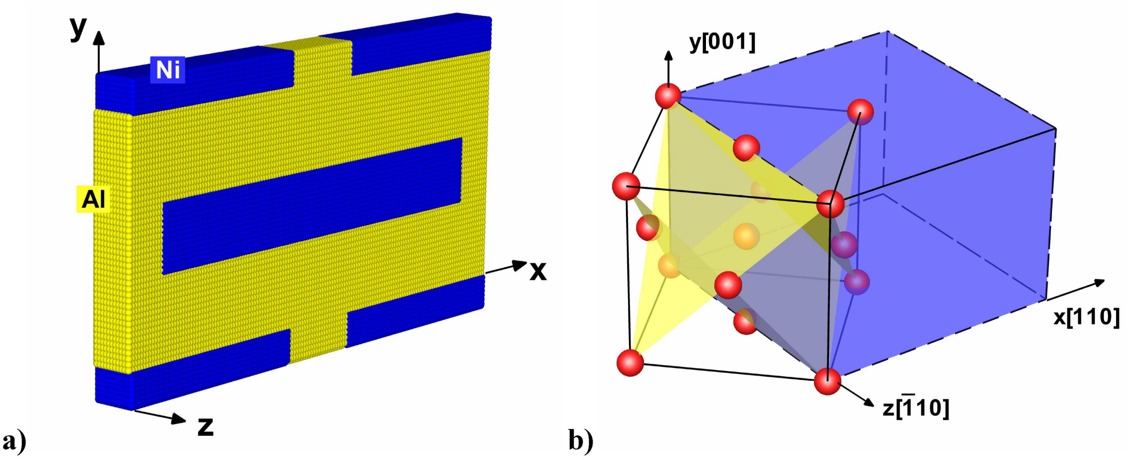

Figure 5.2: a) Sample geometry of the building block of size d. Ni atoms are colored blue and Al atoms yellow. b) Orientation of the building block (blue cuboid) in the crystallographic coordinate system. The yellow planes indicate the {111} slip planes.

two. Due to this geometrical constraint we expect the material to respond harder than laminated nanocomposites with discontinuous reinforcements in all directions. However, the benefit of the reduction in dimension is a lower system size that allows performing simulations under realistic quasi static loading conditions. Dynamical effects stemming from a high loading rates usually applied in MD simulations are thus avoided. Moreover, the temperature considered is $T = 0\,\mathrm{K}$.

The initial atomic configurations for the simulations are generated as follows. Two auxiliary periodic structures of Al and Ni single crystals are created with building block size close to that in the desired composite structure. Single platelets are then cut out from the Ni single crystal and shifted to the final position within the composite for which the periodic box of the initial Al single crystal is taken. Finally both auxiliary samples are merged and Al atoms that are closer to the Ni atoms than the Al-Al nearest neighbor distance are eliminated. The chosen crystal orientation and the building block geometry are shown in Figure 5.2. The mechanical properties of the metallic nanocomposite are computed with the parallel classical molecular-dynamics code 'IMD' from the Institute of Theoretical and Applied Physics, University of Stuttgart (Stadler et al., 1997). The analysis of scale dependency requires comparability of the deformation mode over the entire scaling regime. It is therefore critical for the analysis to subject all structures to a well defined loading state. Smaller modifications have been made to the code to perform uniaxial tensile loading simulations under realistic quasi-static conditions. This work covers only equilibrium atomistic simulations. That means that the system is completely isolated from its surroundings with a fixed number of atoms, volume and constant total energy. These boundary conditions correspond to the microcanonical (NVE) ensemble in statistical mechanics. A multi-body potential based on the embedded atoms method (EAM) is adopted in the simulation. The potential energy includes pair interactions between nuclei of atoms i and j and the embedding energy as a function of the local electron density around atom i, see chapter 2. The embedding energy is assumed to depend solely on the local electron density provided by the surrounding atoms. The full description of the Ni-Al system requires definition of seven potential functions. The functions are obtained by fitting to the properties of the individual Ni and Al elements, respectively, to the properties of the Ni-Al alloys in case of the cross-interaction functions (Ludwig and Gumbsch, 1995). The potential used for the Ni-Al system also gives a good representation of the interatomic forces across interfaces between Ni and Al.

After sample generation the structure of the building block Figure 5.2a) is equilibrated with respect to local interatomic forces and global axial stresses at 0 K with periodic boundary conditions applied in all directions. For the relaxation of global axial stresses a linear transformation is computed based on an initial guess for the effective bulk modulus of the composite. This transformation is applied on the simulation box and content so that the box size and shape change accordingly. The box size in z direction is about which is greater than twice the cut-off radius of the interatomic potentials. Due to the 13 % lattice mismatch between Ni and Al, a semi-coherent interface forms with equally distributed misfit dislocations. During loading the atoms are displaced according to an applied strain increment in the longitudinal loading direction via a linear transformation applied on all atoms within the simulation box. After that the atoms are relaxed for 4000 time steps with respect to local interatomic forces, as well as to the global axial stresses that act normal to the loading direction. This relaxation time interval is found to be sufficient to obtain macroscopic equilibrium configurations. During relaxation the scalar product of the global force and momentum vectors containing the force and momentum components of all atoms is evaluated. A negative value indicates that the momentum would increase the total energy. In this case all momenta are reset to zero. The uniaxial strain in the sample is maintained during the relaxation. Note that the simulation algorithm relaxes the stress components arising from cross-contraction by deforming the simulation box accordingly.

To identify nucleation and evolution of defects we use the common neighbour analysis (CNA). The CNA classifies pairs of atoms according to their local environment (Honeycutt and Andersen, 1987; Clarke and Jónsson, 1993) and can be used to detect dislocation cores, stacking faults and other defects in crystalline structures. A key issue of the present work is to identify interfacial slip and to investigate its contribution to the overall plastic deformation. Interfacial shearing of Rachinger type, which is considered here, refers to the relative displacement of adjacent phases under the action of high shear stress. In contrast, Lifshitz sliding denotes the displacement of individual grains in diffusional creep via stress-driven diffusion of vacancies and plays a significant role only at elevated temperatures. For the given morphology of the nanocomposite, interfacial shearing can not occur without some other forms of accommodating mechanisms like plastic slip within the individual phases either by dislocation slip or by mechanical twinning or interfacial decohesion at the platelet front ends. We follow the definition of the slip vector s published by Zimmerman et al. (2002)

$$\mathbf{s}_i = \frac{1}{n_s} \sum_{i \neq j}^{n_s} \mathbf{r}_{ij} - \mathbf{r}_{ij}^0, \tag{5.1}$$

where n is the number of nearest neighbours of atom i, n_s is the number of slipped neighbours, $\mathbf{r}_{ij}$ and $\mathbf{r}_{ij}^0$ are the position vector differences of atom pair ij in the current and a fixed reference configuration, respectively. Here, the initial relaxed stress-free sample is defined as the reference configuration. This vector quantity is a measure for the slip of adjacent atomic planes and indicates local plastic deformation by slip either at the interface or within the ductile phases. Since the evaluation of the slip vector refers to the initial configuration, pre-existing defects or interfaces will not be visible unless they start to move.

5.3 Simulation results

We study plastic deformation of metallic nanocomposites with multi-million atom MD simulations under quasi-static loading conditions and determine the resulting macroscopic strength from the computed stress-stain curves under various geometrical variations of the nanostructure. The stress-strain curves obtained from the MD simulations presented here have some common features, such as a saw tooth-like behavior as seen in Figure 5.3. The sudden drops in stress can be correlated to the nucleation of single partial dislocations.

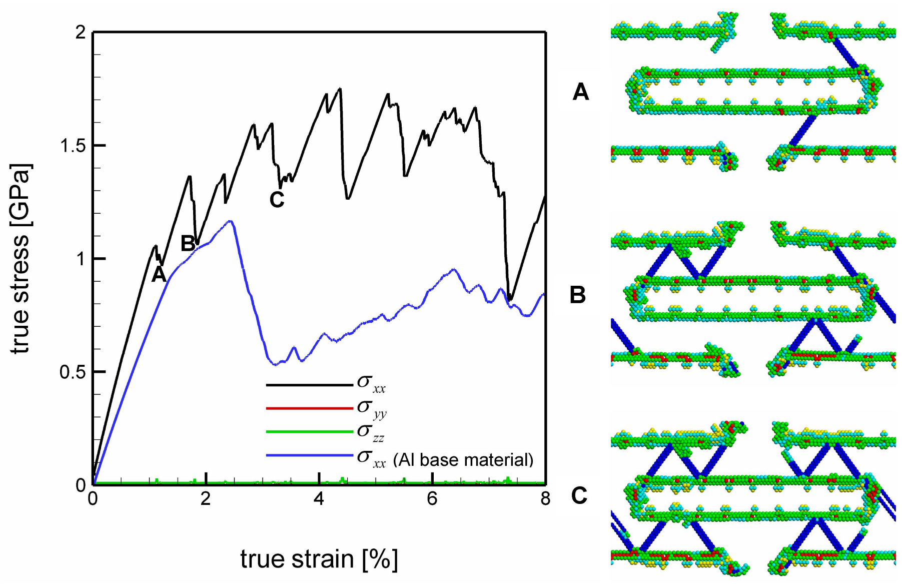

Figure 5.3: A typical stress-strain curve is shown for a fine structured material with obtained from the MD simulation. Right hand side shows the CNA, yellow atoms denote interface atoms, blue atoms denote stacking fault planes.

For structures with larger matrix volumes between the inclusions, the number of defects that participate in plastic deformation increases and the superposition of multiple nucleation events results in smoother stress-strain curves. The characteristic feature of a relatively coarse structured nanocomposite is a sharp drop in stress after reaching the initial yield point. After initial yielding the stress fluctuates around an average value that is usually lower than the stress immediately prior to the onset of plasticity. This behavior is explained with the lack of mobile defects in the initial ideal crystal structure. In this work we define the flow stress as the average stress in the range of 6-8% total strain, consistent with the definition used by Schiøtz and Tolla (1998). In this range of plastic strain, a significant density of mobile defects has developed to accommodate the applied loading. Furthermore we adopt the labeling convention indicated in 5.1 for the characteristic length scale of the nanocomposite which corresponds to the distribution wavelength d of the embedded platelets along the loading direction (Figure 5.1).

We observe various atomistic mechanisms of defect nucleation and migration that are

Table 5.1: Labeling used in this work for the distribution wavelengths d of the embedded platelets in loading direction.

	NC01	NC02	NC03	NC04	NC05	NC06	NC07	NC08	NC09
d [nm]	10,3	15,3	20,6	30,9	41,0	61,5	82,5	163,5	330,2

characteristic of plastic deformation in the biomorphous metallic nanocomposites. Interfacial shearing is always accompanied by an intraphase glide mechanism. Up to NC06 only extended partial dislocations are nucleated. We find that the platelet front ends are the sites for first dislocation nucleation due to the stress concentration there. Extended partials are nucleated usually at the platelet corners and migrate into the thin channels of the Al phase where they interact with the Ni/Al interfaces by pinning or reflection, see Figure 5.4. When a dislocation is reflected at the Ni/Al interface, the difference in the Burgers vectors of the incoming and outgoing dislocation is accommodated by a finite interfacial slip step in the shearing interface so that the total Burgers vector is conserved. Since the Ni/Al interface is semi-coherent, we observed in some rare cases that a dislocation can migrate into the Ni phase.

We start our investigation with studying the effect of the nanostructural morphology on the macroscopic strength. Even though both constituents are ductile metals, interfacial decohesion is observed for materials with defected interfaces. We show that due to the biomorphous nanostructure the materials strength is invariant to both partial interfacial decohesion, as well as to the nanostructural morphology below a critical length scale. We then study the effect of nanostructural scaling on the nucleation and evolution of interfacial decohesion. Finally we present size dependent plasticity for the bio-inspired morphology and investigate the contribution of interfacial slip to the total slip as a function of the structural refinement. As a measure for the slip contribution we define the quantity

$$\bar{s}^{Al} = \frac{1}{\bar{s}^{Al} + \bar{s}^{Ni} + \bar{s}^{int\,Al}} \sum_i |s_x^{(i)Al}|, \tag{5.2}$$

where $\bar{s}^{Al}$ is the accumulated x-component of the slip vector for Al atoms with respect to the total slip, i.e. the accumulated x-component of all atoms $\bar{s}^{Al} + \bar{s}^{Ni} + \bar{s}^{int\,Al}$. The contributions of Ni and Al interface atoms $\bar{s}^{Ni}$ and $\bar{s}^{int\,Al}$ are computed analogously. Al interface atoms are atoms of the Al phase that have one neighbouring Ni atom at least. We note that this quantity is an arbitrarily chosen quantity and only gives a qualitative measure of the real contribution of the slipped atom species to the total plastic deformation.

5.4 Effect of nanostructural morphology

Critical for hardness and resistance to plastic deformation of the metallic nanocomposite is the efficient geometrical confinement of the plastic phase by reinforcements.

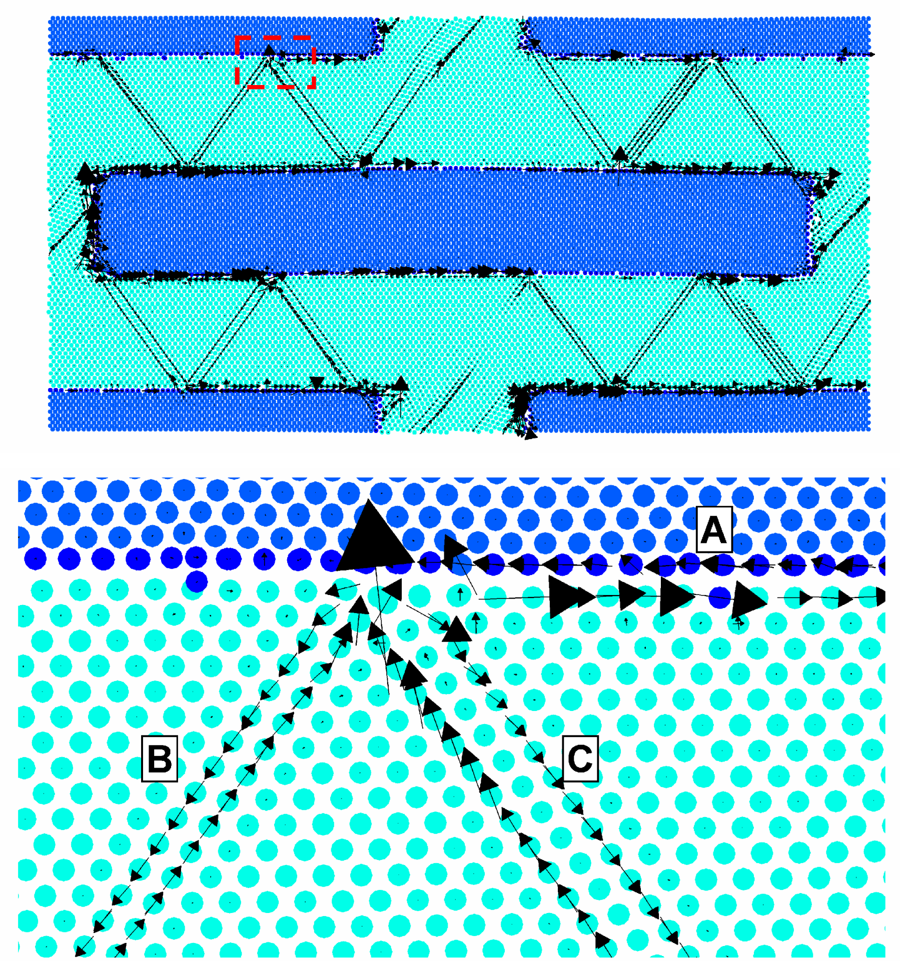

Figure 5.4: Visualization of slip vector analysis shows the characteristic atomistic mechanisms that govern the plastic deformation of biomorphous metallic nanocomposites. Shown are the total structure (top) and a close view on the interface (bottom). Highlighted areas: (A) Interface shearing, (B) extended stacking fault, (C) mechanical twin.

The degree of geometrical confinement depends both on the interfacial properties as well as on the structural morphology. In this section we compare plastic deformation behaviour of the Ni/Al nanocomposite with different nanostructures and study the importance of platelet morphology for the composite resistance to plastic deformation. We consider four different samples “Standard“, “Layered“, “Short“ and “Quadratic“ with equal spatial platelet distribution wavelengths but different platelet morphologies, as shown in Figure 5.5. Morphology “Standard“ consists of platelets of high aspect ratio that overlap by about 50 % of the platelet length. The reinforcing platelets in the “Layered“ sample keep minimal spacing in longitudinal direction and form a quasi-layered substructure. The platelets volume content is about the same as in morphology “Standard“. The volume content of the platelets in morphology “Short“, with the platelet aspect ratio close to one, is much smaller than in morphology “Standard“ and “Layered“. The quadratic platelets in morphology “Quadratic“ have the same volume content as in morphology “Standard“ and are distributed with minimal overlap. The CNA in Figure 5.5 shows different atomistic features of the deformed samples at about 5.6 % of applied strain. The slip vector analysis is shown on the right hand side in Figure 5.5 where the x-component of the slip vector is colour coded omitting atoms with slip vector magnitude less than 0.01 nm.

The computed stress-strain curves are shown in Figure 5.6. We start with comparing the materials response of morphology “Quadratic“ and “Standard“. Note that both materials have the same volume content of reinforcing platelets. In the initial elastic response both curves deviate slightly indicating that material “Quadratic“ is more compliant than material “Standard“ with platelets of high aspect ratio. Both curves show yielding at the tensile stress of about 1.7 GPa and comparatively small fluctuations of the flow stress. We consider now the response of material with morphology 'Short'. The volume content of the reinforcing platelets is only half of that of materials “Quadratic“ and “Standard“. The reduction in stiffness is evident. The initial yield stress is approximately the same as that of materials “Quadratic“ and “Standard“. However, after initial yielding the flow stress drops down to a value of only 50% of the initial yield stress. The material with morphology “Layered“ contains a similar volume content of the reinforcing Ni phase; however, the platelets are distributed with narrow spacing in loading direction. This configuration gives rise to high stress concentrations at the platelet front ends. During loading the interface at the front ends can not sustain the high tensile stress and delaminates even though both the constituents are ductile metals. The result is a sudden drop of the macroscopic stress level at about 5% strain. However the delamination does not lead to total failure of the structure. The interfacial cracks do not grow into the soft Al matrix and the flow stress fluctuates on the same level as in materials “Quadratic“ and “Standard“.

We summarize our observation for nanostructural scaling NC07. The macroscopic stiffness and strength are found to be invariant to morphological changes such as variation in platelet aspect ratio. Stiffness and strength are very sensitive to the volume content of the reinforcing Ni Phase. Narrow platelets spacing gives rise to partial delamination of the interface at the platelet front ends but does not lower

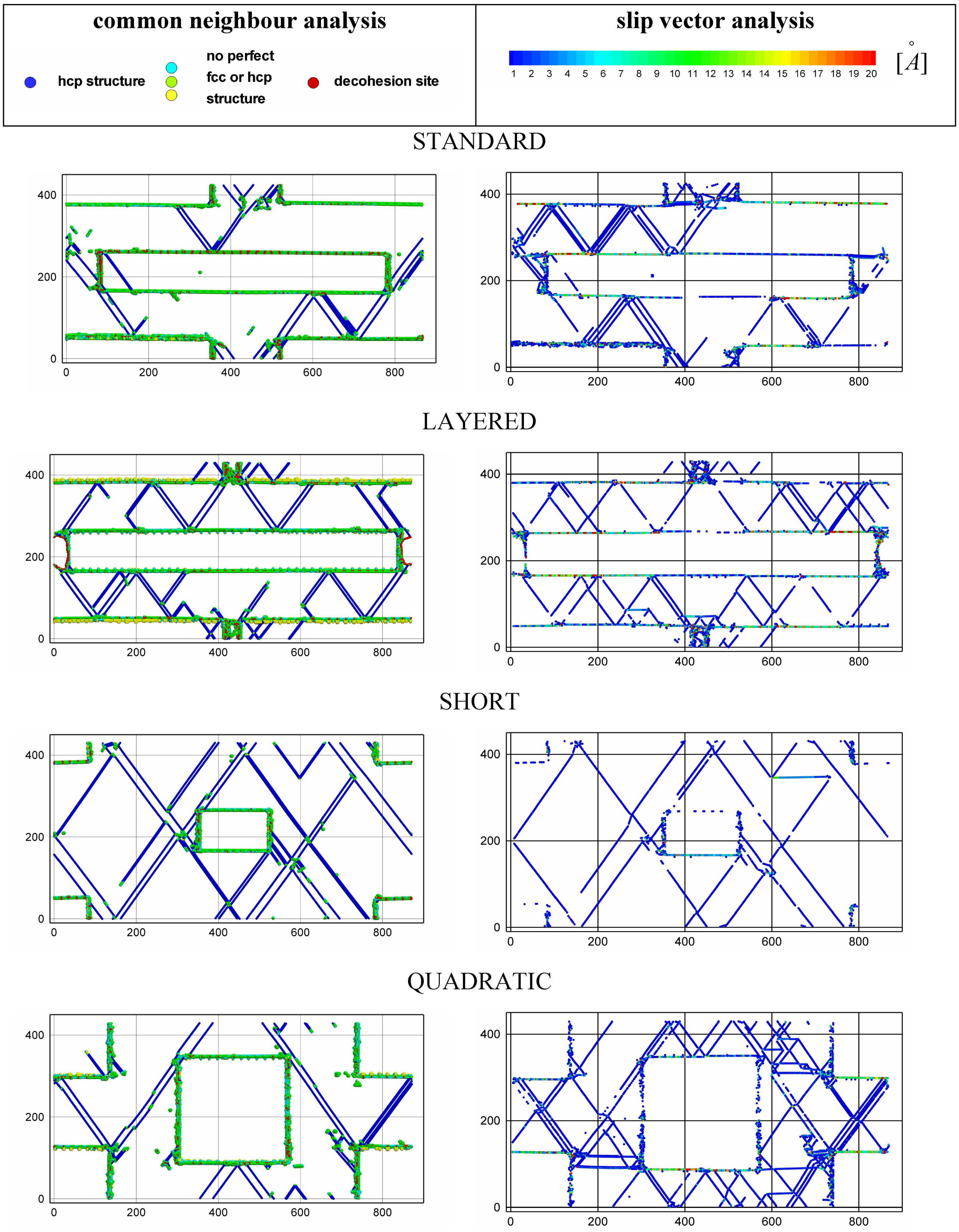

Figure 5.5: Comparison of four nanocomposite materials with different nanostructural morphologies. The spatial distribution wave length of the platelets is kept constant. 4a) Material “Standard“, 4b) Material “Layered“, 4c) Material “Short“, 4d) Material “Quadratic“. Common-neighbour analysis (left column): The hcp atoms indicate twin boundaries as single blue lines or stacking faults as double blue lines. Isolated light green dots represent defected atoms of the dislocation cores. Visualization of slip vector (right column): Shown is the distribution of the x-component of the slip vector.

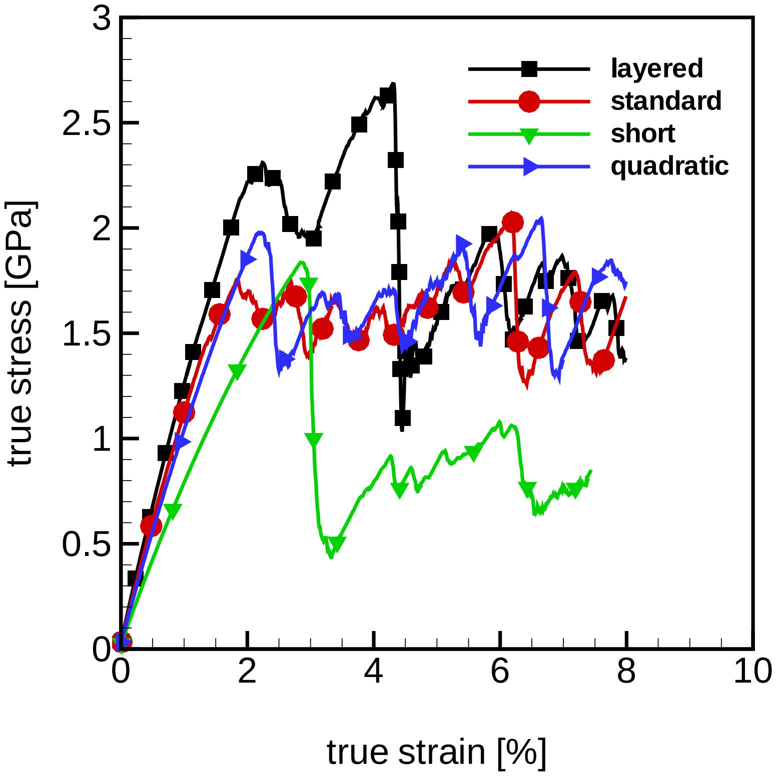

Figure 5.6: Stress-strain curves for materials NC07 with different microstructural morphology as shown in Figure 5.5 .

the strength of the biomorphous metal nanocomposite.

5.5 Enhanced plastic confinement due to biomorphous design

To further understand the impact of the design of the interface network on the macroscopic strength we constructed nanocomposite materials with regular distributions of platelets with quadratic cross-sections. The interface area is equivalent to that of the biomorphous nanocomposites for the same scaling. Figure 5.7 (left) shows the CNA for scaling NC08. Only a few partial dislocations can be observed within the Ni platelets and twin formation occurs predominantly within the Al phase. As described later in more detail, the strength of the regular design is usually smaller than that of the biomorphous design.

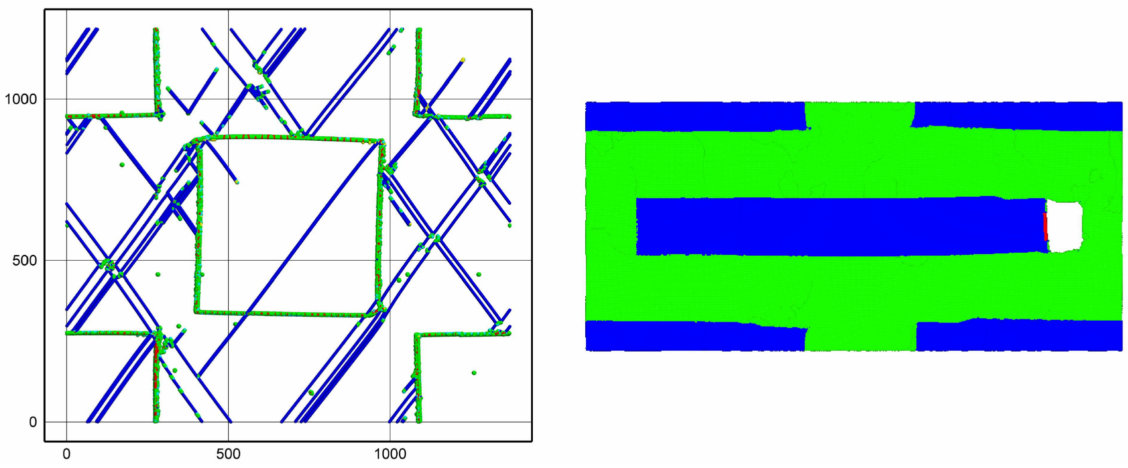

Figure 5.7: Left: CNA analysis for nanocomposite with regularly distributed quadratic platelets for scaling NC08. Right: structure of the flawed biomorphous nanocomposite under large applied strain. Colours represent different atom types (not CNA). The pre-existing interfacial flaw is denoted by red atoms that do not interact with Al phase (green) at the front-end of the central Ni platelet (blue).

We also investigated the effect of pre-existing interfacial flaws on the materials performance and tested the flaw tolerance of the biomorphous design. Flaw tolerance is a key issue for engineering robust materials (Gao et al., 2003; Ji et al., 2004; Buehler et al., 2006). To model interfacial delamination we constructed Ni atom species that interact with the Ni atoms only. Figure 5.7 (right) shows part of the interface at the front-end of the center platelet consisting of Ni atoms (marked in red) that do not interact with the Al phase. This configuration represents an interfacial Griffith crack that experiences a pure mode I loading under the tensile loading applied. During loading the crack opens up and grows along the interface towards the corners of the platelet. Under further loading the crack simply blunts without propagating further into the Al. We insert this type of interfacial flaw into three nanocomposite structures with different scaling and study the effect on the macroscopic strengths. Figure 5.8 shows the strength-scaling variation of flawed biomorphous nanocomposites and nanocomposites with regularly distributed quadratic platelets in comparison with crack-free biomorphous nanocomposites. The computation of the strength of the biomorphous designs is described in detail below and is used here for comparison. To define the strengthening effect of plastic confinement, an Al base material was constructed by inserting quadratic Ni inclusions of very low volume contents in an Al matrix to introduce nucleation sites for dislocations. The material consists of Al with 60 parts per million (ppm) Nickel content in form of quadratic particles with size 5 nm × 5 nm. For a perfect Al single crystal the yield stress obtained by MD simulation would match the theoretical shear strength, thus a certain defect microstructure has to be considered in the initial configuration. This material is taken as the reference material representing effectively the properties of the Al matrix without reinforcement. The computed strength amounts to 830 MPa (blue line in Figure 5.8). The regular design exhibits a weaker size dependence in the strength than the biomorphous design, with a flow stress of around 1.4 GPa for all three variants tested here. Note that the biomorphous design in contrast shows its maximum strength and thus very strong size dependence in this length scale regime. The macroscopic strength of the flawed specimens proves to be strongly size dependent. For scaling NC08 the strength is approximately on the level of the Al base material, and increases significantly with structural refinement (Figure 5.8). The reduction of the scaling parameter from 160 nm to 40 nm leads to a strength enhancement of about 25%.

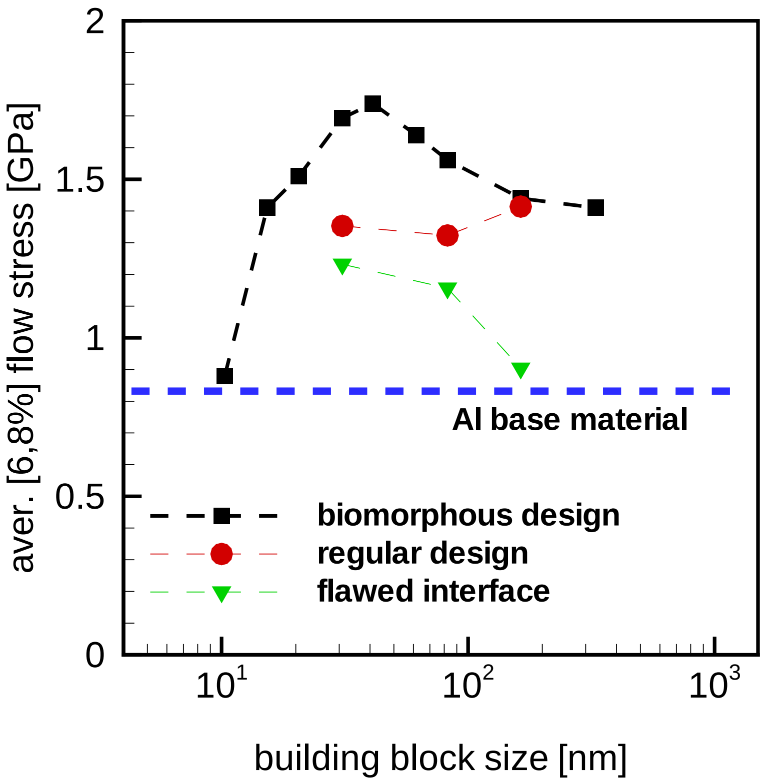

Figure 5.8: Comparison of size dependent strength between biomorphous, regular and flawed nanocomposites.

5.6 Size dependent interfacial delamination

The observation of interfacial decohesion in Ni/Al nanocomposites with ductile constituents gives rise to the question whether its occurrence is size dependent and how the damage evolution changes as a function of the nanostructural scaling. Figure 5.9 shows simulation results for three different nanostructural scalings NC06, NC07 and NC08 for the material morphology “Layered“. No initial flaw has been inserted, but the decohesion occurs during the loading of the specimens. Note again the sudden drop of the stress level of material NC07 'layered' after interfacial decohesion of the platelets front ends at about 5% strain. We observe also partial delamination in scaling NC08 at a larger strain of about 6%. However, the stress decrease is much slower in this material after decohesion occurs. We observed no interfacial decohesion in scaling NC06 and below. Figure 5.10 shows the tensile stress distributions

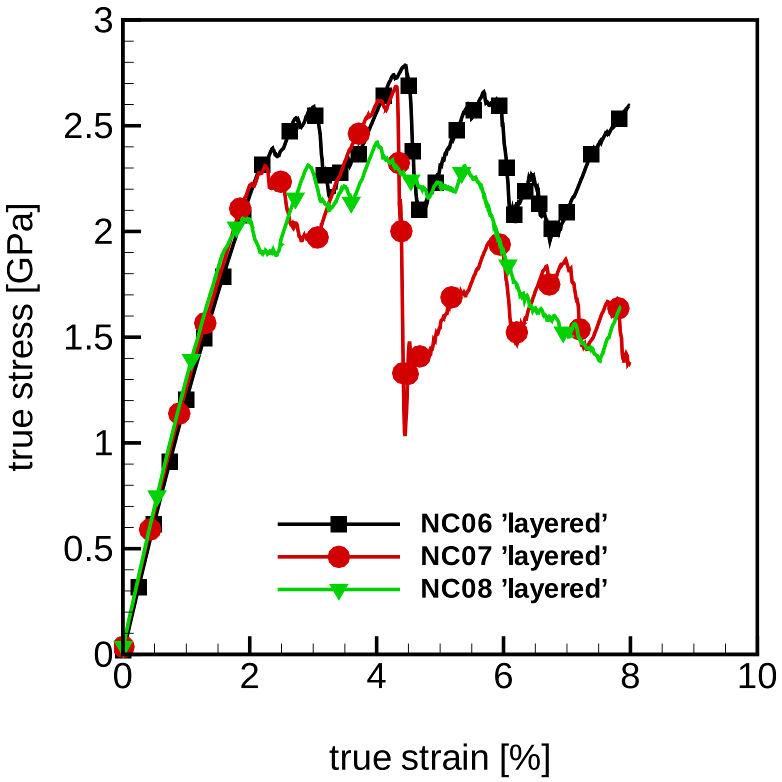

Figure 5.9: Stress-strain curves of the layered like materials shown in Figure 5.10. Note the sudden drop of the stress level of material NC07 'layered' after interfacial decohesion of the platelets front ends at about 5% strain. Stress decreases much slower in material NC07 'layered' after initiation of decohesion at about 6% applied strain.

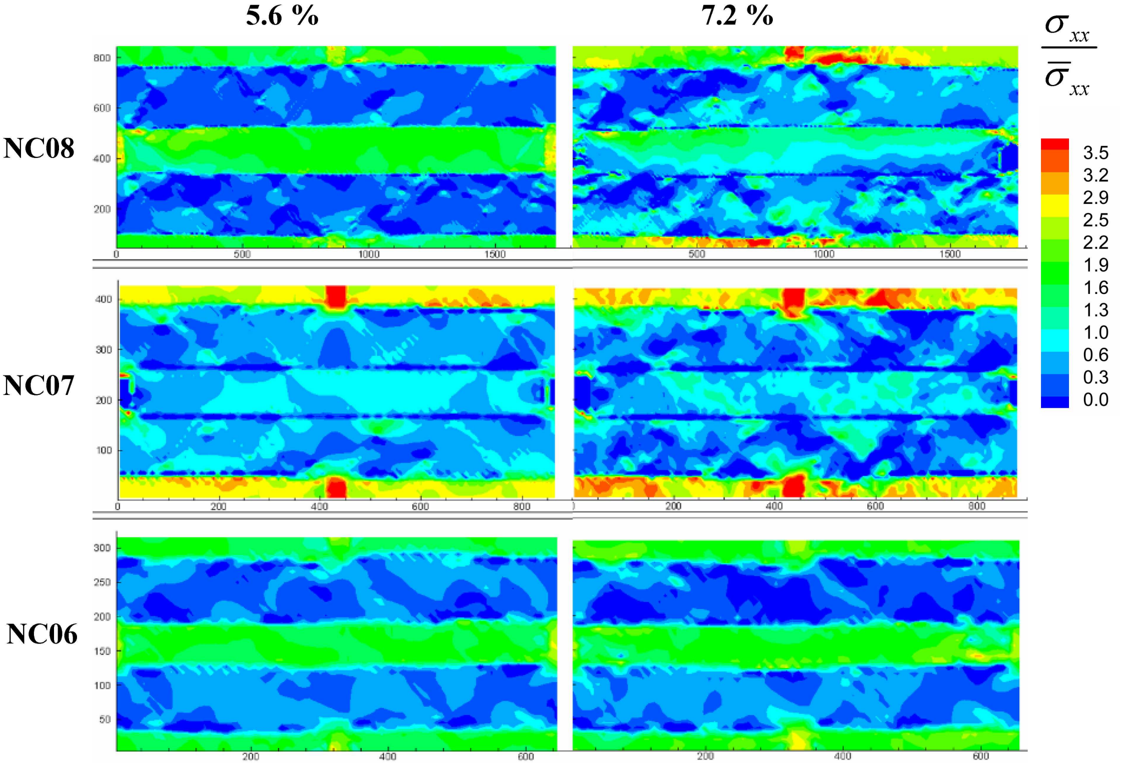

Figure 5.10: Tensile stress distribution σ_{xx} in the material normalized with respect to the average tensile stress $\bar{\sigma}_{xx}$. Shown are layered like microstructures for three scalings NC06, NC07 and NC08 at two different strain levels 5.6% (left) and 7.2% (right). Stress is normalized with respect to the macroscopic stress.

in the different scalings before and after onset of decohesion. Note the stress concentration around the delaminated front ends. The interfacial decohesion in scaling

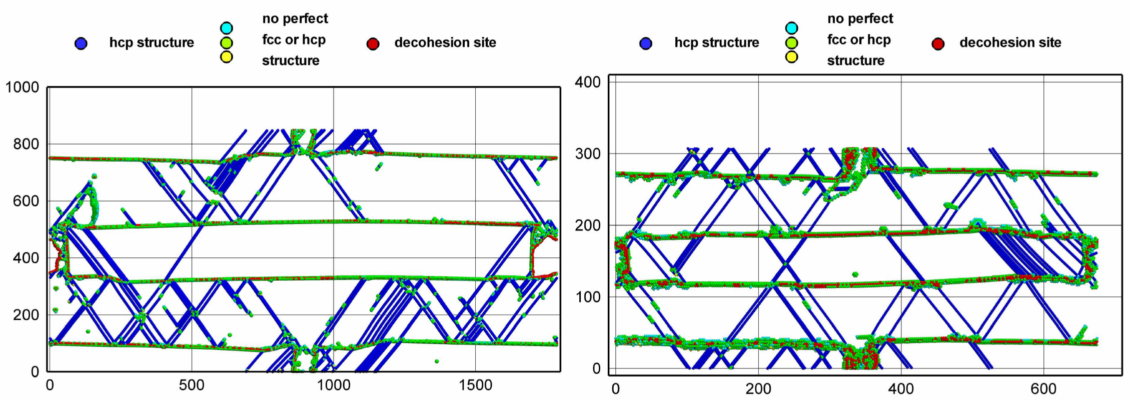

Figure 5.11: CNA visualization of scaling NC06 and NC08 at a large macroscopic strain. Note the initiation of interfacial delamination in scaling NC08 (left). No delamination occurs in scaling NC06. However, the platelet front ends undergo severe plastic deformation by twinning formation.

NC07 leads to a sudden total relaxation of the center platelet which is reflected by the stress drop of the macroscopic stress. For NC08, in contrast, the center platelet is still partially intact and carries tensile stress even after the onset of decohesion. The relaxation of the center platelets is delayed and results in a smooth decay of the flow stress. The high tensile stresses at the platelet front ends in scaling NC06 do not lead to decohesion at all; however, severe plastic deformation of the platelet tips appears in the CNA; see Figure 5.11, right. The densely packed blue lines of hcp atoms denote extensive mechanical twinning.

5.7 Effect of nanostructural scaling on strength

To investigate the scaling effects on the deformation behavior, we consider 9 different nanocomposite materials with building block sizes d ranging from 10 to 320 nm, see 5.1. The elastic behavior of materials depends on the stretching and bending of bonds between individual atoms. In polycrystalline and composite materials the

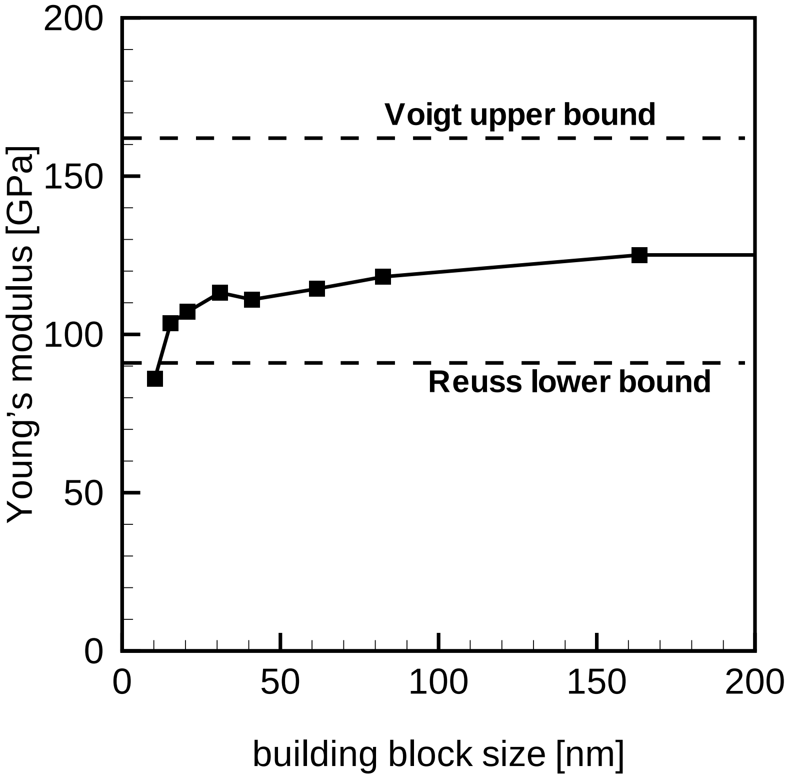

Figure 5.12: Young's modulus as a function of building block size d.

bonds in grain boundaries or interfaces are weaker than the bulk bonds in the grain or phase interior. With increasing grain refinement the fraction of interfacial atoms and hence the fraction of weaker bonds increases. Figure 5.12 shows the variation of Young's modulus as a function of building block size. The plot includes the bounds from the two mixing rules of the Reuss and Voigt systems (Gibson, 1994) where the Voigt upper bound is defined as

$$E^{Voigt} = \Phi E^P + (1 - \Phi)E^M \tag{5.3}$$

and the Reuss lower bound as

$$\frac{1}{E^{Reuss}} = \frac{\Phi}{E^P} + \frac{(1 - \Phi)}{E^M} \tag{5.4}$$

where E^P, E^M and Φ are the Young's modulus of the platelet material, the Young's modulus of the matrix material and the volume concentration, respectively. We

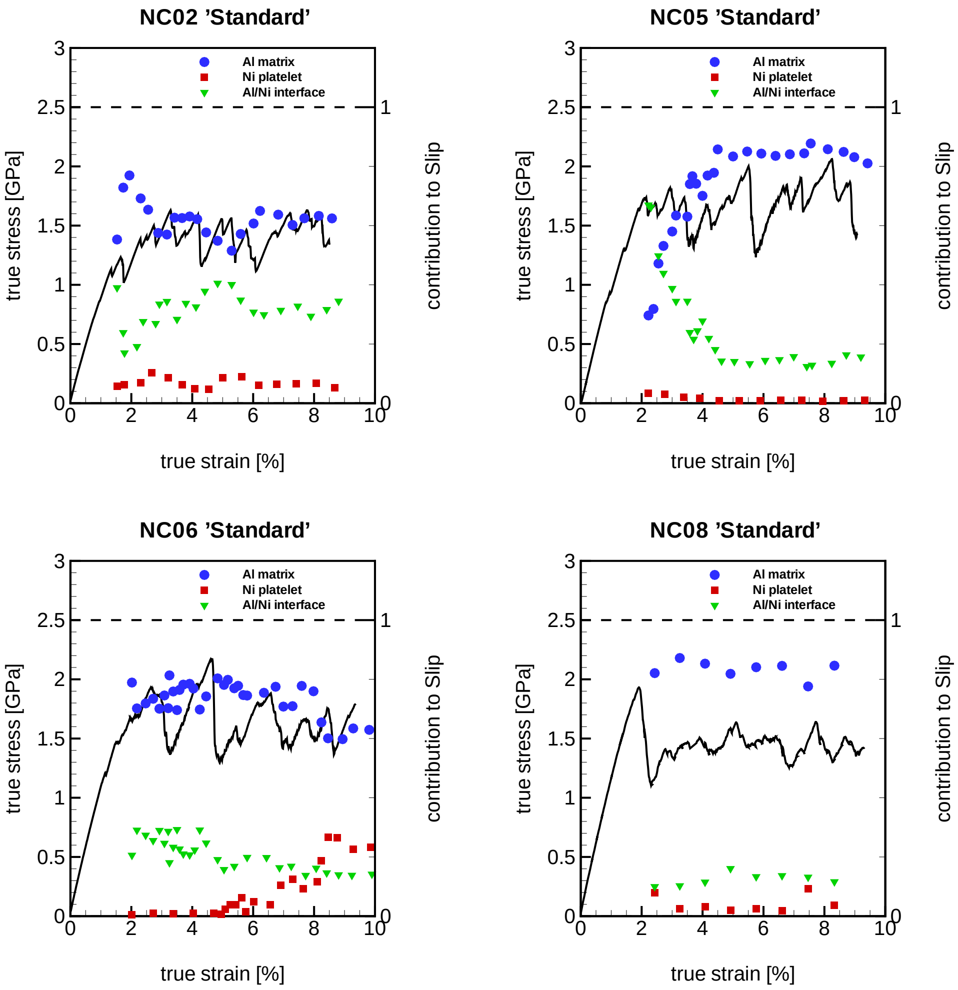

Figure 5.13: Combined plots of stress and slip as a function of applied strain for scalings NC02, NA05, NC06 and NC08.

present here simulation results for the different morphologies, where the individual contributions of dislocation activity in matrix and inclusions and interfacial slip to the total plastic strain are quantified. As a measure of the contribution of interfacial slip we defined the accumulated slip of each atom species, see Equation (5.2). It is seen in Figure 5.13 that plastic deformation and strength of the metallic nanocomposites as well as the relative contributions of the different deformation mechanisms are size dependent. In the coarsest structured material NC08 the contribution of dislocation slip to the plastic deformation of the individual phases remains constant throughout the deformation process. With increasing refinement we observe more interface mediated deformation at the onset of plastic deformation. NC05 shows the strongest variation where the contribution of interfacial shearing is very high at the initial yield point and drops down to finally reach a plateau at about 5% strain. At the same time the contribution of dislocation mediated plasticity in the

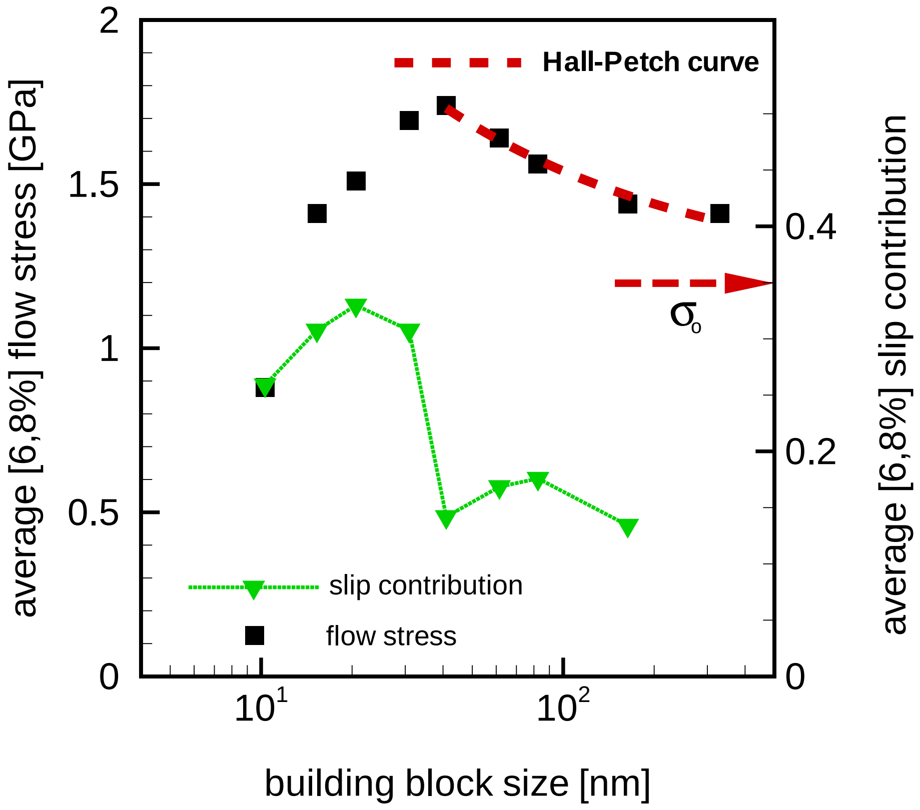

Figure 5.14: The size dependence of strength and its correlation with interfacial shearing for morphology 'Standard'

Al matrix increases continuously. The nanostructural scaling strongly affects the strength of biomorphous metallic nanocomposites. In Figure 5.14 the size dependent macroscopic strength is correlated with interfacial shearing. The flow stress of the biomorphous material reaches a maximum at an scaling of about 50 nm. This scaling represents the cross over length scale between interfacial shearing and dislocation glide dominated regimes. Figure 5.14 also includes a fit curve to data points in the dislocation dominated regime, following the Hall-Petch relationship (2.1) (Hall, 1951; Petch, 1953), where σ_0 is the lattice friction stress and k the Hall-Petch constant. The curve is fit to data points within the length scale regime of 50 to 330 nm and extrapolates the strength-size dependency into the coarse structured regime. The best fit was obtained for the parameters $\sigma_0 = 1.2\,\mathrm{GPa}$ and $k = 0.11\,\mathrm{MPa}\sqrt{\mathrm{m}}$.

5.8 Discussion

Both constituents Ni and Al are intrinsically ductile materials so that the maximum strength achievable by this material pairing is determined by the flow stress of Ni being the harder constituent. Because of the mismatch in strength, the plastic flow within the composite is mainly confined to the Al layers that are locally under shear loading. Due to the chosen structure, the dislocations are geometrically confined to narrow Al channels, which effectively strengthen the composite material. The role of the different deformation mechanisms and the consequence for the mechanical properties of the composite is discussed in detail in the following sections.

5.8.1 Deformation mechanisms

In our investigation we show a quantitative analysis of the role of dislocation mediated plasticity and interfacial shearing as deformation mechanisms. Dislocation nucleation, dislocation glide, mechanical twinning and interface shearing are observed at all investigated length scales. The findings from the analysis of the deformation mechanisms are summarized in table 5.2

The first dislocation nucleation events occur exclusively at the platelet front-ends. The cross-over from extended partial dislocation to full dislocation dominated plastic deformation takes place within the scaling range from 160 nm to 330 nm. In the regime from 50 to 160 nm extended partial dislocations and their mutual interactions as well as their interactions with the interfaces dominate plastic deformation of the material. In the scaling regime below 50 nm the Al interlayers are mainly transected

Table 5.2: Summary of the size dependent governing deformation modes in biomorphous metallic nanocomposites.

	$< 50\,\mathrm{nm}$	$[50\,\mathrm{nm}, 160\,\mathrm{nm}]$	$> 160\,\mathrm{nm}$
Onset of plasticity	Simultaneous nucleation of extended partials in interlayer and interfacial shearing	Nucleation of extended partials at platelet front ends	Nucleation of partial and full dislocations near platelet front ends
During large deformation	Stacking fault formation in interlayer accompanied by interfacial shearing, twinning	Deformation twinning, reflection of extended partials in interlayer by interface shearing	Nucleation of full dislocations everywhere

by extended stacking faults, simultaneously interfacial shearing occurs at the onset of plastic deformation. At high strains, extensive interfacial shearing is accompanied by growth of mechanical twins.

The dislocation-interface interaction in the metallic nanocomposite is fundamentally different from that in single-phase nanocrystalline metals, in which dislocations are pre-dominantly absorbed by grain boundaries (Schiøtz et al., 1999; Schiøtz and Tolla, 1998; Swygenhoven et al., 2002). In the case of metallic nanocomposites considered here the plastic deformation in the size regime 20 to 160 nm characterized by a specific localized flow pattern. Dislocations are strongly confined between the hard/soft interfaces and travel from their nucleation sites into the Al channel where they interact mainly by reflection, in rare cases by transmission into the Ni phase. The ability of the interface to reflect incoming dislocations is very important for the flow stress of the material and is a process that is fundamentally different from grain boundary dislocation interaction in polycrystals. The effect is due to the elastic mismatch between Ni platelets and Al matrix that causes a repelling image force on the incoming dislocations. Even though tangential tractions at the interface are easily relaxed by the motion of misfit dislocations, the normal component of the tractions still implies a repelling image force. If interfacial shearing is difficult, this image force is so large that dislocations do not immediately reach the interface, but are stalled at a distance to the interface until interfacial shearing is triggered. In this case dislocation nucleation and motion is limited and a single slip system cannot be activated more than one time. In the other extreme case of easy interfacial shearing, the dislocation is simply annihilated by the weak interface – as also observed in MD simulations of polycrystals – and the corresponding slip system may operate multiple times.

The behavior of the studied nanocomposite shows an intermediate behavior. On the first view, the interface seems to be surprisingly weak. Since the interaction of Ni and Al atoms is strong, one might expect that interface shearing should be of a very limited importance in this system. However, due to the large lattice mismatch between the Ni platelets and the Al matrix, the density of misfit dislocations at the interface is rather high and interfacial shearing occurs easily. The strength of the interface is reflected in the fact that delamination occurs only under very extreme conditions and only at high plastic strains. Dislocations can very effectively be absorbed at free surfaces in the case of such delamination of the interfaces.

In highly confined metal phases deformation caused by interfacial shearing can only be accommodated by mechanical twinning and twin boundary migration in the plastic phase. Note that twinning in nanostructured Al has also been reported in the literature (Schiøtz et al., 1999; Schiøtz and Tolla, 1998; Swygenhoven et al., 2002; Yamakov et al., 2003, 2002). With increasing refinement the deformation is almost entirely mediated by interfacial shearing. At ultrafine scales, eventually, the volume concentration of interface atoms becomes very large so that the material behavior is governed by the deformation of a quasi-amorphous structure at the interfaces.

5.8.2 Mechanical properties

Flow stress in coarse structured composites is determined by the presence of the internal interfaces between the soft Al phase and the hard Ni platelets that act as barriers to dislocation motion. For small structural sizes, the flow stress is mainly determined by the possibility of dislocation reflection at the interfaces. The initial samples considered here as atomistic models for the Ni/Al nanocomposite are highly idealized structures. The high stress levels before the first load drop that indicates the point of initial yield are caused by the lack of any initial dislocations. The definition of the flow stress as the stress average value within the strain interval of 6 to 8% total strain is therefore necessary. At this stage of deformation a reasonable defect density has developed within the structure and the shape of the platelets is fairly rounded off. The biomorphous design that arranges reinforcing hard platelets of high aspect ratio in a soft ductile matrix is critical for the increase in strength within the scales from 50 to 160 nm. Below 50 nm the material strength is found to be invariant with respect to platelet morphology if the volume content of the reinforcing phase is kept constant. Furthermore, the materials strength becomes invariant to fluctuations of the platelet distribution that could give rise to narrow platelet spacing below the same scaling of 50 nm. This value seems to be a critical refinement level where the design of the interface network seems to play only a minor role for the mechanical properties of metallic nanocomposites.

The presence of interfacial flaws at the platelet front-ends dramatically decreases the strength of the materials above a scaling of about 80 nm. The initial flaws always grow to cover the entire front-end thus creating a large free surface area. As a result the effective plastic confinement is strongly damped since dislocations can easily be absorbed. Below this scale the material exhibits a good flaw tolerance. In this size regime the flow stress is determined by a few discrete dislocation processes within confined Al channels between neighboring platelets. A robust design of hard/soft metallic nanocomposites requires reinforcements of large aspect ratio to limit the size of advancing interfacial cracks when the interfaces have only little tensile resistance. The large aspect ratio of reinforcements would be even more important in case the tensile strength of the interfaces is low.

Conventional polycrystals are known to exhibit strong dependence of strength on the grain size that causes hardening with increasing refinement (Hansen, 2005). This behavior has been observed to follow the Hall-Petch relation, see (2.1). Our investigations reveal that nanocomposites with defect free interfaces may show a hardening effect of the Hall-Petch type within the length scale regime of 50 to 160 nm, see Figure 5.14. The estimated value for the Hall-Petch constant for the investigated Ni/Al nanocomposite is an overestimation but of the same order of magnitude as obtained from experimental analysis for pure Al (Hansen, 2005). The background stress σ_0, however, is overestimated by several orders of magnitude by our MD simulations. This is due to the fact that only a limited number of slip systems are available in the quasi two-dimensional analysis of perfect structures at $0\,K$ presented in this work.

The commonly excepted explanation of the hardening effect in polycrystals is characterized by dislocation pile-ups at grain boundaries. In atomistic investigations of nanocrystalline single-phase metals pile-ups containing a few dislocations have been observed in size regimes above the maximum strength (Schiøtz and Jacobsen, 2003). However, formation of dislocation pile-ups are not found in the metallic nanocomposites considered here. The leading dislocations on a single slip plane are eventually reflected at the Ni/Al interfaces when pushed by local buildup of stresses from following dislocations. The mechanical deformation in the regime of 50 to 160 nm is rather determined by the motion and interaction of extended partial dislocations as well as by a small amount of interfacial slip. Stacking faults and twin boundaries are observed to play the role of dislocation obstacles. Our investigations reveal that the increasing number of stacking faults and twin boundaries with increasing structural refinement causes the hardening effect of the Hall-Petch type. In the case of high-quality interfaces interfacial shearing is the limiting mechanism that causes a strong decrease in strength below a critical length scale of 50 nm. This observation is in agreement with the ’inverse Hall-Petch effect’ found for nanocrystalline single-phase metals (Schiøtz and Jacobsen, 2003; Schiøtz et al., 1999; Schiøtz and Tolla, 1998).

6 Discussion of interface controlled plasticity

Now that we have discussed the effect of confinement in the failure and deformation studies of the specific material problems considered in this work, this chapter turns towards the main findings regarding interface controlled plasticity, and relates these to the literature review.

6.1 The natural size of the plastic zone

In this work dislocation dynamics simulations of crack tip plasticity were performed at a relatively high loading rate because of computational limits. In general, a low loading rate and a large intrinsic fracture energy both increase the spread of the plastic zone, the fracture toughness and, hence, the computational costs. Also the assumed intrinsic fracture energy is rather low compared to real systems, compare with Lane et al. (2000). However, in the analysis of the critical layer thickness and bulk fracture toughness we considered the thickness dependence of the normalized fracture toughness with respect to the intrinsic value to eliminate this effect. Regarding the findings at this high loading rate, we expect that the formation of the localized slip at the crack tip is rather rate independent and so the scaling behavior for thinner films. However, we expect that the size of the plastic zone and the resulting fracture toughness for thicker films is sensitive to the loading rate because then the mobility of the dislocations within the bulk of the layer material becomes more important.

In the absence of geometrical confinement it is found that the size of the plastic zone, determined by the yield strength and the cohesive strength of the material, determines the bulk fracture toughness. However the slip localization is not beneficial for the fracture toughness at large layer thicknesses. This can be seen by considering the bulk fracture toughness that was found to be lower compared to a model with

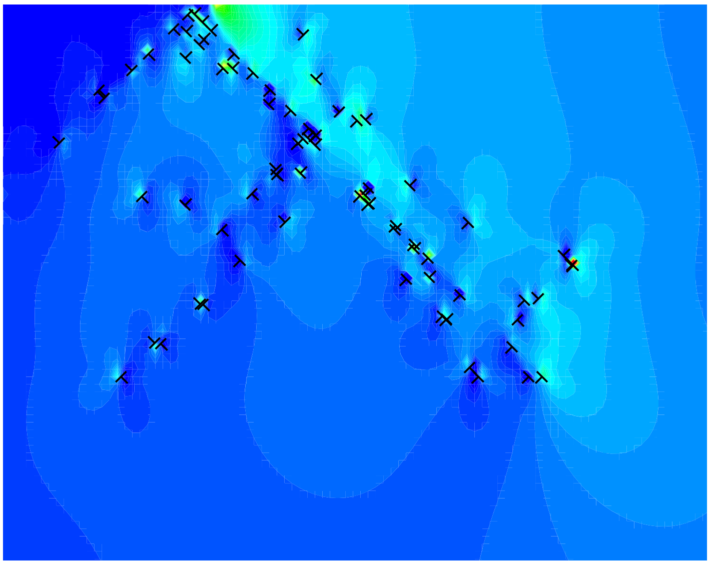

Figure 6.1: Contour plot of the crack opening stress at the crack tip and the evolving dislocation microstructure. Note the localized slip at the crack tip interacting with the bulk plasticity generated by easily operating sources in the bulk

a homogeneous source distribution, see section 4.2.1.

Interesting is the role of the local yield strength, i.e. the source strength, for slip localization. We found the largest plastic zone sizes when the cohesive strength was high but also the local yield strength. Easy source operation in the bulk tends to reduce the mobility of the dislocations stored in the slip zone at the crack tip and limits the spread of the plastic zone under the high loading rate.

6.2 The plastic flow under microscale confinement

The plastic deformation that dominates the mechanical behavior of the considered hard/soft materials under confinement has the following characteristics. Plastic flow in soft metal volumes originates from stress concentrations (crack tips, platelet corners) where it is constrained by interfaces of adjoined hard and soft phases. Under confinement, the emitted dislocations pile up near the interfaces. The back stress from pile-ups decreases the stress intensity at the operating primary source, but also increases the stress intensity at the interface. Important for the plastic flow under confinement is how this secondary stress concentration can be relaxed in order to allow further relaxation of the primary stress concentration, see Figure 6.2. In the case of strong interfaces, the high stress intensity at the interface is relaxed by dis-

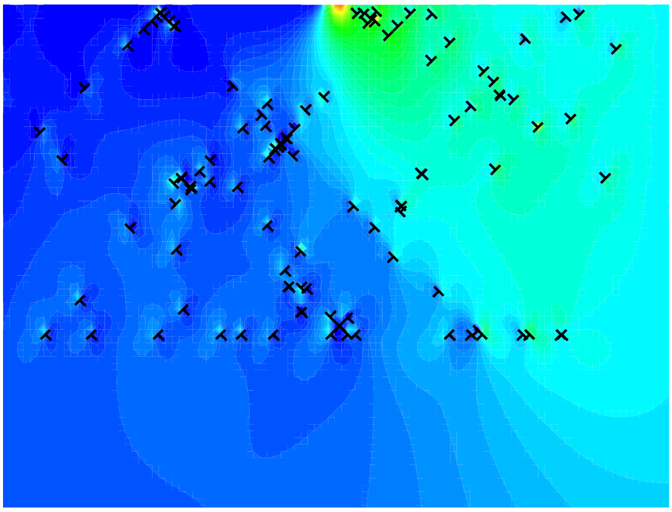

Figure 6.2: Mesoscopic simulation with strong interfaces. Sources in the vicinity of the interface are activated relaxing the stress of the dislocations piling up.

locations that are generated from operating dislocation sources in the vicinity of the interface as demonstrated in the confined crack-tip plasticity study. This leads effectively to a resulting dislocation stored in the vicinity of the interface.

The atomistic deformation analysis performed in this work indicates that, in the case of easily shearing interfaces, dislocation pile-ups at hard/soft interfaces are not stable resulting in a different relaxation mechanism. Dislocations that are pushed into the interface get finally reflected accompanied by a finite interfacial slip step. The reflected dislocations migrate back into the soft phase, see Figure 6.3.

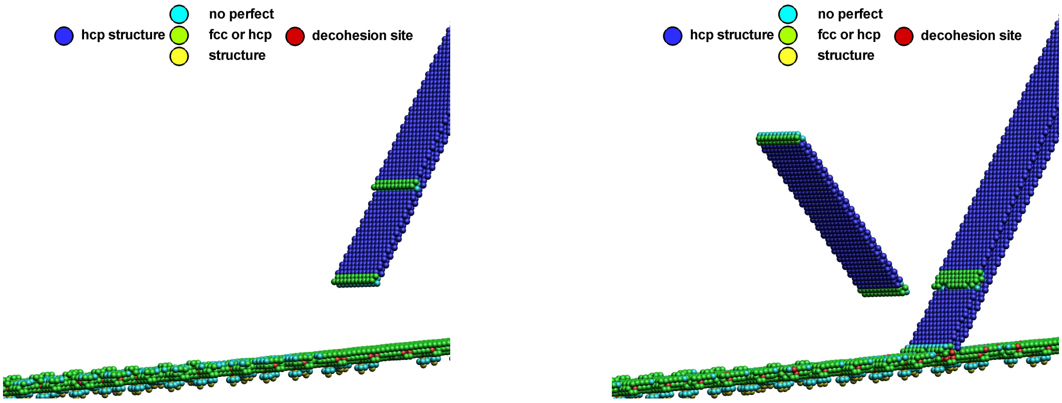

Figure 6.3: Atomistic simulation with weak interfaces. Reflection mechanism of a partial dislocation in twinning configuration at the interface, before (left) and after (right) reflection. Green atoms denote interface atoms and dislocation cores, blue atoms denote stacking fault planes.

6.3 The limiting mechanism under nanoscale confinement

Our simulation results suggest that for the biomorphous metallic nanocomposite interface shearing is not a self-containing deformation mode in the sense that it is independent of other deformation mechanisms, it is rather dislocation-assisted. The entire deformation mode of the material is rather complex. The Ni/Al interfaces are under pure shear loading due to the biomorphous design and the hard/soft material pairing. This local loading condition of the interfaces will certainly facilitate the reflection mechanism.

However, this type of dislocation reflection mechanism was demonstrated in other atomistic simulations of Cu-Ni nanolayered materials (Henager Jr. and Hoagland, 2004) where macroscopic loading was applied parallel to the interfaces. They considered an atomistic model of a gliding pre-existing dislocation in a coherent Cu-Ni layered system initially containing no misfit dislocations and demonstrated a "rebound mechanism"for the creation of misfit dislocations. In the initial samples, the 2.7 % misfit for cube-on-cube oriented Cu-Ni films is entirely accommodated by elastic coherency strain when the layers are below the critical thickness for misfit dislocation formation. Shen (2003), and recently, Shen and Leger (2006) have investigated the interaction between dislocations and interfaces in thin metal films and have particulary focused on the meaning of the resistance to interface shearing. Shen (2003) found for the two extreme cases, when atoms at the interface have the capability of unrestricted tangential slide, an oncoming dislocation tends to be reflected by the interface. On the other hand, when the interfacial atoms are not allowed to slide, the oncoming dislocation tends to be pinned near the interface and becomes temporarily immobile. Shen and Leger (2006) later introduced a sliding parameter to specify the maximum allowable sliding distance corresponding to a small local tangential displacement along the interface. They found that when the interface atoms are allowed a maximum sliding distance of only 0.5% of the atomic spacing, the dislocation motion and overall film response are already not very different from the case of a free sliding interface.

In our atomistic model semi-coherent interfaces form with equally distributed misfit dislocations due to the 13 % lattice mismatch between Ni and Al caused by the large misfit. The reflection mechanism is expected to be facilitated due to the easy-shearing interfaces caused by the dense misfit dislocation network. The reflection mechanism may be important for the propagation of slip in metallic hard/soft nanocomposites at very small scales. Under the condition of geometrical confinement pure edge dislocations are reflected at the interfaces with the line direction being parallel to the interface. In this case the incoming dislocation with Burgers vector $\boldsymbol{b}_1$ is reflected at the interface and glides back into the crystal with $\boldsymbol{b}_2$ under the action of the applied stress. A residual dislocation with Burgers vector $\boldsymbol{b}_r = \boldsymbol{b}_1 - \boldsymbol{b}_2$ remains in the interface. For coherent interfaces, the energy that is required for this process can be approximated by the self-energy of the residual dislocation $\boldsymbol{b}_r$ left behind at the interface. The energetical costs may be substantially lower when easy shearing interfaces are present due to large lattice mismatch of the two adjoining phases. Figure 6.4 shows schematically the meaning of interface shearing for the spread of dislocation based plasticity. At small strains, single residual dislocations may be accommodated by reacting with the present misfit dislocations that easily glide along the interfaces. At large strains, successively reflected dislocations can only be accommodated by extensive interface shearing. The spread of plasticity by propagation of slip is therefore expected to be controlled by the mobility of the present misfit dislocations at small strains, and by the shear strength of the interfaces for large strains. The local shear stress at the interface is required to overcome the shear strength in order to activate the reflection mechanism. Thus, the interfacial shear strength becomes the controlling factor for the spread of the plastic flow at small scales.

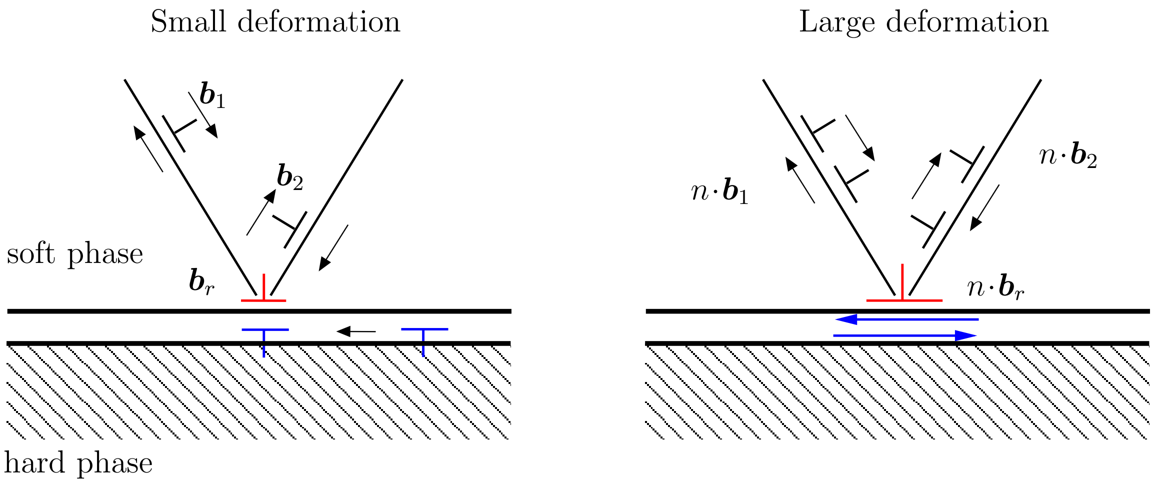

Figure 6.4: Schematics of the proposed slip propagation mechanism in nanocomposites with easily shearing interfaces.

In the crack-tip plasticity study presented in this work the interfaces are assumed to have infinite resistance. In the mesoscopic dislocation dynamics model the number of present Frank-Read sources is limited for layer thickness of 300 nm as sources are homogenously distributed within the layer material. Below 300 nm, the high stresses due to the interface dislocation pile-ups can not be relaxed because there is no sources available. For easily sliding interfaces in very thin confined metal layer, the back-stress on the crack-tip source could be relaxed by this reflection mechanism and further dislocation nucleation right at the crack tip would be possible. Consequently, it can be speculated that for easily sliding interfaces the fracture toughness of the layer materials would be higher at very small thicknesses compared to interfaces with strong bonding.

6.4 Scaling behavior under submicron confinement

Our atomistic and mesoscopic simulation results suggest that the scale dependence is related to the dislocation mean free path. In case of localized plastic flow originating at the interfaces, the mean free path is directly related to the scaling of the materials microstructure and gives rise to a high scaling sensitivity. When the plastic flow is taken over from the volume material at larger scale it is only indirectly related to the microstructural scaling. The dislocation mean free path is then a complicated function of evolving dislocation microstructure.

In our discrete dislocation and molecular dynamics simulations, dislocations are generated from randomly distributed bulk sources (DD), respectively, from random interaction of dislocations in the bulk (MD) and are stored in the material by trapping each other in a random way. When reducing the scaling of the microstructure (layer thickness, building block size) the plastic flow is more and more localized and shows a specific flow pattern that is characteristic for the material. Under strong confinement in a specific size regime, almost all of the dislocations that participate in the plastic deformation are confined between the hard/soft interface. For confined crack tip plasticity, in the thickness regime 300 to 1000 nm dislocation activity right at the crack tip leads to the formation of a compact shielding dislocation array, see section 4.3.2. The characteristic dislocation array for thin layers, however, is created by blunting dislocations, i.e. dislocations moving out from the layer material. This shielding array consists of dislocations stored close to crack tip and can be seen as an array of geometrically necessary dislocation that is the most effective dislocation configuration in the sense that it provides a high shielding factor with a small number of dislocations. The dislocation array is a source of long-range internal stresses that increase the stress intensity in front of the initial crack tip and drive cleavage. We found that also other dislocation configurations may exert shielding on the crack tip, however, far more dislocations randomly generated within the bulk are necessary to give the same amount of shielding, see Figure 4.1 a) and b). If the scaling is increased, i.e. for thicker layers, a cluster of shielding dislocations that are generated in the bulk material forms ahead of the initial crack tip. This configuration provides shielding more efficiently than a long single dislocation array interacting with the background plasticity.

The flow pattern that we found in the atomistic analysis of metallic biomorphous nanocomposites for the scaling regime 20 to 160 nm is characterized by the localized slip within the shearing of ductile interlayer, see section 5.8.1. Even though macroscopically a homogeneous tensile deformation is applied, deformation is microscopically non-homogeneous as a consequence of the microstructural heterogeneity. The soft interlayer need to shear simultaneously to allow for a macroscopic homogeneous tensile deformation. The characteristic flow pattern that causes the shearing of the metallic interlayer takes place by dislocations traveling from their nucleation sites at the platelet corners into the Al channel where they interact mainly by the reflection mechanism with the Ni-Al interface. The strength-scaling curve we deduced from our analysis seems to bend over on larger scales ($d > 160\,\mathrm{nm}$) representing another regime with less scale sensitivity, see Appendix 5.14. That means that analogously to the toughness-thickness scaling of confined crack tip plasticity the scaling sensitivity is reduced at larger scales due to a strain hardening behaviorwhen the specific localized flow pattern interacts with the background plasticity from the material volume. The strain hardening effect gives rise to a higher flow stress with increasing density of dislocations.

Furthermore, the transition of the governing deformation mechanism, from extended partial dislocations to full dislocations, with decreasing scaling is recently correlated with a plateau for the strength-scaling relationship (Yamakov et al., 2004). In the case of regularly designed nanocomposites, the strength was nearly constant in the investigated regime where the occurrence of extended partial dislocations was still dominant, see Figure 5.8. However in the case of biomorphous nanocomposites, the transition in the strength-scaling relationship is clearly correlated to the transition from dislocation slip to interface shearing.

In the case studies investigated in this work, the mechanical properties of the hard/soft nanocomposites showed a higher sensitivity to the microstructural scaling within the size regime where the deformation is dominated by a specific flow pattern of localized plasticity. This regime is characterized by intermittent and correlated motion of interacting dislocations, strain proceeds through uncorrelated events of individual dislocation nucleations and propagations. The dislocation mean free path coincides with the characteristic scale of the material, i.e. the layer thickness or the building block size. With increasing scaling, the evolving specific dislocation pattern interact with the background plasticity from the material volume. Plastic deformation is then provided more efficiently by dislocations generated from random sources in the volume material. On the large scale range (thick layers, large building block sizes), the scaling sensitivity changes significantly.

6.5 Strong and tough due to bone-like design?

In this work, we studied the generic design concept of biological materials such as bone or nacre. We focused on a model system for mineralized collagen fibrils where hard Ni platelets play the role of the hydroxyapatite mineral platelets, and where an Al matrix simulates the behavior of the soft organic collagen.

6.5.1 The hard/soft material pairing

In real bone, the ratio of the elastic moduli between hard and soft phase is more than 100 (Jager and Fratzl, 2000). The hard hydroxyapatite phase can considered to be rigid compared to the soft collagen phase. The breaking of sacrificial bonds in real bone allows for a pure shear-tension mode as described by Ji et al. (2004). In our model Ni/Al nanocomposite the mechanical incompatibility is no that significant so that we did not observe the expected decohesion at the platelet front ends. Decohesion was only found under very extreme conditions and only at high plastic strains. Even though the mechanical dissimilarity between Ni and Al is not that significant as in the biological mineral/collagen counterpart, the deformation mode we found is in agreement with experimental findings and corresponds to the theo-

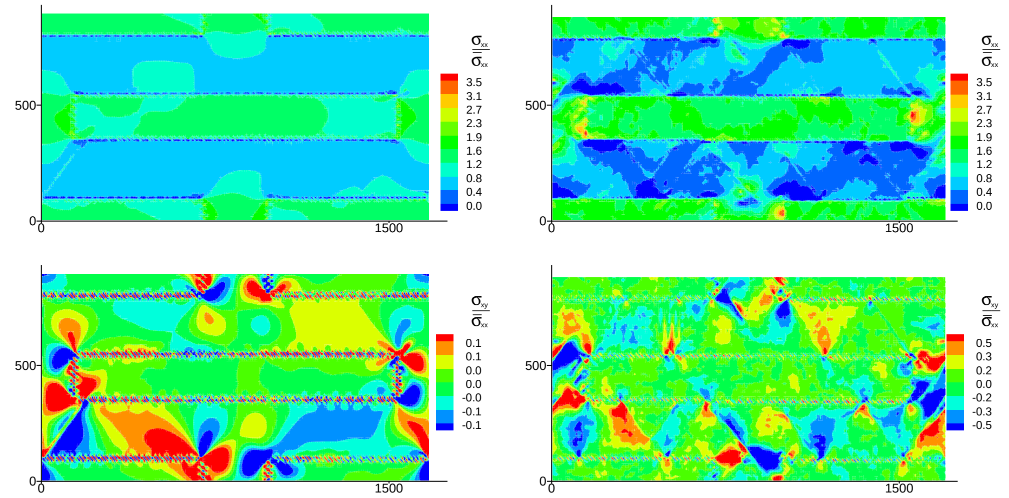

Figure 6.5: Tensile (top) and shear (bottom) stress distribution in the bone-like nanocomposite before (left) and right after (right) the yield point.

retical consideration of the shear-tension load transfer mechanism (Ji et al., 2004). See Figure 6.5(left), macroscopic uniaxial loading $\bar{\sigma}_{xx}$ is transmitted through tensile loading of the platelets and shear loading of the soft matrix. At the macroscopic initial yield point the maximum shear load is reached which the matrix can sustain, Figure 6.5(right). The stress enhancement $\sigma_{xx}^{\text{platelet}}/\bar{\sigma}_{xx}$, i.e. the platelets longitudinal internal stress divided by the applied stress, is about 1.5. For bone under tensile strain, stress enhancement factors of 2.8 are reported in the literature (Almer and Stock, 2005).

6.5.2 The soft phase

It is believed that strength and toughness of the soft matrix become controlling factors for the mechanical performance of bone (Jager and Fratzl, 2000; Gao et al., 2003). We found that since the hard phase is not capable of dissipating much energy, the soft matrix between the hard Ni platelets plays a crucial role by dissipating energy and redistributing high stresses that occur at the platelet corner. In the case of a flawed interface the soft phase provides effective shielding. Even though we found that on large scale interfacial flaws open up to cracks under loading and grow along the interface towards the corners of the platelet, due to efficient shielding the crack simply blunts without propagating further into the Al phase.

6.5.3 The overlapping platelets of large aspect ratio

The amount of mineral is usually thought to determine the stiffness of the fibril. Our simulations suggest that the properties of the the geometrical arrangement of the two components have a larger influence on the properties than traditionally assumed, see Figure 5.6. We found that with increasing grain refinement the fraction of interfacial atoms and hence the fraction of weaker bonds increases, see Figure 5.12. One may speculate that the larger the aspect ratio the smaller the interface content that is under tensile load, and hence the smaller the compliance contributed by the interface. The strength of the confined soft matrix was found to control the mechanical performance of the metallic nanocomposite. The overlapping of the platelets is very important in two ways. First, the confinement effect strengthens the yielding soft phase. At large strains, where the platelets are pulled with respect to each other, due to the large aspect ratio the strengthening effect is still maintained so that the flow stress keeps a constant level. Second, the toughening effect under tensile loading in direction of the platelets is great when the aspect ratio is high since large amounts of energy can be absorbed by successive plastic shearing of the metallic interlayer and finally interfacial shearing after saturation of dislocation activity.

6.5.4 The nanoscale

It has been reported (Jager and Fratzl, 2000; Gao et al., 2003) that the overall mechanical performance of the fibril depends crucially on the shear properties of the organic matrix. The small dimensions (a few nanometers) of both, the mineral particles and the organic layers between them, were proposed to be essential to ensure the mechanical performance of the tissue (Jager and Fratzl, 2000; Gao et al., 2003). We tested the effect of the scaling on both strength and flaw tolerance of the metallic nanocomposite. Notably, we find for the bio-inspired design the maximum strength (highest level of flow stress) and flaw tolerance (flow stress invariance with respect to flaws) is achieved at the same length scale (50 nm).

6.6 Critical view on the models

6.6.1 Applicability of the numerical tools

The computational burden of mesoscopic DD simulations is oftentimes underestimated even in the two dimensional case compared to atomistic simulations. Clearly, both tools address different time and length scales. The underlying theory of the mesoscopic model is linear elasticity. Introducing image forces due to the two extreme cases of free surfaces or fully constrained boundaries already causes extra computational burden, however, the problem remains linear. The computational time required for the analysis of interface controlled plasticity problems increases drastically because the combined DD/CZ model involves complex boundary conditions. The complexity comes from the non-linear constitutive law of the cohesive zone model that is introduced when crack growth or interface shearing and opening is considered. The constitutive relationships for the atomistic simulation specifying the interaction between the atoms are intrinsically non-linear. The presence of interfaces is therefore irrelevant for the computational time involved.

The setup of an efficient combined DD/CZ model is characterized by the compromise between numerical accuracy and computational time. Practically, the accuracy should be measured based on the macroscopic mechanical property that is the ultimate output of the analysis. However, it must be noted that the necessary discretization refinement of the cohesive zone is also related to the considered parameter range of the cohesive zone model. The application of the mesoscopic model to a new problem requires a phase of preliminary testing in order to develop a robust algorithm. This is generally the case when the analysis evolves numerical integration, however, particulary important in a crack growth analysis. The numerical resolution of crack advance is strongly related to the activation of sources, dislocation slip, and hence, to the computed fracture toughness. In consequence, the application of mesoscopic tools is less flexible.

6.6.2 Physical description of the deformation mechanisms

The geometric restriction due to the plane strain approximation in the atomistic model restricts in-plane plastic deformation in the soft Al phase to the nucleation and motion of 60° dislocations. Dislocation nucleation and motion are both affected by this restriction. In the quasi two-dimensional model stacking faults can be generated more easily compared to the situation within a three dimensional structure. Even though aluminium has a high stacking fault energy compared to other fcc metals, our model material for the soft phase corresponds rather to a metal with low stacking fault energy. Furthermore it should be noted that in fully three dimensional structures the nucleation of dislocations from interfaces depends on the scaling, i.e.

there is a scaling dependence of the threshold stress to nucleate a dislocation from the interface. This relation is not represented in the atomistic model. However, the macroscopic strength that we deduce from out atomistic model is related to the flow stress at large plastic strains which is determined by the confinement effect on dislocation motion and not by the dislocation nucleation process.

6.7 Outlook

The DD/CZ model presented in this paper will be employed to understand the competition between crack growth and dislocation nucleation for a crack that may atomically blunt during dislocation formation. Surprisingly, on the dislocation dynamics scale the effect of crack tip blunting has only been addressed secondarily. The results from the sharp crack tip model assesses the impact of finite crack tip blunting for the competition of crack reinitiation versus dislocation nucleation. Ultimately we will attenuate the role of near interfaces for this competition. Is the discrepancies between DD simulations and experimental results regarding the order of the characteristic length scale caused by the neglect of shape change of the crack tip?

Especially mesoscopic approaches have great potential in validating continuum methods based on strain gradient theories and can help to put continuum theories on a more physically solid basic. We did not evaluate the dislocation distribution with respect to volumes containing net Burgers vector in our atomistic simulations as we did not expect high strain gradients near the weak interfaces. However, geometrically necessary dislocations with respect to long-range internal stresses in the sense of Mughrabi (2006) seem only to play a role in the regime above 160 nm. In future we will try to access the scaling behavior in the large scale regime by a discrete dislocation model of hard/soft composite to model the symmetrical multiple slip in the soft phases and to identify the formation of net Burgers vectors in the interface regions. See the simulated dislocation microstructure in Figure 6.6 (right), the stresses are rather high within the platelets due to the occurrence of superdislocations at the interfaces. The bio-inspired design concept for strong and tough material investigated here for the first time provides a solid basis to extend future research in the following steps. (I) Based on the results obtained for the atomistic model that was fully described through EAM potentials, we can now start to make reasonable approximations to reduce the computational costs: since the platelets do not deform plastically, they can be modeled by simple biharmonic potentials. Such a model would allow studying the effect of elastic mismatch by varying the stiffness of the platelets. Computational costs could be reduced significantly by modeling the platelets simply as rigid solids, a reasonable assumption considering real bone tissue. (II) Several questions can be asked from a physical point of view. Does the deformation mode or the deformation mechanisms change when the platelets are discontinuous in all directions as in bone? What is the meaning of interface shearing in this case? Furthermore, what is the influence of the crystal orientation? Do we still see the strong scaling dependence when the slip planes are aligned parallel to the platelets? (III) The research potential of this material is also fascinating considering engineering aspects. In order to investigate the effect of interface strength on the mechanical performance we plan to employ a simple Lennard-Jones potential for the interface description that would introduce controlling parameters for the interface strength.(IV) Eventually one may think of using a gel-like material for the soft phase that mimics collagen more realistically. Such a highly viscous polymer would introduce a strong loading rate sensitivity. At low loading rates, due to confinement

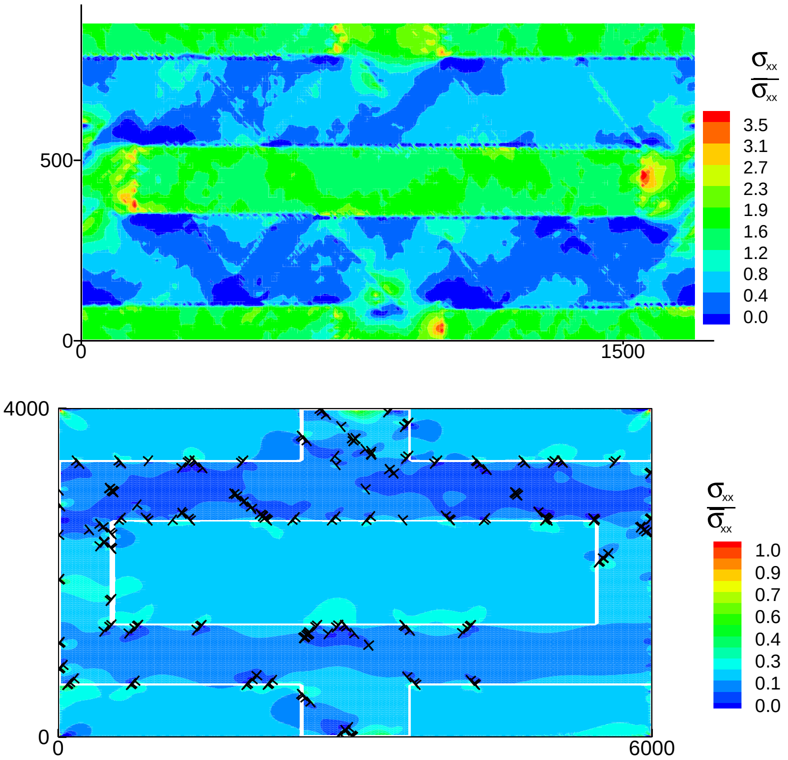

Figure 6.6: Tensile stress redistribution in the biomorphous metallic nanocomposite on the atomistic scale (top; scale is in Å) and on the mesoscopic scale (bottom, scale is in nm)

the fluid-like material would still maintain its mechanical integrity and respond as a soft deformable solid. Under very high loading rates, however, it would respond ultra-hard.

7 Conclusions

7.1 Mesoscopic modeling

This works presents an combined two dimensional dislocation dynamics (DD) - cohesive zone (CZ) model to analyze the dynamics of discrete dislocation (DD) problems in two dimensions accounting for the interaction of cohesive boundaries, interfaces and cracks with a dislocation microstructure. The underlying boundary value problem of dislocations in a finite elastic medium is solved with a Greens function approach. Frank-Read like sources are distributed homogenously in the plastic layer containing two slip systems. A cohesive zone model of trapezoidal shape is implemented to describe crack propagation. It needs fracture energy and maximum tensile strength of the interface as input parameters (Broedling et al., 2006).

The combined DD/CZ is a valuable tool for understanding the complex interplay of dislocation plasticity with small-scale boundary conditions which interact to control fracture and deformation in nano- and microstructured metallic composites. The Green's function approach is, though not very flexible in it its application, a computationally efficient method to consider nano scaled structures such as sharp and blunt crack tips as well as bulk behavior of nanocomposites. The focus on the numerical parameters involved in DD/CZ modelling yields that the influence of the random source distribution can give rise to statistical fluctuation in the fracture toughness of about 5-10% without changing significant trends in other parameters. The variation of the shape of the traction-separation law leaves results unchanged within 5%.

7.2 Confined crack tip plasticity

The two dimensional combined DD/CZ model is employed to study the fracture mechanism of a layered composite material. Frank-Read like dislocation sources are distributed homogenously in an elastic-plastic layer sandwiched within elastic regions. The competition between nucleation and motion of shielding dislocations and the crack propagation determines the amount of plastic energy dissipation and thus the fracture toughness. A general result is that fracture toughness scales with the size of the plastic zone. This leads to an embrittlement of the layered structure due to geometrical confinement. However, even in the absence of geometrical confinement it is found that the size of the plastic zone, now determined by the yield strength and the cohesive strength of the material, decides on its bulk fracture toughness (Broedling et al., 2008b).

The results of the numerical model show that fracture of the layered structure undergoes a transition from ideally brittle to bulk behaviour with increasing layer thickness. The critical layer thickness at which the bulk fracture toughness of the elastic-plastic material is reached as well as the bulk fracture toughness itself increase with the cohesive strength of the interface, but become smaller for higher yield strengths. Fracture toughness as a function of layer thickness saturates gradually if dislocation activity is dispersed, dilute and not compact around the crack tip and increases abruptly within the layer thickness range of 300 to 1000 nm when dislocation activity right at the crack tip is possible and a compact array of shielding dislocations forms near the crack tip. While the slip localization is beneficial for the fracture toughness at small layer thicknesses, the bulk fracture toughness is found to be slightly lower compared to a model with a homogeneous source distribution.

Nucleation of dislocations on sources away from the crack tip increases the density of shielding dislocations in front of the crack and thus shields the crack after it starts to propagate. This leads to a jump like crack advance, with periods of crack arrest in regions where groups of dislocations elastically shield the crack from the applied load. While in thicker layers crack growth is thus stable over some distance, crack arrest in very thin layer materials seems to be more difficult. This is caused by the back stress from the dislocation array near the crack tip that adds to the applied load and by the comparatively small density of shielding dislocations in front of the crack tip.

7.3 Size effects in metallic nanocomposites

A bio-inspired design concept of a dual phase hard/soft metallic nanocomposite is investigated on the example of a Ni/Al system under uniaxial loading (Broedling et al., 2008a). The study is restricted to nanocomposites with regular platelet distributions in a quasi-two-dimensional geometry, i.e. the platelets are considered infinitely long in the third direction by virtue of periodic boundary conditions. This quasi-two-dimensional model allows us to study size dependent mechanical properties over a wide range of characteristic length scales under realistic quasi-static loading conditions. The characteristic length scale of the nanocomposite is given by the distribution wavelength of the embedded platelets in loading direction.

The investigations on size dependent plasticity of biomorphous metallic nanocomposites with self-similar nanostructures reveal that dislocation nucleation, dislocation glide, deformation twinning as well as interfacial slip and decohesion occur on all investigated length scales. However, quantifying the contribution of dislocation-based plasticity and interface-mediated interfacial slip as a function of the nanostructural scaling shows clearly that a transition in the dominant deformation mechanism occurs from interfacial sliding at small length scales to dislocation processes at larger length scales. In the structures considered here, this transition takes place at a length scale of 50 nm. Notably, we find a maximum in the calculated flow stress at the same length scale. For larger length scales the geometric constraint on dislocation processes is relieved and the strength of the material decreases steadily. Our simulations show that the strength within the regime of 50-160 nm scales in agreement with the Hall-Petch relation. Below 50 nm, softening occurs due to interfacial sliding as is confirmed by a slip vector analysis.

The presence of interfacial flaws dramatically decreases the strength above a length scale of 80 nm, below this scale the material exhibits a good flaw tolerance. Changes in structural morphology with respect to the platelet distribution and platelets aspect ratio have an influence on the strength of the nanocomposite even at small scales, but only if the mean free path of dislocations is affected. Our simulations indicate that a larger mean free path means a softer material, even if the volume content of hard inclusions is the same.

7.4 Summary of main findings

Dislocation mean free path determines scaling behavior

The scale dependence is related to the dislocation mean free path. In case of localized plastic flow originating at the interfaces, the mean free path is directly related to the scaling of the materials microstructure and gives rise to a high scaling sensitivity. When the plastic flow is taken over from the volume material at larger scale, the dislocation mean free path is a complicated function of the evolving dislocation microstructure which is only indirectly related to the microstructural scaling.

The role of interface sliding

For biomorphous metallic nanocomposites, interface sliding is not a self-containing deformation mode in the sense that it is independent of other deformation mechanisms, it is rather dislocation-assisted. Interface sliding plays a similar role at the nanoscale that geometrical necessary dislocations play at the microscale. Both the formation of geometrical necessary dislocations and interface sliding are essential to accommodate the inhomogeneous plastic deformation in hard/soft composites. However, where the strength increases due to the presence of geometrical necessary dislocations on the microscale, the presence of interface sliding at the nanoscale leads to dramatic reduction in strength with decreasing scale.

Interface properties determine the limits of strength

This general conclusion is drawn from a continuum point of view. The interfaces in metallic nanocomposites are sources of strain gradients due to the dissimilar yield strengths of soft and hard phases. The magnitude of the strain gradients depend on the microstructural scaling. The smaller the scaling the higher the strain gradient in order to accommodate the local deformation. At the limit of ultra confinement the strain gradients become very large. The plastic strain distribution appears to be discrete. On this scale the mechanical behavior is totally determined by the tangential interface strength. Can the interface sustain the high stresses associated with the steep strain gradient? If the interface is strong, the ductility of a soft volume material may cease causing embrittlement due to confinement (Broedling et al., 2008b). In the other limit of a weak interface, a strong composite becomes soft (Broedling et al., 2008a).

8 Zusammenfassung (in German)

8.1 Einleitung

Grenzflächenbestimmte Materialsysteme, wie z.B. Schichtmaterialien oder nanokristalline Materialien, sind aufgrund geometrischer Einengung der Plastizität durch Längenskalen-abhängige Materialeigenschaften gekennzeichnet. Verformung und Versagen sind bestimmt durch die Eigenschaften der Grenzflächen und durch Größeneffekte auf die vorherrschenden Verformungsmechanismen. Die vorliegende Arbeit setzt sich zum Ziel, durch Modellbildung und Simulation Größeneffekte und skalenabhängige Materialeigenschaften von nanostrukturierten, zweiphasigen Kompositmaterialen auf der atomaren und mesoskopischen Skala aufzuklären.

Die zwei untersuchten Materialsysteme sind von großem technischem und wissenschaftlichem Interesse. Dünne Schichtmaterialien werden in großer Breite in mikroelektronischen Bauteilen eingesetzt. Forschungsgegenstand war bisher die plastische Verformung in solch eingeengten Systemen. Aber eine genaue Betrachtung des Bruchversagens und der Delamination unter geometrischer Einengung der plastischen Zone fehlt bisher in der Literatur. Die Möglichkeit der Versetzungsentstehung in der Rissspitzenumgebung ist für das Verformungsverhalten, für die Abschirmung des Risses und somit für die Vermeidung von Sprödbruchversagen äußerst wichtig. Im Rahmen dieser Arbeit wurde ein mikromechanisches Modell entwickelt, mit dem das Spaltbruchversagen eines zweiphasigen Schichtmaterials unter Berücksichtigung der kollektiven Versetzungsbewegung in der Nähe einer fortschreitenden Rissspitze simuliert werden kann.

Das zweite Materialsystem stammt aus dem Gebiet der biomimetischen Werkstoffentwicklung und der Grenzflächentechnik. Strukturverfeinerung als ein wichtiger Härtungsmechanismus ist eng verknüpft mit der Behinderung des Versetzungsgleitens durch Grenzflächen während der Verformung. Gemäß theoretischen Überlegungen muss es jedoch auf der Nanoskala eine Grenze für die maximal erreichbare Festigkeit geben. Diese untere Grenze ist durch den Wechsel des vorherrschenden

Verformungsmechanismus festgelegt. Viele natürlich vorkommende Nanokomposite, wie z.B. Spinnenseide oder Perlmutt, sind Vorbilder für feste und gleichzeitig zähe Materialen aufgrund einer besonderen Nanostrukturierung. Die überragenden Eigenschaften beruhen auf einem parallel ausgerichteten Aufbau der Mikrostruktur. In dieser Arbeit wurde ein bio-inspiriertes Materialkonzept für extrem harte und gleichzeitig zähe Materialien getestet. Die Untersuchungen liefern erste grundlegende Erkenntnisse über die entscheidenden Verformungsmechanismen und die kritische Längenskala, die die Festigkeit des Pendants eines biomimetischen Metall-Nanokomposits bestimmen.

8.2 Methoden

8.2.1 Mesoskopische Modelle für Kleinbereichsplastizität

In der vorliegenden Arbeit wird ein gekoppeltes Kohäsivzonen-/ Versetzungsdynamikmodel für 2D Probleme der Kleinbereichsplastizität entwickelt (Broedling et al., 2006). Das mikromechanische Modell berücksichtigt die Wechselwirkung einer Versetzungsmikrostruktur mit Grenzflächen oder einem Riss. Die Auswertung der Peach-Koehler Kraft führt auf ein Versetzungsrandwertproblem, bei dem die Versetzungs-Grenzflächen-Wechselwirkung mit Hife des Superpositionsprinzips der linearen Elastizitätstheorie abgespalten wird, siehe hierzu Abbildung 3.5. Die numerische Lösung des dem Modell zugrunde liegenden Versetzungsrandwertproblems erfolgt über einen Ansatz mit Greenschen Funktionen. Die Versetzungsplastizität ist durch die Nukleation von Stufenversetzungen an Frank-Read-artigen Quellen und deren Bewegung auf zwei Gleitsystemen beschrieben, siehe Abbildung 8.1. Der Rissfortschritt ist durch ein Kohäsivzonenmodell erfasst, das durch Zugfestigkeit und Bruchenergie als Eingangsparameter spezifiziert wird. Das mikromechanische Modell wird anschließend erweitert, um einerseits Rissspitzenfelder an stumpfen Rissen numerisch zu modellieren sowie andererseits das Volumenverhalten von zweiphasigen Metallmatrix-Verbundwerkstoffen unter Berücksichtigung innerer Grenzflächen beschreiben zu können.

Bruchversagen duktiler Schichten

Das 2D Modell beschreibt die Prozesszone in der Nähe der Rissspitze eines Modus I belasteten Risses unter Annahme eines ebenen Verzerrungszustandes und unter Ausnutzung der Spiegelsymmetrie des Problems. Dabei wird die Rissspitze als

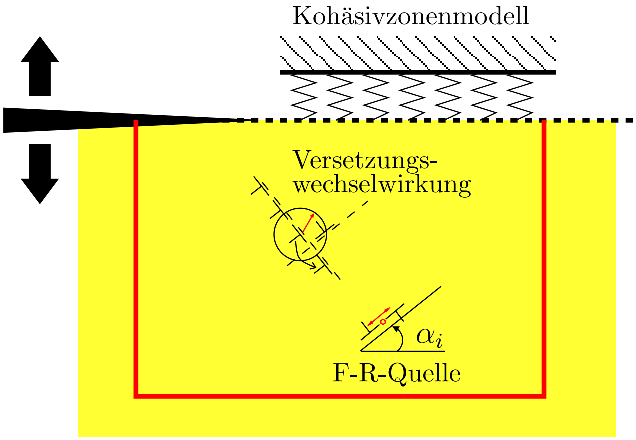

Abbildung 8.1: Schematische Darstellung des gekoppelten Kohäsivzonen-/ Versetzungsdynamikmodels zur Beschreibung eines Modus I belasteten Risses.

der Nahbereich eines viel längeren endlichen Risses betrachtet, siehe Abbildung 8.1. Die Abbildung zeigt lediglich die rechte Rissspitze mit der Kohäsivzone, die durch eine Spannungs-Rissöffnungs-Beziehung (TS-law) charakterisiert ist. Die Auswertung der Peach-Koehler-Kraft führt auf ein reines Spannungsrandwertproblem für einen halb-unendlichen Raum, das mit der Methode der virtuellen Versetzungen gelöst wird (Hills et al., 1996). Die numerische Integration des sich daraus ergebenen Systems aus Randintegralgleichungen erfolgt mit der Kollokationsmethode.

Als Anfangsbedingung für die Simulationen wird ein versetzungs- und spannungsfreies Material angenommen. Die Spannungsintensität wird mit einer konstanten Rate inkrementell erhöht. Der Simulationsalgorithmus beinhaltet neben der Versetzungsmultiplikation (Frank-Read-Quellmechanismus), der zeitlichen Integration der Versetzungsbewegung (Annahme eines viskosen Versetzungsgleitens) und der Erfassung elementarer, kurzreichweitiger Versetzungswechselwirkungen (Versetzungsblokade, Dissoziation) auch die numerische Auswertung der Peach-Koehler-Kraft unter Berücksichtigung der langreichweitigen Versetzungs-Kohäsivzonenwechselwirkung. In dieser Arbeit wird ein trapezförmiges Kohäsivzonenmodell (Tvergaard and Hutchinson, 1993) implementiert, wodurch eine nicht-lineare Materialantwort induziert wird. Die Lösung des Versetzungsrandwertproblems erfolgt iterativ durch ein semi-implizites Prediktor-Korrektorverfahren und Linearisierung des Kohäsivzonengesetzes, siehe hierzu das Flussdiagram in Abbildung 3.2. Dieses Vorgehen ergibt sich aus der zeitlichen Auflösung der Versetzungsprozesse, die einen sehr kleinen Zeitschritt erfordert. Der effektive Abschirmungsintensitätsfaktor der Rissspitze ergibt sich aus der Differenz der lokalen und globalen Spannungsintensitätsfaktoren. Diese werden numerisch durch Auswerten des J-Integrals berechnet, siehe hierzu Abbildung 3.7.

Modell für stumpfe Rissspitzen

Das mesoskopische Modell für stumpfe Rissspitzen ist motiviert durch die Diskrepanz zwischen Simulationsergebnissen aus Versetzungsdynamikmodellen und Ergebnissen aus Experimenten in Bezug auf die Größenordnung der charakteristischen Längenskala, auf denen eine Wechselwirkung zwischen Rissspitze und Grenzfläche beobachtet wird (Vehoff, 2007). Die unterschiedlichen Größenordnungen können auf die Annahme eines scharfen Risses in DD Simulationen zurückgeführt werden, wodurch die plastische Zone lokal auf einen kleinen Bereich an der Rissspitze begrenzt bleibt.
In dem Modell für stumpfe Risse wird ein mit einem fokussierten Ionenstrahl erzeugter Anriss als halbkreisförmige Rissspitzengeometrie modelliert. Das diesem Modell zugrunde liegende Randwertproblem ist für ein endliches, die Rissspitze umfassendes Gebiet formuliert, siehe hierzu Abbildung 3.11. Für die numerische Integration der Randintegralgleichungen werden Randelemente auf Basis von Verschiebungsdiskontinuitäten verwendet. Dieses Vorgehen hat gegenüber der Methode der virtuellen Versetzungen den Vorteil, dass bei geknickten Rissen keine zusätzlichen Übergangsbedingungen implementiert werden müssen, siehe (Hills et al., 1996). Im Modell für stumpfe Risse wird die äußere Belastung durch geeignete Verschiebungsrandbedingungen entsprechend eines im Modus I belasteten Risses auf Randsegmenten weit weg von der Rissspitze simuliert.

Verformung von Metallmatrix-Verbundwerkstoffen

In der Literatur sind Versetzungsdynamik-Simulationen nur für kristalline Volumenmaterialien oder Nanokomposite mit kohärenten Grenzflächen beschrieben worden. Die Grenzflächen waren dabei entweder durch ihre diskontinuerlich veränderlichen elastischen Eigenschaften (Cleveringa and Van der Giessen, 1999; Cleveringa et al., 1997) und/oder als für Versetzungen undurchdringlich modelliert worden (Cleveringa and Van der Giessen, 1999; Cleveringa et al., 1997; Biner and Morris, 2003, 2002). Atomistische Simulationen zeigen jedoch, dass die Grenzflächeneigenschaften in grob strukturierten Kompositen einen großen Einfluss auf die makroskopischen mechanischen Eigenschaften haben. Zum Beispiel können schon kleinste Grenzflächenanrisse die Festigkeit eines grob strukturierten Metallmatrix-Komposits extrem verringern (Broedling et al., 2008a).

Das Ziel in dieser Arbeit ist die Entwicklung eines Simulationswerkzeugs für die

Untersuchung des Volumenverhaltens von Metallmatrix-Kompositwerkstoffen mit Auflösung der mikroskaligen Versetzungsprozesse und des Grenzflächengleitens. Die wesentlichen Änderungen bestehen in der Implementierung einer periodischen Simulationszelle zur Beschreibung der Volumenverformung eines representativen Volumenelementes (RVE), siehe Abbildung 3.18 und Abbildung 3.19. In dem Modell wird die äußere Belastung durch eine im makroskopischen Sinne homogene Dehnung aufgebracht. In der Implementierung der Periodizitätsforderung sind alle makroskopischen Größen - auch die äußere Belastung - als Mittelwerte der lokalen mechanischen Felder definiert. Die mechanischen Felder (Spannungen und Verschiebungen) können auf dem Rand der Simulationszelle um diese Mittelwerte fluktuieren.

8.2.2 Atomistisches Modell für metallische Nanokomposite

Einen weiteren Schwerpunkt in der vorliegenden Arbeit bildet der Einsatz großskaliger Molekulardynamik zur Simulation zweiphasiger metallischer Nanokomposite mit einer nanoskaligen Strukturmorphologie ähnlich der in biologischen Nanokompositen (Knochen, Perlmutt), siehe Abbildung 5.1. Hierbei steht die Analyse der vorherrschenden Verformungsmechanismen im Vordergrund. Das betrachtete atomistische Ni/Al-Modellsystem besteht aus harten, nano-dimensionierten Ni-Plättchen, die in einer Al-Matrix eingebettet sind. Die Untersuchungen sind beschränkt auf Nanokomposite mit gleichmäßig verteilten Plättchenanordnungen in quasi-zweidimensionalen Strukturen, d.h. die Plättchen werden in der dritten Raumrichtung als unendlich ausgedehnt betrachtet. Durch die Reduktion der Dimension ist es möglich, die Simulationen unter realistischen quasi-statischen Belastungsbedingungen durchzuführen und so dynamische Effekte aufgrund von hohen Belastungsraten zu vermeiden. Die simulierten $[\bar{1}10]$ texturierten kolumnaren Nanostrukturen bestehen aus zwei Komponenten (Ni und Al) mit der gleichen kristallographischen Orientierung. Die Orientierung und die aufgebrachten periodischen Randbedingungen erlauben Versetzungsnukleation und Versetzungsbewegung auf effektiv nur zwei, zur Belastungsrichtung ±60° geneigten Gleitsystemen, siehe Abbildung 5.1.

Die mechanischen Eigenschaften werden mit dem am Institut für theoretische und angewandte Physik, Universität Stuttgart, entwickelten, parallelen Molekulardynamik-Code “IMD“ berechnet (Stadler et al., 1997). Zur Simulation einer einachsigen, quasi-statischen Zugbelastung werden geringfügige Modifikationen an dem Code vorgenommen. Die Beschreibung der interatomaren Wechselwirkung wird mit einem embedded atom (EAM) Wechselwirkungsmodell (Ludwig and Gumbsch, 1995) realisiert. Dieses Modell eignet sich belegterweise gut für eine realistische Beschreibung der interatomaren Kräfte entlang von Ni/Al Grenzflächen. Zur Identifizierung der Nukleation und Bewegung von Defekten werden in dieser Arbeit die *common neighbour analysis* (CNA) und die Gleitvektor-Analyse eingesetzt. Die Berechnung des Gleitvektors folgt dem Vorschlag von Zimmerman et al. (2002). Während die CNA verwendet wird, um Atompaare hinsichtlich ihrer lokalen Umgebung zu klassifizieren und dadurch Versetzungskerne, Stapelfehler und andere Defekte der kristallinen Struktur nachweisen zu können, wird der Gleitvektor als Maß verwendet, um das Auftreten von Gleitmechanismen sowohl in den duktilen Komponenten als auch in den Grenzflächen zu quantifizieren.

8.3 Ergebnisse und Diskussion

8.3.1 Skalenabhängige Bruchzähigkeit dünner Schichten

Einfluss der mikrostrukturellen Umgebung an der Rissspitze

Es werden sowohl der Einfluss der lokalen Quellverteilung als auch die Quellverteilungsdichte untersucht. Für dünne Schichtmaterialien mit einer Schichtdicke unter 300 nm ist das Bruchverhalten durch die lokale Quellverteilung selbst und nicht mehr durch deren Dichte kontrolliert. Deswegen wird angenommen, dass in diesem Größenbereich die Möglichkeit der Versetzungsnukleation direkt an der Rissspitze das Bruchverhalten dominiert und der Einfluss von Volumenquellen vernachlässigbar ist, siehe Abbildung 4.1. In den vier Simulationen eines $1\,\mu$m dicken Schichtmaterials werden für das Volumenmaterial unterschiedliche Quelldichten angenommen. Zusätzlich wird für die Materialien in Abbildung 4.1 b), c) und d) eine Rissspitzenquelle nahe der Rissspitze berücksichtigt, siehe Abbildung 4.1 a) und b). Für das Skalierungsverhalten ergibt sich, dass die Bruchzähigkeit dünner Schichten ($h < 1000\,\text{nm}$) durch die Versetzungsnukleation direkt an der Rissspitze kontrolliert wird, siehe Abbildung 8.2. Der Einfluss der Volumenquellen zeigt sich nur für dicke Schichten ($h > 1000\,\text{nm}$) durch eine Änderung der Bruchzähigkeit des Volumenmaterials, die das Material im Grenzfall sehr dicker Schichten erreicht.

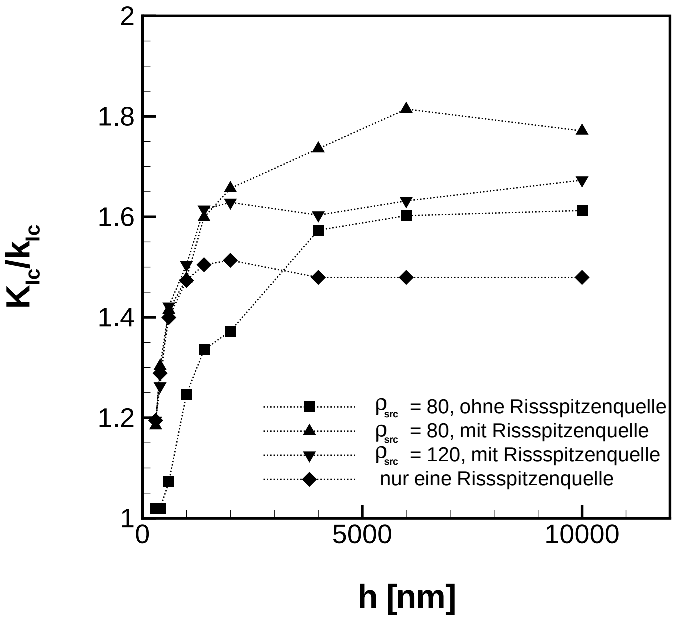

Abbildung 8.2: Normierte Bruchzähigkeit als Funktion der Schichtdicke für vier verschiedene Quellverteilungen, siehe auch Abbildung 4.1.

Einfluss der intrinsischen Materialeigenschaften

Die Bruchzähigkeit als Funktion der Schichtdicke geht graduell in eine Sättigung über, wenn die Versetzungsprozesse an der Rissspitze breit verteilt sind. Sie steigt jedoch im Bereich 300 – 1000 nm sprunghaft an, wenn an der Rissspitze lokalisierte Gleitprozesse möglich sind und eine kompakte Versetzungsreihe von abschirmenden Versetzungen gebildet werden kann. Die numerischen Simulationen zeigen, dass das analytische “Superversetzungsmodel“ von Hsia et al. (1994) den Abschirmungseffekt lokal an der Rissspitze auftretender Gleitprozesse unterschätzt und den daraus resultierenden sprunghaften Anstieg der Bruchzähigkeit nicht abbildet. Im Fall von lokal an der Rissspitze auftretenden Gleitprozessen kann das Skalierungsverhalten durch die Bruchzähigkeit des Volumenmaterials und durch die kritische Schichtdicke beschrieben werden, bei der die Bruchzähigkeit des Schichtmaterials 95% der Bruchzähigkeit des Volumenmaterials erreicht (Broedling et al., 2008b). Die numerischen Ergebnisse machen den starken Einfluss der kohäsiven Festigkeit, der intrinsischen Bruchzähigkeit und auch der Fließfestigkeit auf das Skalierungsverhalten deutlich, siehe Abbildung 8.3. Unter anderem zeigt sich, dass bei einer Verdopplung der kohäsiven Festigkeit die Bruchzähigkeit des Volumenmaterials um 10% und die kritische Schichtdicke um 20% ansteigt. Einen großen Einfluss hat auch die intrinsische Fließfestigkeit des Volumenmaterials. Wenn beispielsweise die Versetzungsnukleation durch eine Verdopplung der Fließfestigkeit erschwert wird, fällt die Bruchzähigkeit des Volumenmaterials um 20% ab und die kritische Schichtdicke

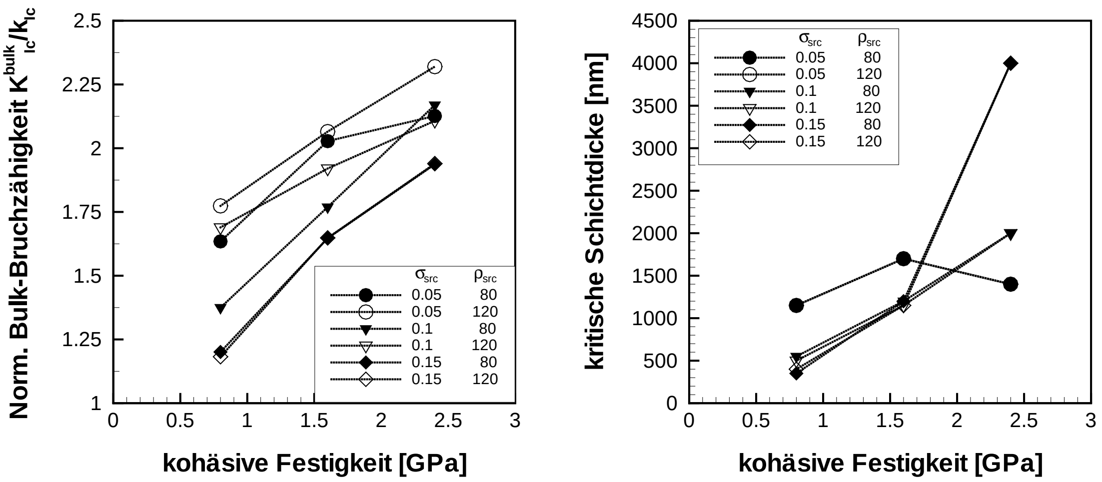

Abbildung 8.3: Bruchzähigkeit des Volumenmaterials (a)) und kritische Schichtdicke (b)) als Funktion der kohäsiven Festigkeit für unterschiedliche Fließfestigkeiten. Kurven entsprechen zwei Quelldichten $\rho_{src} = 80\,(\mu\text{m})^{-2}$ (gefüllte Symbole), $\rho_{src} = 120\,(\mu\text{m})^{-2}$ (offene Symbole) und drei unterschiedlichen Fließfestigkeiten $\sigma_{src} = 0.05\,\text{GPa}$, $0.1\,\text{GPa}$ und $0.15\,\text{GPa}$.

um sogar 80%. Weiterhin zeigen die numerischen Untersuchungen, dass in dickeren Schichten ein instabil fortschreitender Riss zum Stillstand kommen kann, wenn die Rissspitze auf eine Versetzungsquelle trifft, die in kurzer Zeit eine Reihe von Versetzungen mit stark abschirmendem Charakter emittieren kann. Dieses Verhalten wurde für Volumenmaterialien auch von Cleveringa et al. (2000) beschrieben. In sehr dünnen Schichten kann man jedoch davon ausgehen, dass dieses Verhalten nicht auftritt, da sich zeigt, dass durch den emittierten primären Versetzungsaufstau eine hohe Spannungsintensität vor der Rissspitze induziert wird, die die auf den Riss wirkende treibende Kraft stark erhöht (Broedling et al., 2008b).

8.3.2 Größeneffekte in bioinspirierten Metall-Nanokompositen

Die charakteristische Längenskala des bio-inspirierten metallischen Nanokomposits ist durch die Verteilungswellenlänge d (building block size) der eingebetteten Plättchen gegeben. Die Untersuchung der skalenabhängigen Verformungsmechanismen und Materialeigenschaften erfolgt anhand von neun selbstähnlichen Nanostrukturen, siehe Tabelle 8.1.

Die Festigkeit des Materials wird in Analogie zu Schiøtz and Jacobsen (2003) als die mittlere Fließspannung im Intervall [6%; 8%] der Gesamtdehnung definiert.

Tabelle 8.1: Verwendete Kennzeichnung des Skalierungsparamters d (building block size), entspricht der Verteilungswellenlänge der eingebetten Plättchen in Belastungsrichtung.

	NC01	NC02	NC03	NC04	NC05	NC06	NC07	NC08	NC09
d [nm]	10,3	15,3	20,6	30,9	41,0	61,5	82,5	163,5	330,2

Grenzflächendefekte und Strukturmorphologie

Für die Skalierung NC07 zeigt das Aspektverhältniss der Plättchen keinen wesentlichen Einfluss auf die Steifigkeit, siehe Abbildung 5.5. Steifigkeit und Festigkeit zeigen sich jedoch sehr empfindlich gegenüber Änderungen des Volumenanteils der verstärkenden Ni-Phase. Für einen engen Plättchenabstand wird darüberhinaus eine bei höheren Dehnungen einsetzende Delamination der Ni/Al Grenzfläche an den Stirnseiten der Plättchen beobachtet. Die Beobachtung der Grenzflächendelamination in einem Nanokomposit mit duktilen Komponenten bringt die Frage auf, ob dieser Schädigungsmechanismus skalenabhängig ist und wie der Schädigungsverlauf von der Strukturskalierung abhängt. Für die biomorphe Struktur wird deshalb der Einfluss der durch einen engen Plättchenabstand hervorgerufenen Delamination sowie der Einfluss von vorhandenen Grenzflächenanrissen auf die makroskopische Festigkeit des Materials auf verschiedenen Skalen eingehend analysiert. Die Festigkeit des fehlerbehafteten Nanokomposits zeigt sich dabei stark skalenabhängig. Während die verstärkende Wirkung der Plättchen bei einer groben Skalierung von NC08 vollkommen verloren geht, wird die Festigkeit des Materials bei einer feinen Skalierung von NC05 nicht wesentlich beeinträchtigt.

Skalenabhängige Verformungsmechanismen

Ein wichtiges Ziel dieser Arbeit ist es, die Rolle des Grenzflächengleitens und der Versetzungsplastizität quantitativ zu untersuchen. Dazu wird über den gesamten Dehnungsbereich $[0; 8\%]$ der Gleitvektor nach Zimmerman et al. (2002) ausgewertet. Für die Analyse der skalenabhängigen Verformungsmechanismen in der duktilen Phase sowie in der Grenzfläche werden die CNA und die Gleitvektoranalyse eingesetzt. Versetzungsgleiten, mechanische Zwillingsbildung sowie Grenzflächengleiten und Dekohäsion konnten auf allen betrachteten Längenskalen beobachtet werden. Die in Abhängigkeit von der Längenskala dominierenden Verformungsmechanismen sind in Tabelle 5.2 zusammengetragen.

Die hier beobachteten Wechselwirkungen zwischen Versetzungen und Grenzflächen unterscheiden sich grundlegend von denen sonst von einphasigen nanokristallinen Metallen bekannten. Dort werden die Versetzungen vornehmlich von den Korngrenzen absorbiert (Schiøtz et al., 1999; Schiøtz and Tolla, 1998; Swygenhoven et al., 2002). In den hier untersuchten Strukturen bewegen sich die Versetzungen von ihren Nukleationsquellen an den Stirnseiten der Plättchen hinein in die Al-Kanäle, wo sie durch Reflexion, in seltenen Fällen auch durch Transmission, mit den Grenzflächen wechselwirken. Dieser Mechanismus ist auch in anderen atomistischen Simulationen von Cu-Ni Schichtsystemen bekannt und als "*rebound*"-Mechanismus bezeichnet worden (Henager Jr. and Hoagland, 2004; Shen, 2003; Shen and Leger, 2006). Shen (2003) und kürzlich Shen und Leger (2006) haben den Einfluss der Scherfestigkeit der Grenzfläche auf diesen Mechanismus beschrieben. Die Scherfestigkeit der Grenzfläche scheint also in zweiphasigen (hart/weich) Metall-Nanokompositen einen starken Einfluss auf das plastische Fließen und somit auch auf die makroskopischen Materialeigenschaften zu haben.

Korrelation von Materialfestigkeit und Grenzflächengleiten

Die Skalierung der Nanostruktur hat einen starken Einfluss auf die Festigkeit des biomorphen Nanokomposits (Broedling et al., 2008a). Als Maß für die individuellen Gleitanteile der Versetzungsaktivitäten in Matrix, Plättchen sowie des Grenzflächengleitens ist der akkumulierte, anteilige Gleitvektor eingeführt worden (siehe Abschnitt 5.2). In Abbildung 8.4 ist die skalenabhängige Materialfestigkeit zusammen mit dem Anteil des Grenzflächengleitens aufgetragen. Die Festigkeit des biomorphen Materials erreicht ihren Maximalwert bei einer Skalierung von 50 nm. Diese Skalierung stellt eine kritische Längenskala zwischen zwei Bereichen dar, der eine dominiert durch Grenzflächen- und der andere durch Versetzungsgleiten. Die abgeleiteten Werte für die Hall-Petch-Konstante sind zwar überschätzt, sie entsprechen jedoch ihrer Größenordnung nach experimentellen Befunden (Hansen, 2005). Durch die geometrischen Restriktionen des Modellsystems sowie der betrachteten Temperatur von $0\,K$ wird jedoch die Hintergrund-Spannung σ_0 von dem atomistischen Modell um mehrere Größenordnungen überschätzt.

Bewertung des Ni-Al-Modellsystems

In dem Modellsystem für Metall-Nanokomposite mit knochenähnlicher Nanostruktur übernehmen die Ni-Plättchen die Rolle des harten Hydroxylapatit, während die Al-Phase die weiche, organische Kollagen-Matrix simuliert. Obwohl die mechani-

schen Eigenschaften der gewählten Komponenten bei weitem nicht so signifikant verschieden sind wie in dem biologischen Vorbild (Jager and Fratzl, 2000), entspricht dennoch der für das im Metallmatrix-Nanokomposit gefundene *shear-tension*-Verformungsmechanismus dem experimentellen Befund (Jager and Fratzl, 2000) und theoretischen Überlegungen (Ji et al., 2004), (Gao et al., 2003).
(1) Die weiche Al-Phase spielt eine wichtige Rolle für die Umlagerung der Spannungskonzentrationen an den Stirnseiten der Plättchen, für das Abschirmen von vorhandenen Grenzflächenanrissen und kontrolliert somit die mechanischen Eigenschaften des Materials bei großen Strukturskalierungen. (2) Die Überlappung der verstärkenden Plättchen mit großem Aspektverhältnis ist sowohl für die geometrische Einengung der Plastizität gerade bei großen Dehnungen als auch für die Duktilität äußerst wichtig. (3) Die kritische Längenskala für maximale Festigkeit ist nanoskalig und liegt bei d=50 nm. Interessanterweise beginnt darunter auch der Bereich der Fehlertoleranz, in dem die mechanischen Eigenschaften des Materials nicht mehr durch vorhandene Grenzflächenanrisse beinflusst werden.

8.4 Schlussfolgerungen

In der vorliegenden Arbeit wurde der Einfluss geometrischer Einengung auf die Plastizität und auf die mechanischen Eigenschaften zweiphasiger (hart/weich) Nanokomposite untersucht. Aus den numerischen Ergebnissen konnten folgende Schlussfolge-

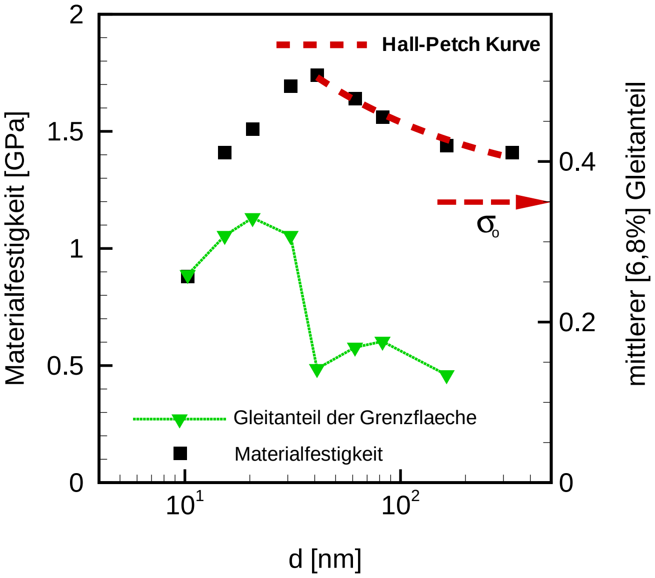

Abbildung 8.4: Skalenabhängige Materialfestigkeit und deren Korrelation mit dem Auftreten von Grenzflächengleiten für das biomorphe Nanokomposit.

rungen gezogen werden:

(I) Die Dickenabhängigkeit der Bruchzähigkeit sehr dünner Metallschichten wird durch die Versetzungsnukleation an der Rissspitze kontrolliert. Bei dickeren Schichten muss zusätzlich die Versetzungsnukleation im Volumen des Schichtmaterials berücksichtigt werden. Die Bruchzähigkeit hängt dann stark von der Fließfestigkeit des Schichtmaterials, der Grenzflächenfestigkeit und von der natürlichen Größe der plastischen Zone ab. Ein Modell mit nur einer Rissspitzenquelle erwieß sich als ausreichend, um die Schichtdickenabhängigkeit der Bruchzähigkeit für sehr dünne Schichten ($h < 1000\,\mathrm{nm}$) abzubilden.Wolf et al. (2005)

(II) In bio-inspirierten Metallmatrix-Nanokompositen ist die große Hall-Petch-artige Festigkeitssteigerung aufgrund von Strukurverfeinerung durch Grenzflächengleiten limitiert. Auf einer kritischen Längenskala wird die Festigkeit des Materials maximal. Dort ist der Effekt geometrischer Einengung auf die Versetzungsbewegung sehr groß und Grenzflächengleiten setzt ein. Die kritische Längenskala wird durch die Scherfestigkeit der Grenzfläche und durch die Fließgrenze der Matrix definiert.

Bibliography

M. P. Allen and D. J. Tildesley. *Computer simulation of liquids.* Clarendon Press. UK, 1996.

J.D. Almer and S.R. Stock. Internal strains and stresses measured in cortical bone via high-energy x-ray diffraction. *Journal of Structural Biology*, 152:14–27, 2005.

E. Arzt. Size effects in materials due to microstructural and dimensional constraints: A comparative review. *Acta Materialia*, 46:5611, 1998.

G. Bao, J.W. Hutchinson, and R.M. McMeeking. Particle reinforcement in ductile matrices against plastic flow and creep. *Acta Metallurgica et Materialia*, 39:1871–1882, 1991.

G.I. Barenblatt. The mathematical theory of equilibrium cracks in brittle fracture. *Advances in Applied Mechanics*, 7:55–129, 1962.

S.B. Biner and J.R. Morris. The effects of grain size and dislocation source density on the strengthening behaviour of polycrystals: a two-dimensional discrete dislocation simulation. *Philosophical Magazine*, 83:3677–3690, 2003.

S.B. Biner and J.R. Morris. A two-dimensional discrete dislocation simulation of the effect of grain size on strengthening behaviour. *Modelling and Simulation in Materials Science and Engineering*, 10:617–635, 2002.

E. Bitzek, P. Koskinen, F. Gahler, M. Moseler, and P. Gumbsch. Structural relaxation made simple. *Physical Review Letters*, 97:170201, 2006.

J.R. Brockenbrough, S. Suresh, and H.A. Wienecke. Deformation of metal matrix composites with continuous fibers-geometrical effects of fiber distribution and shape. *Acta Metallurgica et Materialia*, 39:735–752, 1991.

N.C. Broedling, A. Hartmaier, and H. Gao. A combined dislocation - cohesive zone model for fracture in a confined ductile layer. *International Journal of Fracture*, 140:169–181, 2006.

N.C. Broedling, M.J. Buehler, A. Hartmaier, and H. Gao. The strength limit in a bio-inspired metallic nanocomposite. *Journal of the Mechanics and Physics of Solids*, 56:1086–1104, 2008a.

N.C. Broedling, A. Hartmaier, and H. Gao. Fracture toughness of layered structures: Embrittlement due to confinement of plasticity. *Engineering Fracture Mechanics*, 75:3743–3754, 2008b.

M.J. Buehler, H. Yao, H. Gao, and B. Ji. Cracking and adhesion at small sales: atomistic and continuum studies of flaw tolerant nanostructures. *Modelling and Simulation in Materials Science and Engineering*, 14:799, 2006.

W. Cai, V.V. Bulatob, J.P. Chang, J. Li, and S. Yip. Periodic image effects in dislocation modelling. *Philosophical Magazine*, 83:539–567, 2003.

N. Chandra and P. Dang. Atomistic simulation of grain boundary sliding and migration. *Journal of Materials Science*, 34:655–666, 1999.

N. Chandra, H. Li, C. Shet, and H. Ghonem. Some issues in the application of cohesive zone elements for metal-ceramic interfaces. *International Journal of Solids and Structures*, 39:2817–2855, 2002.

J. Chen, L. Lu, and K. Lu. Hardness and strain rate sensitivity of nanocrystalline cu. *Scripta Materialia*, 54:1913, 2006.

A.S. Clarke and H. Jónsson. Surface step effects on nanoindentation. *Physical Review*, E47:3975, 1993.

H.H.M. Cleveringa and E. Van der Giessen. A discrete dislocation analysis of residual stresses in a composite material. *Philosophical Magazine*, A79:893–920, 1999.

H.H.M. Cleveringa, E. Van der Giessen, and A. Needleman. Comparison of discrete dislocation and continuum plasticity predictions for a composite material. *Acta Materialia*, 45:3163–3179, 1997.

H.H.M. Cleveringa, E. Van der Giessen, and A. Needleman. A discrete dislocation analysis of mode I crack growth. *Journal of the Mechanics and Physics of Solids*, 48:1133–1157, 2000.

S.F. Corbin and D.S. Wilkinson. The influence of particle distribution on the mechanical response of a particulate metal matrix composite. *Acta Metallurgica et Materialia*, 42:1311–1318, 1992.

A.H. Cottrell. *Dislocations and plastic flow in crystals.* Oxford University Press. UK, 1953.

J.D. Currey. Mechanical properties of mother of pearl in tension. *Proceedings of the Royal Society of London*, B196:443, 1977.

M.S. Daw and M.I. Baskes. Embedded-atom method derivation and application to impurities, surfaces, and other defects in metals. *Physical Review*, B29:6443, 1984.

P.M. Derlet and H. Van Swygenhoven. Length scale effects in the simulation of deformation properties of nanocrystalline metals. *Scripta Materialia*, 47:719–714, 2004.

P.M. Derlet, H. Van Swygenhoven, and A. Hasnaoui. Atomistic simulation of dislocation emission in nanosized grain boundaries. *Philosophical Magazine*, 83:3569–3575, 2003.

V.S. Deshpande, A. Needleman, and E. Van der Giessen. Dislocation plasticity modeling of short cracks in single crystals. *Acta Materialia*, 51:1–15, 2003.

D.S. Dugdale. Yielding of steel sheets containing slits. *Journal of the Mechanics and Physics of Solids*, 8:100–108, 1960.

J.D. Eshelby. The force on an elastic singularity. *Philosophical Transactions of the Royal Society of London*, A244:87–112, 1951.

H.D. Espinosa and P.D. Zavattieri. A grain level model for the study of failure initiation and evolution in polycrystalline brittle materials. Part I: Theory and numerical implementation. *Mechanics of Materials*, 35:333–364, 2003.

U. Essmann and H. Mughrabi. Annihilation of dislocations during tensile and cyclic deformation and limits of dislocation densities. *Philosophical Magazine*, A40:731–756, 1997.

M.L. Falk, A. Needleman, and J.R. Rice. A critical evaluation of dynamic fracture simulations using cohesive surfaces. *Journal de Physique*, IV11:43–50, 2001.

D. Farkas and W.A. Curtin. Plastic deformation mechanisms in nanocrystalline columnar grain structures. *Materials Science and Engineering*, A412:316–322, 2005.

D. Farkas, H. Van Swygenhoven, and P.M. Derlet. Intergranular fracture in nanocrystalline metals. *Physical Review*, B66:060101, 2002.

D. Farkas, S. Van Petegem, P.M. Derlet, and H. Van Swygenhoven. Dislocation activity and nano-void formation near crack tips in nanocrystalline Ni. *Acta Materialia*, 53:3115–3123, 2005.

S.M. Foiles and M.S. Daw. Application of the embedded atom method to Ni_3/Al. *Journal of Materials Research*, 2:5–15, 1987.

A.G. Frøseth, P.M. Derlet, and H. Van Swygenhoven. Dislocation emitted from nanocrystalline grain boundaries: nucleation and splitting distance. *Acta Materialia*, 52:5863, 2004.

K. Gall, M.F. Horstmeyer, M. Van Schildgaarde, and M. Baskes. Atomistic simulations on the tensile debonding of an alumnium-silicon interface. *Journal of the Mechanics and Physics in Solids*, 48:2183–2212, 2000.

H. Gao, Y. Huang, and W.D. Nix. Modeling plasticity at the micron scale. *Naturwissenschaften*, 86:507, 1999.

H. Gao, B. Ji, I.L. Jaeger, E. Arzt, and P. Fratzl. Materials become insensitive to flaws at nanoscale: lessons from nature. *Proceedings of the National Academy of Sciences*, 100:5597, 2003.

M.G. Gehling and H. Vehoff. Computation of the fracture stress in notched NiAl-polycrystals. *Materials Science and Engineering*, A329:255–261, 2002.

D.F. Gibson. *Principle of Composite Material Mechanics.* McGraw-Hill - Engineering mechanics series. New York, 1994.

M.Y. Gutkin and A.E. Romanov. Straight edge dislocations in a thin two-phase plate. *Physica Status Solidi*, 125:107–125, 1991.

H. Hahn, P. Mondal, and K.A. Padmanabhan. Plastic deformation of nanocrystalline materials. *Nanostructured Materials*, 9:603–606, 1997.

E.O. Hall. The deformation and ageing of mild steel: III discussion of results. *Proceeding of the Physical Society of London*, B64:747, 1951.

L.H. Han, L. Li, and J. Sun. Ductile to brittle transition of pure al sheet constrained by strength mismatched parallel bi-interface. *Scripta Materialia*, 52:1157–1162, 2005.

N. Hansen. Hall-petch relation and boundary strengthening. *Scripta Materialia*, 51: 801–806, 2004.

N. Hansen. Boundary strengthening in undeformed and deformed polycrystals. *Materials Science and Engineering*, A409:39, 2005.

A. Hartmaier and P. Gumbsch. Thermal activation of crack-tip plasticity: the brittle or ductile response of a stationary crack loaded to failure. *Physical Review*, B71: 024108–1–11, 2005.

A. Hartmaier, M.J. Buehler, and H. Gao. A discrete dislocation plasticity model of creep in polycrystalline thin films. *Defect and Diffusion Forum*, 107:224–225, 2003.

A. Hartmaier, M. J. Buehler, and H. Gao. Multiscale modeling of deformation in polycrystalline thin metal films on substrates. *Advanced Engineering Materials*, 7:165–169, 2005.

C.H. Henager Jr. and R.G. Hoagland. A rebound mechanism for misfit dislocation creation in metallic nanolayers. *Scripta Materialia*, 50:701–705, 2004.

D. A. Hills, P. A. Kelly, D. N. Dai, and A. M. Korsunsky. *Solution of Crack Problems: The Distributed Dislocation Technique.* Kluwer Academic Publishers, Dordrecht, 1996.

J.D. Honeycutt and H.C. Andersen. Surface step effects on nanoindentation. *Journal of Physical Chemistry*, 91:4950, 1987.

H.W. Höppel, J. May, and M. Göken. Enhanced strength and ductility in ultrafine-grained aluminium produced by accumulative roll bonding. *Advanced Engineering Materials*, 6:781, 2004.

K.J. Hsia, Z. Suo, and W. Yang. Cleavage due to dislocation confinement in layered materials. *Journal of the Mechanics and Physics of Solids*, 42:877–896, 1994.

A.P. Jackson, J.F. Vincent, and R.M. Turner. The mechanical design of nacre. *Proceedings Of the Royal Society of London*, B234:415, 1988.

I. Jager and P. Fratzl. Mineralized collagen fibrils: A mechanical model with a staggered arrangement of mineral particles. *Biophysical Journal*, 79:1737–1746, 2000.

M. Janecek, F. Louchet, B. Doisneau-Cottignies, Y. Bréchet, and N. Guelton. Specific dislocation multiplication mechanisms and mechanical properties in nanoscaled multilayers: the example of pearlite. *Philosophical Magazine*, A80:1605, 2000.

E.A.A. Jarvis, R.L. Hayes, and E. Carter. Effects of oxidation on the nanoscale mechanisms of crack formation in aluminium. *Journal of Chemical Physics and Physical Chemistry*, 2:55–59, 2001.

B. Ji, H. Gao, and T. Wang. Flow stress of biomorphous metal-matrix composites. *Materials Science and Engineering*, A386:435, 2004.

BH. Ji and HJ. Gao. A study of fracture mechanisms in biological nano–composites via the virtual internal bond model. *Materials Science and Engineering*, A366: 96–103, 2004.

F. Kauffmann, B. Ji, G. Dehm, H. Gao, and E. Arzt. A quantitative study of the hardness of a superhard nanocrystalline titanium nitride/silicon nitride coating. *Scripta Materialia*, 52:1269, 2005.

A.S. Khan, H. Zhang, and L. Takacs. Mechanical response and modeling of fully compacted nanocrystalline iron and copper. *International Journal of Plasticity*, 16:1459–1476, 2000.

P. Klein and H. Gao. Crack nucleation and growth as strain localization in a virtual-bond continuum. *Engineering Fracture Mechanics*, 61:21–48, 1998.

C.C. Koch. *Nanostructured materials; processing, properties and applications.* Kluwer Academic Publishers, Norwich, NY, 2002.

H.G.M. Kreuzer and R. Pippan. Discrete dislocation simulation of nanoindentation: the effect of moving conditions and indenter shape. *Materials Science and Engineering*, A 387:254–256, 2004.

K.S. Kumar, H. Van Swygenhoven, and S. Suresh. Mechanical behavior of nanocrystalline metals and alloys. *Acta Materialia*, 51:5743–5774, 2003.

W.J. Landis. The strength of a calcified tissue depends in part on the molecular-structure and organization of its constituent mineral crystals in their organic matrix. *Bone*, 16:533, 1995.

K. Lane, R.H. Dauskardt, A. Vainchtein, and HJ Gao. Plasticity contributions to interface adhesion in thin-film interconnect structures. *Journal of Materials Research*, 15:2758–2769, 2000.

T.G. Langdon. Grain boundary sliding revisited: Developments in sliding over four decades. *Journal of Materials Science*, 41:597–609, 2006.

J.E. Lennard-Jones. The determination of molecular fields. I. from the variation of the viscosity of a gas with temperature. *Proceedings of the Royal Society of London*, A106:441, 1924.

I.H. Lin and R. Thomson. Cleavage, dislocation emission and shielding for cracks under general loading. *Acta Metallurgica et Materialia*, 34:187–206, 1986.

R.C. Lin, D. Steglich, W. Brocks, and J. Betten. Performing RVE calculations under constant stress triaxiality for monotonous and cyclic loading. *International Journal of Numerical Methods in Engineering*, 66:1331–1360, 2006.

J. Llorca, A. Needleman, and S. Suresh. An analysis of the effects of matrix void growth on deformation and ductility in metal ceramic composites. *Acta Metallurgica et Materialia*, 39:2317, 1991.

L. Lu, M.L. Sui, and K. Lu. Superplastic extensibility of nanocrystalline copper at room temperature. *Science*, 287:1463–1466, 2000.

H.M. Ludwig and P. Gumbsch. An empirical interatomic potential for B2 NiAl. *Modelling and Simulation in Materials Science and Engineering*, 3:533, 1995.

D.J. Benson M.A. Meyers, A. Mishra. The deformation physics of nanocrystalline metals: Experiments, analysis, and computations. *Journal of Metals*, 58:41–48, 2006.

S.X. Mao and M.Z. Lib. Effects of dislocation shielding on interface crack initiation and growth in metal/ceramic layered materials. *Journal of the Mechanics and Physics of Solids*, 47:2351–2379, 1999.

R.A. Masumura, P.M. Hazzledine, and C.S. Pande. Yield stress of fine grained materials. *Acta Materialia*, 46:4527–4534, 1998.

J. May, H.W. Höppel, and M. Göken. Strain rate sensitivity of ultrafine-grained aluminium processed by severe plastic deformation. *Advanced Engineering Materials*, 53:189, 2005.

R. Menig, M.H. Meyers, M.A. Meyers, and K.S. Vecchio. Quasi-static and dynamic mechanical response of haliotis rufescens (abalone) shells. *Acta Materialia*, 48: 2383, 2000.

Y. Mishin, D. Farkas, M.J. Mehl, and D.A. Papaconstantopoulos. Interatomic potentials for monoatomic metals from experimental data and ab initio calculations. *Physical Review*, B59:3393–3407, 1999.

Y. Mishin, M.J. Mehl, D.A. Papaconstantopoulos, A.F. Voter, and J.D. Kress. Structural stability and lattice defects in copper: Ab initio, tight-binding, and embedded-atom calculations. *Physical Review*, B63:224106–224101, 2001.

H. Mughrabi. Dual role of deformation-induced geometrically necessary dislocations with respect to lattice plane misorientations and/or long-range internal stresses. *Acta Materialia*, 54:3417–3427, 2006.

T. Mura. *The Continuum Theory of Dislocations*, volume 3 of *in: H. Herman (Ed.), Advances in Materials Research.* Interscience Publishers, New York, 1968.

T. Mura. *Micromechanics of defects in solids.* Martinus Nijhoff Publishers, Dordrecht, 1982.

N. P. O´Dowd, M. G. Stout, and C. F. Shih. Fracture toughness of alumina-niobium interfaces, experiments and analyses. *Journal of the Mechanics and Physics of Solids*, 66:1037–1064, 1992.

N. P. O´Dowd, M. G. Stout, and C. F. Shih. Fracture of a ductile layer constrained by stiff substrates. *Fatigue & Fracture of Engineering Materials & Structures*, 23: 1–13, 2001.

M. Ortiz and A. Pandolfi. Finite-deformation irreversibility cohesive elements for three-dimensional crack-propagation analysis. *International Journal for Numerical Methods in Engineering*, 44:1267–1282, 1999.

N.J. Petch. The cleavage strength of polycrystals. *Journal of the Iron and Steel Institute*, 174:25, 1953.

D. Raabe, F. Roters, F. Barlat, and L. Chen (Editors). *Continuum scale simulation of engineering materials - Fundamentals - Microstructures - Process Applications.* Wiley-VCH Verlag GmbH, 2004.

J.R. Rice and G.F. Rosengren. Plane strain deformation near a crack tip in a power-law hardening material. *Journal of the Mechanics and Physics of Solids*, 12:1–12, 1968.

F.O. Riemelmoser, R. Pippan, and O. Kolednik. Cyclic crack growth in elastic plastic solids: a description in terms of dislocation theory. *Computational Mechanics*, 20: 139–144, 1997.

S.G. Roberts, A.S. Booth, and P.B. Hirsch. Dislocation activity and brittle-ductile transitions in single crystals. *Materials Science and Engineering*, A176:91–98, 1994.

G. Sanders, J. A. Eastman, , and J. R. Weertman. Elastic and tensile behavior of nanocrystalline copper and palladium. *Acta Materialia*, 45:4019, 1997.

F. Sansoz and J.F. Molinari. Incidence of atom shuffling on the shear and decohesion behavior of a symmetric tilt grain boundary in copper. *Scripta Materialia*, 50: 1283–1288, 2004.

F. Sansoz and J.F. Molinari. Mechanical behavior of sigma tilt grain boundaries in nanoscale cu and al: A quasicontinuum study. *Acta Materialia*, 53:1931–1944, 2005.

J.C.J. Schellekens and R. de Borst. On the numerical integration of interface elements. *International Journal of Numerical Methods in Engineering*, 44:1267–1282, 1999.

J. Schiøtz and K. W. Jacobsen. A maximum in the strength of nanocrystalline copper. *Science*, 301:1357, 2003.

J. Schiøtz and F.D. Di Tolla. Softening of nanocrystalline metals at very small grain sizes. *Science*, 391:6667, 1998.

J. Schiøtz, T. Vegge, F.D. Di Tolla, and K.W. Jacobsen. Atomic-scale simulations of the mechanical deformation of nanocrystalline metals. *Physical Review*, B60: 11971–11983, 1999.

Y.-L. Shen, M. Finot, A. Needleman, and S. Suresh. Effective plastic response of 2-phase composites. *Acta Metallurgica et Materialia*, 43:1701–1722, 1995.

YL. Shen. Strength and interface-constrained plasticity in thin metal films. *Journal of Materials Research*, 18:2281–2284, 2003.

YL. Shen and R.W. Leger. Parametric atomistic analysis of dislocationinterface interactions in thin metallic films. *Materials Science and Engineering*, A423:102–106, 2006.

A. Siddiq and S. Schmauder. Interface fracture analyses of a bicrystal niobium/alumina specimen using a cohesive modelling approach. *Modelling and Simulation in Materials Science and Engineering*, 14:1015–1030, 2006.

J. Stadler, R. Mikulla, and H.-R. Trebin. IMD: A software package for molecular dynamics studies on parallel computers. *International Journal of Modern Physics*, C8:1131, 1997.

Z. Suo, C. F. Shih, and A. G. Varias. A theory of cleavage cracking in the presence of plastic flow. *Acta Metallurgica et Materialia*, 41:1551–1557, 1991.

A.P. Sutton and R.W. Balluffi. *Interfaces in crystalline materials*. Clarandon Press, Oxford, 1995.

H. Van Swygenhoven and A. Caro. Plastic behavior of nanophase metals studied by molecular dynamics. *Physical Review*, B58:11246–11251, 1998.

H. Van Swygenhoven, H. Spaczer, and A. Caro. Microscopic description of plasticity in computer generated metallic nanophase samples: A comparison between Cu and Ni. *Acta Materialia*, 47:3117–3126, 1999.

H. Van Swygenhoven, H. Spaczer, A. Caro, and D. Farkas. Competing plastic deformation mechanisms in nanophase metals. *Physical Review*, B60:22–25, 1999a.

H. Van Swygenhoven, H. Spaczer, D. Farkas, and A. Caro. The role of grain size and the presence of low and high angle grain boundaries in the deformation mechanism of nanophase Ni: A molecular dynamics computer simulation. *Nanostructured Materials*, 12:323–326, 1999b.

H. Van Swygenhoven, A. Caro, and D. Farkas. A molecular dynamics study of polycrystalline fcc metals at the nanoscale: Grain boundary structure and its influence on plastic deformation. *Materials Science and Engineering*, A47:440–444, 2001.

H. Van Swygenhoven, P.M. Derlet, and A. Hasnaoui. Atomic mechanism for dislocation emission from nanosized grain boundaries. *Physical Review*, B66:024101–024101, 2002.

H. Van Swygenhoven, P.M. Derlet, and A.G. Frøseth. Stacking fault energies and slip in nanocrystalline metals. *Nature Materials*, 3:399–403, 2004.

V. Tvergaard and J. W. Hutchinson. Toughness of an interface along a thin ductile layer joining elastic solids. *Philosophical Magazine*, A70:641, 1994.

V. Tvergaard and J.W. Hutchinson. The influence of plasticity on mixed mode interface toughness. *Journal of the Mechanics and Physics of Solids*, 41:1119–1135, 1993.

R. Valiev. Nanostructuring of metals by severe plastic deformation for advanced properties. *Nature Materials*, 3:511–516, 2004.

R.Z. Valiev, YT. Zhu I.V. Alexandrov and, and T.C. Lowe. Paradox of strength and ductility in metals processed by severe plastic deformation. *Journal of Materials Research*, 17:5–8, 2002.

E. Van der Giessen and A. Needleman. Discrete dislocation plasticity: a simple planar model. *Modelling and Simulation in Materials Science and Engineering*, 3:689–735, 1995.

A.G. Varias, Z. Suo, and C. F. Shih. Ductile failure of a constrained metal foil. *Journal of the Mechanics and Physics of Solids*, 39:963–986, 1991.

H. Vehoff. From in situ crack growth tests to nanoindentation in UFG matrials. *Modelling and Simulation in Materials Science and Engineering*, 15:313, 2007.

S. Veprek. The search for novel, superhard materials. *Journal of Vacuum Science & Technology*, A 17:2401, 1999.

A. Vinogradov, S. Hashimoto, V. Patlan, and K. Kitagawa. Atomic force microscopic study on surface morphology of ultra-fine grained materials after tensile testing. *Materials Science and Engineering*, A319:862–866, 2001.

T. Volpp, E. Gring, W.M. Kuschke, and E. Arzt. Grain size determination and limits to hall-petch behaviour in nanocrystalline NiAl powder. *Nanostructured Materials*, 8:855, 1997.

F. Voter and SP. Chen. Accurate interatomic potentials for Ni, Al and Ni3Al characterization of defects. *Materials Research Society Symposium Proceedings*, 82:175–180, 1987.

YM. Wang, MW. Chen, FH. Zhou, and E. Ma. High tensile ductility in a nanostructured metal. *Nature*, 419:912, 2002.

J.R. Weertman. Microstructure and mechanical behavior of nanocrystalline metals. *Materials Science and Engineering*, A285:391, 2000.

YJ. Wei and L. Anand. Grain-boundary sliding and separation in polycrystalline metals: application to nanocrystalline fcc metals. *Journal of the Mechanics and Physics of Solids*, 52:2587–2616, 2004.

D. Wolf. Structure-energy correlation for grain boundaries in f.c.c metals. III. symmetrical tilt boundaries. *Acta Metallurgica*, 38:781–790, 1990.

D. Wolf, V. Yamakov, S.R. Phillpot, A. Mukherjee, and H. Gleiter. Deformation of nanocrystalline materials by molecular-dynamics simulation: Relationship to experiments? *Acta Materialia*, 53:1–40, 2005.

X. Xu and A. Needleman. Numerical simulations of fast crack growth in brittle solids. *Journal of the Mechanics and Physics of Solids*, 42:1397–1434, 1994.

V. Yamakov, D. Wolf, S.R. Phillpot, A.K. Mukherjee, and H. Gleiter. Dislocation processes in the deformation of nanocrystalline aluminium by molecular-dynamics simulation. *Nature*, 1:45–48, 2002.

V. Yamakov, D. Wolf, S.R. Phillpot, A.K. Mukherjee, and H. Gleiter. Deformation mechanism crossover and mechanical behaviour in nanocrystalline materials. *Philosophical Magazine Letters*, 83:385–393, 2003.

V. Yamakov, D. Wolf, S.R. Phillpot, A.K. Mukherjee, and H. Gleiter. Deformation-mechanism map for nanocrystalline metals by molecular-dynamics simulation. *Nature Materials*, 3:43, 2004.

V. Yamakov, E. Saether, D.R. Phillips, and E.H. Glaessgen. Molecular-dynamics simulation-based cohesive zone representation of intergranular fracture processes in aluminum. *Journal of the Mechanics and Physics of Solids*, 54:1899–1928, 2006.

B. Yang, S. Mall, and K. Ravi-Chandar. A cohesive zone model for fatigue crack growth in quasibrittle materials. *International Journal of Solids and Structures*, 38:3927–3944, 2001.

S. Yip. The strongest size. *Nature*, 391:532, 1998.

P.D. Zavattieri and H.D. Espinosa. Grain level analysis of crack initiation and propagation in brittle materials. *Acta Materialia*, 49:4291–4311, 2001.

YW. Zhang, P. Liu, and C. Lu. Molecular dynamics simulations of the preparation and deformation of nanocrystalline copper. *Acta Materialia*, 52:5105–5114, 2004.

J.A. Zimmerman, HJ. Gao, and F.F. Abraham. Generalized stacking fault energies for embedded atom fcc metals. *Modelling and Simulation in Materials Science and Engineering*, 8:103–115, 2000.

J.A. Zimmerman, C.L. Kelchner, J.C. Hamilton, and S.M. Foiles. Surface step effects on nanoindentation. *Physical Review Letters*, 87:165507, 2002.